Universität Hamburg
DER FORSCHUNG | DER LEHRE | DER BILDUNG

Methane emissions from the East Siberian Arctic Shelf inferred from accurate observations of atmospheric methane mole fractions

Dissertation
with the aim of achieving a doctoral degree
at the Faculty of Mathematics, Informatics and Natural Sciences
Department of Earth Sciences
at Universität Hamburg

by Dipl.-Phys. Friedemann Reum

2019

Prepared at:
Max Planck Institute
for Biogeochemistry
Jena

Accepted as Dissertation at the Department of Earth Sciences

Date of oral defense:
April 25, 2019

Reviewers:
Prof. Martin Claußen, University of Hamburg
Prof. Martin Heimann, Max Planck Institute for Biogeochemistry, Jena

Chair of the examination commission:
Prof. Martin Claußen, University of Hamburg

Chair of the Subject Doctoral Committee:
Prof. Dr. Dirk Gajewski

Dean of Faculty of MIN:
Prof. Dr. Heinrich Graener

Abstract

In the Arctic, vast carbon reservoirs are preserved by cold climate conditions. Due to climate change, they are at risk of degradation, which could lead to increased levels of greenhouse gases in the atmosphere. One of these reservoirs is the seabed of the East Siberian Arctic Shelf (ESAS), which has in recent years attracted attention as a potentially large source of methane (CH_4) to the atmosphere, both at present and in warmer conditions projected by climate models for the coming decades. Yet, estimates of the current annual CH_4 outgassing of the shelf as well as key controls of the emissions are highly uncertain. One reason for the uncertainties is limited data coverage. Thus, this work aims at (1) improving the data availability on CH_4 emissions from the East Siberian Arctic Shelf and (2) estimating current CH_4 emissions from this region to the atmosphere. To achieve the first goal, an observation station for atmospheric greenhouse gases was established in the remote locality Ambarchik at the coast of the East Siberian Sea. The station Ambarchik operates continuously since it was established in August 2014 and provides accurate CO_2 and CH_4 data suitable for estimating the sources and sinks of these gases via inverse modeling of atmospheric transport. As a side product of the calibration efforts of Ambarchik data, an improvement of the accuracy of measurements of greenhouse gas mole fractions in humid air with the widely used instruments manufactured by Picarro, Inc. was achieved. To achieve the second goal, data obtained at Ambarchik were used together with data from other sites to estimate CH_4 emissions from the ESAS to the atmosphere via an inverse model of atmospheric CH_4 transport. Results indicate that the ESAS CH_4 emission budget is on the low end of literature estimates (0.4–1.5 Tg CH_4 yr^{-1} compared to 0–17 Tg; 1 Tg = 10^{12} g). Retrieved spatial emission patterns indicate emissions originate predominantly from shallow areas of the ESAS. Seasonal variations indicate potentially large emissions during fall, continued emissions during the ice-covered period, and limited emissions during ice melt. While this allowed some speculation on the underlying emission controls, the explanatory power of the retrieved spatiotemporal emission patterns was limited by limitations of the atmospheric data coverage and the model. Overall, the estimated budget indicates that the relevance of the ESAS for the present global atmospheric CH_4 budget is small.

Zusammenfassung

In der Arktis sind enorme Kohlenstoffreservoire durch das kalte Klima konserviert. Durch den Klimawandel droht ihre Zersetzung, was zu einer Erhöhung des Treibhausgasgehalts in der Atmosphäre führen könnte. Eines dieser Reservoire ist der Meeresboden des Ostsibirischen Arktischen Schelfs, das in den letzten Jahren Beachtung als möglicherweise starke Quelle für Methan in der Atmosphäre auf sich gezogen hat, sowohl gegenwärtig als auch in wärmeren Bedingungen die von Klimamodellen für die kommenden Jahrzehnte vorhergesagt werden. Dennoch sind Abschätzungen der momentanen jährlichen Methanausgasung des Schelfs sowie maßgebliche Einflüsse von denen die Emissionen gesteuert werden höchst unsicher. Ein Grund für die Unsicherheiten ist die beschränkte Datenabdeckung. Deshalb zielt diese Arbeit darauf ab, (1) die Datenlage über Methanemissionen des Ostsibirischen Arktischen Schelfs zu verbessern und (2) die momentanen Methanemissionen aus dieser Region abzuschätzen. Um das erste Ziel zu erreichen wurde eine Beobachtungsstation für Treibhausgase in der Atmosphäre im abgelegenen Ort Ambarchik an der Küste der Ostsibirischen See eingerichtet. Die Station Ambarchik arbeitet kontinuierlich seit ihrer Einrichtung im August 2014 und liefert genaue CO_2- und CH_4-Daten die geeignet sind um die Quellen und Senken dieser Gase mittels inverser Modellierung des atmosphärischen Transports abzuschätzen. Als Nebenprodukt der Bemühungen um die Kalibration der Ambarchik-Daten wurde eine Verbesserung der Genauigkeit von Messungen des Stoffmengengehaltes von Treibhausgasen in feuchter Luft mit den weithin genutzten Instrumenten von Picarro, Inc. erreicht. Um das zweite Ziel zu erreichen wurden die in Ambarchik gewonnen Daten zusammen mit Daten anderer Stationen genutzt um Methanemissionen vom Ostsibirischen Arktischen Schelf in die Atmosphäre mittels eines inversen Modells des atmosphärischen Methantransports abzuschätzen. Die Ergebnisse deuten darauf hin, dass die Methanemissionen des Schelfs am unteren Ende der Abschätzungen in der Fachliteratur liegen (0.4–1.5 Tg CH_4 pro Jahr gegenüber 0–17 Tg; 1 Tg = 10^{12} g). Erfasste räumliche Muster deuten darauf hin dass die Emissionen vorwiegend von flachen Bereichen des Schelfs stammen. Zeitliche Variationen deuten auf möglicherweise hohe Emissionen im Herbst, fortgesetzte Emissionen während der eisbedeckten Periode, und begrenzte Emissionen während der Eisschmelze hin. Während dies Spekulationen über die zugrundeliegenden steuernden Einflüsse erlaubte, war die Aussagekraft der räumlichen und zeitlichen Emissionsmuster begrenzt aufgrund von Limitierungen der Datenlage und des Modells. Insgesamt deutet das abgeschätzte Budget darauf hin, dass das Ostsibirische Arktische Schelf derzeit für den globalen atmosphärischen Methanhaushalt von geringer Bedeutung ist.

Table of contents

1 Introduction

1.1 Motivation

Greenhouse gases are one of the major drivers of present day climate change (IPCC, 2013). Therefore, understanding their natural sources and sinks is crucial for projections of future climate trajectories. In this context, special attention is directed towards so-called tipping elements, i.e. systems which may transition to a new state due to climate change and that may not be easily reverted to the previous state (Lenton et al., 2008; Steffen et al., 2018). One of these systems is the case of vast amounts of carbon stored in the Arctic and preserved by cold climate conditions (Hugelius et al., 2014; James et al., 2016; Schuur et al., 2015). Terrestrial (Schuur et al., 2013) and subsea (James et al., 2016) carbon reservoirs are at risk of being degraded and released to the atmosphere in warming conditions. A substantial release of the stored carbon in the form of CO_2 and CH_4 would constitute a significant positive feedback enhancing global warming. Therefore, improved insight into the mechanisms that govern the sustainability of Arctic carbon reservoirs and greenhouse gas exchange with the atmosphere is essential for the assessment of Arctic carbon-climate feedbacks and the simulation of accurate future climate trajectories.

In recent years, the East Siberian Arctic Shelf (ESAS), one of the carbon pools potentially degrading under climate change, has attracted interest as a potentially important source of CH_4 to the atmosphere at present and in the future (Shakhova et al., 2015, 2010a). The CH_4 cycle within the shelf is a complex system of a variety of sources, sinks, reservoirs and transport mechanisms (Damm et al., 2018; Fenwick et al., 2017; Sapart et al., 2017; Shakhova et al., 2015; Zhou et al., 2014). Constraints on present-day shelf-wide CH_4 emissions to the atmosphere are uncertain, with greatly varying budget estimates in the literature. A previously identified reason for the uncertainties is limited data coverage. Previous studies relied either on bottom-up scaling of emission estimates based on temporary in-situ campaigns, in many cases with a focus on the ice-free season and coastal regions. Others scaled emission scenarios to fit data from the sparse network of calibrated atmospheric CH_4 observation stations in the Arctic. Better constraints on current CH_4 emissions from the ESAS to the atmosphere, based on more data and refined methods, could contribute to a better understanding of the factors that control the emissions and thus, ultimately, contribute to a better understanding of the ESAS CH_4 cycle and how it may evolve in our changing climate.

1.2 Goals of this thesis

This work aims to better constrain present-day ESAS CH_4 emissions using atmospheric CH_4 signals. Given the sparse data coverage, the main goals of this study are two-fold:

1. Gather year-round accurate observations of atmospheric greenhouse gases at the coast of the East Siberian Arctic Shelf

To achieve this goal, a station that continuously measures dry air mole fractions of atmospheric greenhouse gases (CO_2 and CH_4) was established in Ambarchik, Northeast Siberia. Tasks encompassed setup and maintenance of the station, as well as processing, calibration and quality control of the data.

2. Estimate CH_4 emissions from the East Siberian Arctic Shelf to the atmosphere based on an inverse model of atmospheric CH_4 transport

This goal encompassed estimating the annual ESAS CH_4 budget based on year-round measurements, finding spatiotemporal patterns in the emissions and, if possible, linking them to controlling mechanisms.

1.3 Structure of this thesis

This thesis begins with a review of the CH_4 cycle of the ESAS, including a review of literature estimates on CH_4 emissions from the ESAS to the atmosphere (Chapter 2). Next, the methods for estimating ESAS CH_4 emissions used in this study are introduced (Chapter 3). Chapter 4 describes the observations gathered at the new station Ambarchik. Chapter 5 describes the setup and results of an inverse modeling study on ESAS CH_4 emissions based on the preceding chapters. The main conclusions on the stated goals are given in Chapter 6.

2 The CH_4 cycle of the East Siberian Arctic Shelf

The East Siberian Arctic Shelf is an environment with complex biogeochemical cycles and hosts large carbon pools of uncertain stability. In the following sections, the origins of CH_4 in ESAS waters and the state of knowledge on dynamics relevant for CH_4 release to the atmosphere are introduced. The chapter concludes with a review of evidence for CH_4 outgassing from the shelf to the atmosphere (Sect. 2.6).

2.1 Origins of carbon in the seabed

Methanogenesis requires a carbon source. In this section, sources of carbon in the seabed of the East Siberian Arctic Shelf that can contribute to methanogenesis are introduced.

2.1.1 Surface sediment layer and organic carbon input

The topmost sediment layer of the East Siberian Arctic Shelf originates from mostly terrestrially (western part) or oceanically (eastern part) derived carbon, with the boundary between the domains located in the eastern part of the East Siberian Sea (Anderson et al., 2011; Semiletov et al., 2005). The divide stems from the dominant water masses. Sediments in the Laptev Sea and the majority of the East Siberian Sea are dominated by contemporary coastal erosion and river input, which carry organic carbon from adjacent terrestrial ecosystems (Rachold et al., 2000; Semiletov et al., 2012; Vonk et al., 2012). The Chukchi Sea, on the other hand, is dominated by Pacific waters, and the sediments are partly of terrestrial and partly of marine origin (Semiletov et al., 2012).

2.1.2 Subsea permafrost

Beneath the surface sediment layer (Sect. 2.1.1), the East Siberian Arctic Shelf is underlain by carbon-rich submerged permafrost, which formed in the Pleistocene. I.e. over the past hundreds of thousands of years, several transgressions and regressions of the ocean to occurred on the ESAS (Nicolsky et al., 2012), the most recent of which (the Holocene transgression), took place between about 12 and 5 kyr ago (Bauch et al., 2001) with some near-shore areas submerged later (Nicolsky et al., 2012). In the Siberian Arctic, remnants of the biosphere accumulated over timescales of hundreds of thousands of years, forming soils rich in organic carbon ("yedoma") that does not degrade in the cold temperatures (Romanovskii et al., 2005; Sher et al., 2005; Zimov et al., 2006). The permafrost layer of the East Siberian Arctic Shelf is a relic of the accumulations that took place while the area was not submerged (Romanovskii et al., 2005).

The extent of subsea permafrost in the ESAS is uncertain. Cramer and Franke (2005) speculated that the northern part of the shelf is not covered by continuous permafrost based on the occurrence of gas flares; a similar observation was made in the Kara Sea (Portnov et al., 2013). Ruppel et al. (2015) assumed a permafrost extent up to 30m depth based on observational results for the Kara Sea and Beaufort Sea, which qualitatively agrees with Cramer and Franke. Other assessments of the state of permafrost that could allow mapping its extent relied on models (e.g. Nicolsky et al., 2012).

Shakhova et al. (2010b) give an estimate of the size of this carbon pool at 500 Gt, citing Zimov et al. (2006)[1].

2.1.3 Methane hydrates

CH_4 (and other gases) can be trapped in lattices of water ice, forming hydrates (e.g. Gornitz and Fung, 1994). Hydrate stability in the ESAS seabed is limited by low pressure and/or high temperature at the top, and the geothermal gradient at the bottom. Various upper limits for the "Gas Hydrate Stability Zone" (GHSZ) in the Arctic have been reported, e.g. 300 m (Archer, 2015, model result) and 120 m (Dallimore and Collett, 1995, observations) below sea level. The GHSZ can be several hundred meters thick (Archer, 2015). Shakhova et al. (2010b) cited a total mass estimate of 540 Gt carbon for this pool[2].

2.1.4 Natural gas

Below the GHSZ, CH_4 can occur as free gas. Seeps of thermogenic CH_4 have been observed during gas field exploration in the Laptev Sea, suggesting the presence of a natural gas pool (Cramer and Franke, 2005). Shakhova et al. (2010b) also cited earlier reports on the existence of a free gas pool underneath the permafrost, with an estimated mass of 360 Gt carbon[3].

2.2 CH_4 sources to ESAS waters

CH_4 emissions from the seabed are a widespread phenomenon observed globally (e.g. Etiope, 2015; Judd, 2003). Sea bed CH_4 can be produced biogenically (microbial decomposition of organic matter), thermogenically (degradation of organic matter in high temperatures and pressures over millions of years), or abiotically (via various chemical processes). In the seabed of the East Siberian Arctic Shelf, surface sediment and permafrost may serve as substrate for biogenic CH_4, and CH_4 from dissociating hydrates or free gas may migrate upwards. In the following paragraphs, sources of CH_4 to the waters of the ESAS are presented.

2.2.1 Mobilization of old carbon

It has been hypothesized that the permafrost layer acts as a barrier for underlying CH_4, and that this "lid" is at present being compromised, both releasing permafrost-derived CH_4 and

---

[1] The 500 Gt estimate by Zimov et al. is for yedoma soil covering a land surface of 1 Mio. km^2. Therefore, this ESAS carbon pool estimate should actually be ~1000 Gt carbon.

[2] The cited sources therein were in Russian and thus inaccessible to the author.

[3] The cited sources therein were in Russian and thus inaccessible to the author.

opening migration pathways for underlying CH_4 (Shakhova et al., 2010a). As a result, CH_4 could be released in dissolved form or, more rapidly, as bubbles (gas flares), which has been observed on the Arctic shelves (see Sect. 2.3.2 on bubble transport). In the following paragraphs, possible warming mechanisms and other pathways for CH_4 emissions to the shelf waters are briefly introduced.

Warming from the top

Model results suggest that at present permafrost is thawing due to warming by ocean waters since the Holocene transgression (Dmitrenko et al., 2011), which are warmer than the average air temperature. The state of permafrost degradation has been linked to seafloor CH_4 emissions (Shakhova et al., 2015). The time scale of thawing implies that the permafrost layer should be more intact in shallower waters, which were flooded more recently (Archer, 2015 and references therein). Degradation may be related to submerged taliks, i.e. layers or pockets of unfrozen water within the permafrost that formed beneath thaw lakes or rivers before the transgression (Frederick and Buffett, 2014; Nicolsky et al., 2012). Also, the large Arctic rivers transport warm water to the shelf, which may cause permafrost to thaw (Delisle, 2000; Romanovskii et al., 2005; Semiletov et al., 2012). Modern climate change has been hypothesized to trigger abrupt release of vast amounts of CH_4, inducing a positive global warming feedback (Shakhova et al., 2010a). Although recent warming related to climate change has warmed shallow Arctic shelf waters of the ESAS (Dmitrenko et al., 2011), model results indicate that this warming has a considerable impact on CH_4 release due to permafrost degradation and hydrate destabilization rather on millennial timescales (Archer, 2015; Dmitrenko et al., 2011). Note that climate-change-related warming of bottom waters has been linked to increased CH_4 emissions from the continental margin to the ocean off Svalbard (c.f. James et al., 2016; Walczowski and Piechura, 2006; Westbrook et al., 2009).

Warming from the bottom

Subsea permafrost may be degraded and CH_4 hydrates destabilized where the geothermal heat flux is high, i.e. at fault zones (Romanovskii and Hubberten, 2001) or paleo-river beds (Frederick and Buffett, 2014).

Exposure at the continental slope

The transition from the continental shelf to the deep Arctic Ocean (continental slope) exposes deep sediment layers closer to ocean water. At the slope, large gas hydrate deposits have been suggested (e.g. Cramer and Franke, 2005; references in Miller et al., 2017) which may be prone to destabilization and escape to the water column due to the absence of a permafrost cover. At the Laptev Sea slope, increased CH_4 concentrations in bottom waters have been observed (Schröder, 2000). However, a recent expedition found no evidence for elevated CH_4 in sediment cores from the slope of the East Siberian Sea, putting abundant escape of CH_4 to the water column across the slope into question (Miller et al., 2017).

2.2.2 Production and consumption in the surface sediment

CH_4 can be produced microbially in anoxic environments in the surface sediment in the seafloor (e.g. Koch et al., 2009) and has been shown to be a source of CH_4 to bottom waters of the ESAS (e.g. Fenwick et al., 2017; Li et al., 2017; Matveeva et al., 2015; Reeburgh, 2007; Savvichev et al., 2007). However, CH_4 can also be removed in the surface sediment by anaerobic oxidation, e.g. sulfate reduction. This process may limit how much CH_4 from thawing subsea permafrost reaches the water (Overduin et al., 2015; Winkel et al., 2018).

2.2.3 River input of CH_4

Arctic rivers carry dissolved and particulate terrestrial organic matter to the Arctic Ocean, which can be degraded and released to the atmosphere as CH_4. The largest stream that enters the ESAS, the Lena, exhibits elevated CH_4 levels in its delta, but the excess CH_4 is vented to the atmosphere before reaching the Laptev Sea (Bussmann, 2013). The mouth of the Kolyma river exhibits elevated concentrations of dissolved CH_4, which indicates that it transports CH_4 to the East Siberian Sea (Shakhova and Semiletov, 2007).

2.2.4 Microbial production and consumption of CH_4 in the shelf water

CH_4 can be produced microbially in upper ocean waters in the Arctic by methanogens. There is evidence for methanogenesis via DMSP (dimethylsulfoniopropionate) as a substrate. DMSP is produced by phytoplankton. Accordingly, in situ CH_4 production is correlated with phytoplankton blooms (Damm et al., 2008, 2010), which has been observed in the Pacific-dominated Chukchi Sea (Fenwick et al., 2017; Li et al., 2017). Another observed pathway is via methylphosphanate (Repeta et al., 2016).

CH_4 in Arctic shelf waters that is produced in situ or released from the seafloor is partially consumed by microbial oxidation (Fenwick et al., 2017; Li et al., 2017), which diminishes the amount of CH_4 that reaches the atmosphere. This process is more effective the longer the residence time of CH_4 in the water is, i.e. in the presence of dynamical barriers (see Sect. 2.3.1 and 2.4). Li et al. (2017) concluded that, in the Chukchi Sea, 43 % of all CH_4 input is consumed microbially, while 52 % reaches the atmosphere. Shakhova et al. (2015) found a turnover time of 300–1000 days for dissolved CH_4 in the ESAS and concluded that considerable fractions of it would therefore reach the atmosphere.

2.3 CH_4 transport in ESAS water

CH_4 released from the seabed into the water does not necessarily reach surface waters and the atmosphere due to microbial consumption (Sect. 2.2.4) and dynamical barriers that can effectively trap dissolved CH_4 in bottom waters. This section introduces the literature on the fate of CH_4 in the shelf waters.

2.3.1 Stable stratification of shelf waters

In general, stable stratifications can occur due to density gradients (pycnoclines) related to temperature or salinity (Myhre et al., 2016). For example, in summer, upper Arctic shelf waters can be stably stratified due to freshwater input, e.g. from the Lena river (Charkin et al., 2011; Wåhlström et al., 2012). In the Laptev Sea, seasonal variations of the pycnocline have been shown (Janout et al., 2017). It is heavily influenced by sea ice dynamics (Sect. 2.4), and can be deepened by wind-driven mixing, which is most effective during storms (Shakhova et al., 2014). A rough estimate for its depth during the ice-free season is on the order of 10 m (Thornton et al., 2016b) to 20 m (M. Janout, personal communication). CH_4 trapped in a stratified water column is more likely to be consumed (Sect. 2.2.4). Thus, stratification can inhibit emissions of CH_4 from the ESAS to the atmosphere.

2.3.2 Bubble transport (gas flares)

The microbial sink in the water column can be circumvented by CH_4 that enters the water in the form of bubbles. CH_4 gas flares emanating from the seafloor have been observed across the Arctic shelf seas and continental slopes (Andreassen et al., 2017; Cramer and Franke, 2005; Mau et al., 2017; Myhre et al., 2016; Paull et al., 2007; Portnov et al., 2013; Shakhova et al., 2010a; Westbrook et al., 2009). Bubble plumes rising through the water column are partially dissolved, and the fraction that reaches the surface depends on their size, density, release depth, dissolved CH_4 concentration in the surrounding water, and other factors (DelSontro et al., 2015; e.g. Leifer and Patro, 2002; McGinnis et al., 2006).

2.3.3 Lateral transport with ocean currents

ESAS shelf waters are advected with ocean currents (Damm et al., 2018; Kvenvolden et al., 1993; Li et al., 2017; Shakhova et al., 2015). This process may limit CH_4 accumulation under and in sea ice on the shelf and instead distribute CH_4 to other parts of the Arctic Ocean (Damm et al., 2018).

2.4 Role of sea ice for the CH_4 cycle of the ESAS

The seasonal sea ice cover plays a dominant role in the CH_4 cycle of the ESAS. Sea ice formation, cover and melt influence the dynamics of CH_4 transfer from the water to the atmosphere, as well as mixing and stratification of the water column. Furthermore, CH_4 can be stored and produced in situ in sea ice. These processes are introduced in the following paragraphs.

Sea ice as a barrier between water and atmosphere

Closed sea ice cover strongly restricts the flux of CH_4 to the atmosphere, acting as an effective barrier that traps CH_4 below the surface (e.g. Zhou et al., 2014) and increases its residence time and thus consumption (Kitidis et al., 2010). However, open water is present in Arctic sea ice throughout the winter in the form of leads and polynyas (introduced below) through which CH_4 can be emitted to the atmosphere in winter (Kort et al., 2012). Furthermore, it has been shown that sea ice can be permeable for CH_4 (Crabeck et al., 2014; Kelley and Gosink, 1979; Loose et al., 2011; Lovely et al., 2015), but the gas transfer velocity is much smaller than direct air-sea gas transfer if fractures in the ice are present (Loose et al., 2011).

Water column mixing during sea ice formation and refreezing of leads and polynyas

During sea ice formation, brine (water with very high salinity) is ejected from the sea ice. This can lead to direct CH_4 outgassing from the brine (Zhou et al., 2014) and, due to the high density of the brine that causes it to sink, mixing of the water column, enabling transport of CH_4 from seabed sources to the surface (Damm et al., 2015a). Sea ice formation continues throughout the winter in areas of open water in the ice, i.e. leads and polynyas. The terms "leads" and "polynyas" are sometimes used ambiguously in the literature. Here, "leads" denominate linear cracks on the order of meters to kilometers in width that form in drift ice through shear stress and are transient features (Miles and Barry, 1998). "Polynyas" can be larger and more persistent than leads and can form through several mechanisms. Upwelling of warm bottom water e.g. driven by ocean currents can cause ice melt and prevent refreezing ("sensible heat polynyas", cf. Ainley et al., 2003). Persistent winds can create openings at the interface of land-fast sea ice and drift ice ("latent heat polynyas", Eicken, 2003), forming an area of continuous ice production and thus brine rejection throughout winter (Lowry et al., 2018 and references therein). In particular, the Great Siberian Polynya, which can be up to 200 km wide (Dmitrenko et al., 2005), remains open at the interface of land-fast ice and drift ice in the Laptev Sea and parts of the East Siberian Sea every year and has been suggested as a pathway for CH_4 to the atmosphere in winter (Shakhova et al., 2015). In polynyas and leads, enhanced mixing due to refreezing has been observed and associated with considerably enhanced air-sea gas transfer compared to open water conditions (Damm et al., 2007; Else et al., 2011; Lowry et al., 2018; Steiner et al., 2013). For example, Else et al. (2011) estimated CO_2 fluxes in an area of fractional sea ice cover to be 1–2 orders of magnitude higher than open ocean fluxes during summer. Damm et al. (2007) estimated CH_4 emissions from a polynya close to Svalbard similar in magnitude (26–104 μmole m^{-2} d^{-1}) to hot spots estimated for the ESAS in the summer (45–95 μmole m^{-2} d^{-1}, (Shakhova and Semiletov, 2007)).

CH_4 cycling in sea ice

In situ CH_4 production and (chemical and biological) consumption in sea ice has been suggested (Damm et al., 2015a; Fenwick et al., 2017; He et al., 2013). However, in a study on land-fast sea ice close to Barrow, Alaska, physical mechanisms were the dominant drivers of CH_4 exchange between sea ice, surface waters and atmosphere, such as retention, permeability during formation and breakup, and brine rejection (Zhou et al., 2014).

Ice melt

During ice melt, CH_4 accumulated under or stored in ice can be released to the atmosphere (Kvenvolden et al., 1993; Shakhova et al., 2010a; Zhou et al., 2014). On the other hand, melting sea ice forms a fresh melt water layer at the sea surface, which is lighter than the salt water below and therefore can increase stratification and has been observed to trap CH_4-rich water beneath, restricting outgassing to the atmosphere (Damm et al., 2015a; Kitidis et al., 2010).

2.5 Air-sea CH_4 transfer: Diffusion and Ebullition

Exchange of CH_4 dissolved in water and the atmosphere is governed by turbulent diffusion. Gas transfer via turbulent diffusion depends on the partial pressure difference of the gas between air and water, turbulence at the interface, the viscosity of the water and the solubility of the gas. Turbulence is often expressed as a function of wind speed, while viscosity and solubility depend on the temperature and salinity of the water, as well as atmospheric surface pressure (Wanninkhof, 1992). This parameterization has shortcomings, and more processes play a role, e.g. at high wind speeds and the ice edge. Gas transfer at the air-ocean interface and in the presence of sea ice is a subject of ongoing research (e.g. Bigdeli et al., 2018; Deike and Melville, 2018; Turner et al., 2018; Zavarsky et al., 2018).

Besides diffusive air-sea gas transfer, CH_4 gas flares from the seafloor (Sect. 2.3.2) may reach the surface in shallow waters (Leifer et al., 2006). This process is termed ebullition.

2.6 Observational and model evidence for CH_4 emissions from the ESAS to the atmosphere: pathways, distribution and budget

2.6.1 Observations of seabed CH_4 sources and emissions to the atmosphere

In this section, observational evidence for CH_4 outgassing from the ESAS to the atmosphere is summarized.

During numerous ship-based campaigns, widespread CH_4 supersaturation of ESAS surface waters has been observed (Cramer and Franke, 2005; Fenwick et al., 2017; Li et al., 2017; Savvichev et al., 2007; Shakhova et al., 2010a). Since partial pressure differences at the air-water interface drive gas transfer between water and atmosphere via diffusive gas transfer (Sect. 2.5), the observed supersaturation implies CH_4 emissions to the atmosphere.

Besides diffusion, widespread ebullition has been reported as a pathway of CH_4 from the ESAS to the atmosphere (Shakhova et al., 2014). Ebullition fluxes originate from seeps on the seafloor (Sect. 2.5), which are presumably paths for CH_4 derived from ancient carbon in the seabed to the water column (cf. Sect. 2.2.1). These seeps are common not only in the ESAS, but also on other Arctic shelves like the shelf off Svalbard (e.g. Mau et al., 2017), the

Kara Sea (Portnov et al., 2013), Beaufort Sea (Paull et al., 2007), and Barents Sea (Andreassen et al., 2017).

Shakhova et al. (2010a) reported large spatial heterogeneity of ESAS CH_4 emissions to the atmosphere, and distinguished between "background" emissions and "hotspots", presumably related to large CH_4 seeps (cf. Sect. 2.2.1). They estimated that hotspots constitute 10 % of the area of the ESAS and attributed a significant amount of the total ESAS CH_4 emissions to them. These patterns may be seen in remote sensing data as well (Yurganov and Leifer, 2016), although the accuracy of these analyses may not be sufficient to discern patterns and estimate emission rates (Martin Heimann, personal communication). Locally enhanced atmospheric CH_4 levels in the atmosphere above the ESAS have been observed by others as well (Pankratova et al., 2018). Thornton et al. (2016b) observed only few gas flares in the central shelf and concluded that the CH_4 flux to the atmosphere there was predominantly driven by turbulent diffusion.

Besides emissions of CH_4 from the seabed, Li et al. (2017) estimated that 20 % of the CH_4 input to the Chukchi Sea is from in situ production in the water. The studies that included a focus on in situ production (Fenwick et al., 2017; Li et al., 2017) estimated CH_4 emissions to the atmosphere on the low end of the literature estimates.

Whether CH_4 in the water reaches the atmosphere depends on its turnover time and its residence time. Shakhova et al. (2015) reported a turnover time of dissolved CH_4 in ESAS waters of 300–1000 days and argued that this makes the release of large parts of the CH_4 input to the shelf water to the atmosphere likely due to storms that mix the water column. This assessment was contested by Thornton et al. (2016b). Indeed, the fraction of CH_4 that reaches the atmosphere without mixing of the water column may be small. Off Svalbard, observations indicate that large concentrations of dissolved CH_4 originating from seeps can be trapped effectively below 50 m depth due to stable stratification of the water, and significant amounts would only reach the atmosphere when the stratification is broken, e.g. during storms (Myhre et al., 2016). In the Beaufort Sea, Sparrow et al. (2018) observed that dissolved CH_4 derived from ancient carbon sources does not reach above 30 m below the surface.

Outgassing of CH_4 during sea ice growth from Arctic shelves was observed as well as of retention of CH_4 in sea ice and release during melt (Damm et al., 2015a; Zhou et al., 2014).

2.6.2 Estimates of the annual ESAS-wide CH_4 budget in the literature: differences between studies and knowledge gaps

Literature estimates of the magnitude of CH_4 emissions from the ESAS to the atmosphere vary widely, from 0 to 17 Tg CH_4 yr^{-1} (Table 1). By comparison, the global CH_4 budget is 540–568 Tg CH_4 yr^{-1} with an annual growth rate of atmospheric CH_4 of around 10 Tg (Saunois et al., 2016). Thus, the high end of the estimates would constitute a globally significant source and warrants increased interest in the ESAS as a CH_4 source, in particular in the context of potential destabilization of submarine carbon pools and thus increased emissions in a warming climate. ESAS CH_4 budget estimates in the literature are based on upscaling of local flux estimates obtained during ship-based campaigns, modeling atmospheric CH_4 observations by scaling emission estimates, or models of subsea permafrost degradation and in situ production. In one case, the main focus of the study was not on the ESAS (Warwick et al., 2016). Besides several ESAS-wide budget estimates, some studies gave emission estimates for parts of the shelf. The available estimates are summarized in Table 1. Budget estimates by Shakhova et al. far exceed those by subsequent studies. Several authors discussed the differences and attributed them to a variety of factors. Fenwick et al. (2017) stated that their study region (Chukchi Sea) was different from what Shakhova et al. focused on (East Siberian Sea and Laptev Sea), and that it is not underlain by permafrost or gas hydrates. This statement was based on Ruppel (2015), who assumed subsea permafrost extends only to less than 30 m depth based on a literature review on Arctic shelves. Fenwick et al. (2017) also stated that they did not target CH_4 release in polynyas, during ice breakup, during storm events and at hotspots, and that dilution with melt water may have decreased surface water CH_4 concentrations. Furthermore, they found that calculating diffusive sea-air CH_4 fluxes based on daily or instantaneous wind speed data, “as is often done”, would have biased their result by a factor of about 2. Instead, they averaged wind speeds 60 days prior to the measurement to better reflect the mixing of the surface layer. Li et al. (2017), like Fenwick et al. (2017), emphasize that their study area (Chukchi Sea) was different than that of the Shakhova group. Thornton et al. (2016b) focused on central parts of the East Siberian Sea, and stated that this may be more representative, especially for bubble transport, than the coverage by Shakhova et al., which focused more on shallower waters. The model study by Wåhlström and Meier (2014) neglected ebullition.

Knowledge gaps include the annual CH_4 budget of the ESAS, the magnitude of winter emissions (as campaigns mostly focused on ice-free seasons, apart from sparse data by Shakhova et al.), emissions of CH_4 built up under sea ice during ice melt, the role of polynyas and storms, the spatiotemporal distribution of hotspots (Fenwick et al., 2017), and differences between the Laptev, East Siberian and Chukchi Seas. In addition, there may also be considerable interannual variability, as Shakhova et al. (2005) reported a five-fold difference between potential summer CH_4 emissions in 2003 and 2004. Finally, import by the Kolyma River should be considered as a source of CH_4 in shelf waters.

Table 1: Estimates of the annual budget of CH_4 emissions from the ESAS to the atmosphere. More studies estimated flux rates without integrating them over a larger area (cf. Li et al., 2017; Table 1).

Study	Area	Annual budget [Tg CH_4 yr^{-1}]	Method
This study	ESAS (2.0×10^6 km^2)	0.4–1.5	Top-down
Shakhova et al. (2010a)	ESAS (2.1×10^6 km^2)	8	Upscaling
Shakhova et al. (2014)	ESAS	17	Upscaling
Berchet et al. (2016)	ESAS	0–4.5	Top-down
Thornton et al. (2016b)	ESAS	2.9	Upscaling
Warwick et al. (2016)	ESAS	"lower half of published estimated ranges (0.5 to 17 Tg yr^{-1})"	Top-down
Fenwick et al. (2017)	Eastern Chukchi Sea (2.1×10^5 km^2)	$(2.3 \pm 1.7) \times10^{-3}$	Upscaling; no hot spots
Li et al. (2017)	Chukchi Sea (5.95×10^5 km^2)	0.033	Upscaling
Wåhlström and Meier (2014)	Laptev Sea (5×10^5 km^2)	$(7.29 \pm 0.98) \times10^{-3}$	Process model of diffusive fluxes
Archer (2015)	ESAS	0.42	Process model

3 Inverse modeling of atmospheric CH_4 transport

Fluxes of CH_4 between the surface and the atmosphere cause variations of the atmospheric CH_4 mole fraction. These variations are transported in the atmosphere and can be detected downwind of a source (or sink) location. By calculating the inverse of the atmospheric transport process, atmospheric CH_4 signals can be used to infer the spatiotemporal distribution of surface-atmosphere-fluxes.

In this chapter, the basic concepts and methods used for estimating ESAS CH_4 emissions are introduced. The chapter also introduces important general limitations of the method.

3.1 Atmospheric CH_4 transport

In this section, the basics of atmospheric CH_4 transport in the context of source and sink estimation, as well as general limitations of transport models, are outlined.

3.1.1 Atmospheric tracer transport

CH_4 can be treated as a passive atmospheric tracer, which means that its presence does not influence its transport. Therefore, its transport can be treated as a linear problem. Atmospheric CH_4 transport can be divided into two processes: physical displacement, like advection with the mean wind, convection and turbulent diffusion, and consumption or production. Physical transport can be modeled based on meteorological fields, e.g. from mesoscale weather prediction models. For more details, the reader is referred to the literature on atmospheric tracer transport models (e.g. Lin et al., 2003). Production and/or consumption can be treated separately (Sect. 3.1.2).

3.1.2 Atmospheric CH_4 sinks

CH_4 is chemically oxidized in the atmosphere by several processes. The main sink is the reaction with the hydroxyl radical (OH), which accounts for about 90 % of atmospheric CH_4 consumption globally. OH is formed in a reaction sequence that starts with photolytic ozone dissociation (e.g. Cicerone and Oremland, 1988) and therefore varies seasonally.

Other sinks include reactions with chlorine radicals and atomic oxygen radicals in the stratosphere (~3 %), and reactions with chlorine radicals from sea salt in the marine boundary layer (~3 %) (Kirschke et al., 2013). Based on a back-of-the-envelope calculation, Yu et al. (2015) asserted that the chlorine sink in the Arctic marine boundary layer may be up to a third of the OH sink over the Arctic Ocean, due to low OH availability in the Arctic.

3.1.3 General limitations of inverse models of atmospheric tracer transport

Inverse modeling methods have a number of general limitations that naturally also apply to the results of this study. In this section, important limitations of the methods are outlined to help evaluate the results.

Variability between atmospheric tracer transport models

The accuracy of tracer transport models is a limitation on the accuracy of inversions. A recent study found significant differences between high-resolution transport models that were related to input meteorology and parameterization of vertical transport (Karion et al., 2018). Thus, inferred fluxes may be sensitive to which transport model was used in a study.

Stable stratification of the atmospheric boundary layer

The atmospheric boundary layer is the layer of the surface that is directly influenced by the surface and is characterized by fast mixing (timescale ~1 hour). This layer is particularly important for quantifying surface-atmosphere exchange processes because the fast mixing determines dispersion and ground-based stations measure tracers inside the atmospheric boundary layer.

Tracer transport in the atmospheric boundary layer is difficult to represent if the layer is not well mixed, e.g. when it is stably stratified due to a lack of turbulent mixing (Stull, 1988), which can be generated e.g. by surface heating or wind shear. In the Arctic, stably stratified boundary layers are often caused by temperature inversions due to the lack of surface heating by sunlight. This occurs especially during the polar night, and meteorology models are only moderately successful in capturing these temperature inversions (Kilpeläinen et al., 2012). Thus, it is desirable to filter out data that were obtained in a stably stratified boundary layer.

Local (near field) fluxes and representativeness of atmospheric data

Due to the limited resolution of atmospheric transport models and inverse models, errors can arise due to the mismatch of the spatial scale for which atmospheric data are representative and the model grid. Localized emissions in the far field are less problematic in this regard, since they produce signals that are similar to less localized emissions due to turbulent mixing, and thus their integrated strength can still be captured by an inverse model (F. Vogel, personal communication). However, localized emissions in the far field may be hard detect. By contrast, if local fluxes in the vicinity of a measurement location occur (the near field), an inverse model will erroneously assign the flux strength to a whole grid cell. Thus, models are unable to capture local emissions, and data that are strongly influenced by local emissions should be filtered out. In practice, this is difficult to achieve based on objective criteria (Sect. 5.1.3.2).

3.2 Inverse modeling theory

In this work, fluxes of CH_4 from the surface to the atmosphere are estimated based on atmospheric observations and atmospheric transport. The method is widely used in the field (cf. e.g. Kirschke et al., 2013). In Sect. 3.2.1, Bayesian inverse modeling theory is described in the context of CH_4 flux estimation based on measurements of atmospheric CH_4 mole fractions. In Sect. 3.2.2, limitations of the classical Bayesian approach are discussed, and Sect. 3.2.3 introduces how some of these limitations can be overcome by geostatistical inverse modeling.

3.2.1 Bayesian inverse modeling theory

In this section, inverse modeling theory is described based on Rodgers (2000).

In general, the unknown *state vector* $\boldsymbol{f}$, which is to be estimated, is related to *observations* $\boldsymbol{c}$ by a *forward function* $\boldsymbol{h}$:

$$\boldsymbol{c} = \boldsymbol{h}(\boldsymbol{f}) \tag{1}$$

Here, $\boldsymbol{c}$ denotes measured mole fractions of CH_4 in the atmosphere, $\boldsymbol{f}$ denotes the unknown surface fluxes of CH_4, and $\boldsymbol{h}()$ describes the processes that link the fluxes to the observations (transport of CH_4 in the atmosphere and the measurement). The formal solution of this problem is:

$$\boldsymbol{f} = \boldsymbol{h}^{-1}(\boldsymbol{c}) \tag{2}$$

Hence, the task is to invert the forward function $\boldsymbol{h}()$. Here, it is not known, but modeled by a *forward model* $\boldsymbol{H}$. Explicitely denoting *model-data mismatch* $\boldsymbol{\varepsilon}$, the relationship now reads:

$$c = H(f) + \boldsymbol{\varepsilon} \tag{3}$$

Here, $\boldsymbol{H}()$ is the *atmospheric transport model*, and the task is to find its inverse. However, this is generally an ill-posed problem. In particular, due to the presence of measurement error alone, a formal solution as in Eq. (2) does not exist for Eq. (3). This is overcome by finding an approximate solution $\hat{\boldsymbol{f}}$ by minimizing a *cost function* $J()$ for the difference between measured and modeled observations:

$$J(\boldsymbol{f}) = \|\boldsymbol{c} - \boldsymbol{H}(\boldsymbol{f})\|_{\boldsymbol{R}} \tag{4}$$

$$\hat{\boldsymbol{f}} = \underbrace{argmin}_{\boldsymbol{f}}\big(J(\boldsymbol{f})\big) \tag{5}$$

Here, $\|\cdot\|_{\boldsymbol{R}}$ denotes a norm, usually $\|\boldsymbol{\xi}\|_{\boldsymbol{R}} := (\boldsymbol{\xi}^T\boldsymbol{R}^{-1}\boldsymbol{\xi})$ with the *model-data mismatch covariance matrix* $\boldsymbol{R}$. In practice, possible error covariances in the difference between modeled and observed measurements are often neglected for simplicity. In this case, $\boldsymbol{R}$ is diagonal and describes measurement uncertainties and (the dominant) model errors.

However, Eq. (5) is usually underconstrained. In other words, the measurements do not uniquely constrain all elements of the state vector. This is the case for two reasons: First, atmospheric measurements are not sensitive to fluxes outside of their footprint (footprints are introduced in Sect. 5.1.4). Second, different distributions of fluxes $\boldsymbol{f}$ can result in the same observations $\boldsymbol{c}$, a problem that is known as equifinality. In simpler words, the measurements do not see fluxes downwind of the measurement location and a single observation cannot resolve where in the sampled area the signal originated.

A frequently used method for solving the underconstrained problem of inverting atmospheric transport is to minimize a regularized modification of the cost function, specifically adding a penalty term for deviations of the solution to a prior solution $\boldsymbol{f_a}$ (Tarantola, 1987):

$$J_a(\boldsymbol{f}) = \|\boldsymbol{c} - \boldsymbol{H}(\boldsymbol{f})\|_{\boldsymbol{R}} + \|\boldsymbol{f} - \boldsymbol{f_a}\|_{\boldsymbol{Q}} \tag{6}$$

Here, the norm $\|\cdot\|_{\boldsymbol{Q}}$ is analogous to $\|\cdot\|_{\boldsymbol{R}}$, but with *flux covariance matrix* $\boldsymbol{Q}$.

Minimizing $J_a()$ from Eq. (6) is commonly referred to as *Bayesian inverse modeling*, because fluxes optimized using $J_a()$ in Eq. (5) are equivalent to the Bayesian posterior probability distribution based on the prior probability distribution $\boldsymbol{f_a}$ (cf. Reum, 2012). Posterior fluxes should be interpreted as updates of the prior fluxes $\boldsymbol{f_a}$ with new information (atmospheric observations $\boldsymbol{c}$), since the "gaps" in the knowledge of the fluxes that is provided by the observations (described above) are "filled" by the prior fluxes. In this context, the flux covariance matrix $\boldsymbol{Q}$ can serve a special role, because off-diagonal elements describe spatial and temporal correlations of $\boldsymbol{f} - \boldsymbol{f_a}$. In other words, off-diagonal elements of $\boldsymbol{Q}$ define the spatiotemporal "range" of fluxes that can be estimated based on an observation, also outside of its footprint (see Sect. 5.1.4). More details on flux covariances are given in Sect. 3.2.3.3.

In order to facilitate numerical solution of minimizing J_b, atmospheric transport is represented by a linear model, i.e. $\boldsymbol{H}(\boldsymbol{f}) \rightarrow \boldsymbol{H} \cdot \boldsymbol{f} + \boldsymbol{c_{ini}}$. Here, $\boldsymbol{H}$ is the *atmospheric transport matrix* and $\boldsymbol{c_{ini}}$ are *boundary conditions* (more details in Sect. 5.1). The difference between observations $\boldsymbol{c}$ and boundary conditions $\boldsymbol{c_{ini}}$ is optimized and called $\boldsymbol{z}$**.** All probability distributions are assumed to be Gaussian. Posterior fluxes $\hat{\boldsymbol{f}}$ and and their covariance matrix $\boldsymbol{V_{\hat{f}}}$ thus become (e.g. Tarantola, 2005):

$$\hat{\boldsymbol{f}} = \boldsymbol{f_a} + \boldsymbol{QH}^T(\boldsymbol{HQH}^T + \boldsymbol{R})^{-1}(\boldsymbol{z} - \boldsymbol{Hf_a}) \tag{7}$$

$$\boldsymbol{V_{\hat{f}}} = \boldsymbol{Q} - \boldsymbol{QH}^T(\boldsymbol{HQH}^T + \boldsymbol{R})^{-1}\boldsymbol{HQ} \tag{8}$$

The linear Gaussian case will be used from here on throughout this study.

3.2.2 Shortcomings of Bayesian inverse modeling

An inherent problem of solving underconstrained problems is the dependence on prior knowledge. In classical Bayesian inverse modeling, prior knowledge takes the form of prior fluxes $\boldsymbol{f_a}$ and covariance matrices $\boldsymbol{R}$ and $\boldsymbol{Q}$. Biases in either quantity reduce the accuracy of estimated posterior fluxes.

Biased prior fluxes result in biased posterior fluxes, especially so where atmospheric data exert little influence on the result (i.e. where the footprint is small). The magnitude of CH_4

emissions from the East Siberian Arctic Shelf is poorly known (Sect. 2.6), which makes an unbiased prior estimate difficult to achieve.

In Sect. 3.2.1, error covariance matrices $\boldsymbol{R}$ and $\boldsymbol{Q}$ have been introduced, and the role of $\boldsymbol{Q}$ for regularizing posterior flux estimates briefly outlined. The matrix $\boldsymbol{Q}$ describes deviations of the unknown fluxes from the prior flux estimate $\boldsymbol{f_a}$. Hence, $\boldsymbol{Q}$ depends on the prior flux. As an illustration, consider the diurnal cycle of CO_2 exchange of a temperate forest with the atmosphere. If the prior flux is constant throughout the day, it can at best match the mean diurnal flux, and deviations between this model and actual fluxes will be larger than if the prior flux has a (realistic) diurnal cycle. In this sense, $\boldsymbol{Q}$ also describes shortcomings of the prior flux, and it should reflect actual flux processes. However, in practice, estimating $\boldsymbol{Q}$ can be difficult. For example, Rödenbeck et al. (2003) estimated spatial correlations of NEE based on model intercomparisons at 1275 km, while later studies, which were based on eddy covariance measurements, concluded that actual spatial correlations are much shorter (Chevallier et al., 2006, 2012; Kountouris et al., 2015).

3.2.3 Geostatistical inverse modeling

The poor prior knowledge on CH_4 emissions from the East Siberian Arctic Shelf (Sect. 2.6) makes an unbiased prior estimate as required by the classical Bayesian approach difficult. Therefore, methods that allow more data-driven and flexible ways to express prior knowledge were employed in this study known as geostatistical inverse modeling techniques. The geostatistical inverse modeling techniques used in here were adopted from work by the lab of Anna M. Michalak (specific citations in the text).

3.2.3.1 Regression model

In geostatistical inverse modeling, the formulation of the prior flux is different than in the classical Bayesian approach. Instead of a fixed prior flux estimate, a linear combination of predictor variables is included in the cost function (Michalak et al., 2004):

$$J_X(\boldsymbol{f},\boldsymbol{\beta}) = \|\boldsymbol{z} - \boldsymbol{Hf}\|_{\boldsymbol{R}} + \|\boldsymbol{f} - \boldsymbol{X\beta}\|_{\boldsymbol{Q}} \tag{9}$$

The *regression model* $\boldsymbol{X\beta}$, which takes the place of the prior fluxes, consists of the *regressor matrix* $\boldsymbol{X}$, the columns of which are here called *auxiliary variables* X_i, and the *regression model coefficients* $\boldsymbol{\beta}$. For the flux optimization, regression model coefficients $\widehat{\boldsymbol{\beta}}$ are computed that satisfy (Michalak et al., 2004):

$$(\boldsymbol{HX})^{\boldsymbol{T}}\boldsymbol{\Psi}^{-1}(\boldsymbol{HX})\widehat{\boldsymbol{\beta}} = (\boldsymbol{\Psi}^{-1}\boldsymbol{HX})^{\boldsymbol{T}}\,\boldsymbol{z}, \tag{10}$$

where

$$\boldsymbol{\Psi} = \boldsymbol{HQH}^T + \boldsymbol{R}. \tag{11}$$

The optimal regression model $\boldsymbol{X}\widehat{\boldsymbol{\beta}}$ is then used as an initial guess for the fluxes, i.e. the starting point for calculating optimized fluxes $\widehat{\boldsymbol{f}}$. Thus, each auxiliary variable is scaled to minimize the mismatch between regression model and posterior fluxes. Simply put, the prior flux is determined by the observations. Thus, this framework eliminates the need for an unbiased prior guess of the magnitude of the unknown fluxes. Instead, knowledge on spatiotemporal flux patterns is required.

The difference between optimized fluxes and regression model ($\hat{\boldsymbol{f}} - \boldsymbol{X}\hat{\boldsymbol{\beta}}$) is here called the *stochastic component* of the optimized fluxes.

Introducing the regression model can be viewed as introducing correlations in the posterior fluxes beyond the spatiotemporal correlations of the stochastic flux component, which is described by the flux covariance matrix $\boldsymbol{Q}$. In this sense, the regression model allows the observations to control the flux estimate outside of the range allowed in classical Bayesian inverse modeling, which is determined by footprint coverage and $\boldsymbol{Q}$.

3.2.3.2 Regression model selection

The ability to compare the performance of different regression models and selecting a best one is both a further step towards a more objective optimal prior (or initial) flux estimate and a tool for finding spatiotemporal patterns in the fluxes. Thus, model selection provides a means to gain knowledge about controls and processes governing of fluxes.

Evaluation metric BIC

A variety of methods for ranking regression models have been proposed (e.g. Ward, 2008). In this study, the Bayesian Information Criterion (BIC) was used as a score for model performance, since it rewards goodness of fit and penalizes model complexity. Therefore, BIC can help avoiding overfitting data with complex, hard to interpret regression models. A description was given e.g. by Yadav et al. (2013), which is summarized here. The criterion can be expressed as:

$$BIC = J_{BIC}(\hat{\boldsymbol{\beta}}) + p \cdot ln(n), \tag{12}$$

where p is the number of auxiliary variables (columns of $\boldsymbol{X}$), and n is the number of observations. The first addend, $J_{BIC}(\hat{\boldsymbol{\beta}})$, is the minimum value of the cost function

$$J_{BIC}(\boldsymbol{\beta}) = ln|\boldsymbol{\Psi}| + (\boldsymbol{z} - \boldsymbol{HX\beta})^T \boldsymbol{\Psi}^{-1} (\boldsymbol{z} - \boldsymbol{HX\beta}), \tag{13}$$

i.e. its value at the values of $\boldsymbol{\beta} = \hat{\boldsymbol{\beta}}$ that minimize the mismatch of the regression model with the atmospheric observations $\boldsymbol{z}$. Substituting in the solution $\hat{\boldsymbol{\beta}}$ yields:

$$BIC = ln|\boldsymbol{\Psi}| + \boldsymbol{z}^T \boldsymbol{\Xi} \boldsymbol{z} + p \cdot ln(n), \tag{14}$$

$$\boldsymbol{\Xi} = \boldsymbol{\Psi}^{-1} - \boldsymbol{\Psi}^{-1} \boldsymbol{HX} (\boldsymbol{X}^T \boldsymbol{H}^T \boldsymbol{\Psi}^{-1} \boldsymbol{HX})^{-1} \boldsymbol{X}^T \boldsymbol{H}^T \boldsymbol{\Psi}^{-1}. \tag{15}$$

Qualitatively, a small BIC score of a regression model indicates that it fits the atmospheric data well with a small number of auxiliary variables.

Since BIC and covariance matrices depend on each other (see also Sect. 3.2.3.3), these quantities should be iteratively optimized to obtain a best solution.

Interpretation of BIC

BIC is related to Bayes Factors for large numbers of observations, and thus differences in the BIC scores of models are a measure for the likelihood that a given model describes the data better than another (Kass and Raftery, 1995). Kass and Raftery (1995) suggest a scale for the interpretation of the difference between BIC for different models, which is based on Jeffreys (1961). On this scale, a difference of less than 2 indicates that there is no evidence for the better performance of a model, while a difference of more than 10 is called "decisive" evidence. These numbers are used as guidelines here.

The performance of models on the BIC scale can be expressed more formally via posterior probabilities of a model M (Ramsey and Schafer, 1997):

$$p''\left(M_j\middle|\boldsymbol{c}\right) = \frac{p'\left(M_j\right) \cdot e^{-BIC_j}}{\sum_i p'(M_i) \cdot e^{-BIC_i}}, \tag{16}$$

where $p'\left(M_j\right)$ denotes the prior probability of model M_j and $p''\left(M_j\middle|\boldsymbol{c}\right)$ denotes its posterior probability given the data $\boldsymbol{c}$. In the absence of prior knowledge on the models (i.e. $p'\left(M_j\right) \propto 1$), the posterior probability reduces to a function of BIC.

Collinearity checks

If the contributions of auxiliary variables to modeled atmospheric data (HX_j) are strongly collinear, regression coefficients are not stable against small perturbations, which hampers interpretation of the regression model. To detect collinearity, *Variance Inflation Factors (VIF)* are used here. The Variance Inflation Factor is the ratio of the variance of the regression coefficient of an auxiliary variable when fitting the full regression model and its variance when only fitting this particular variable (James et al., 2013). A threshold of $VIF > 5 \ldots 10$ indicates collinearity (James et al., 2013).

3.2.3.3 Covariance parameter estimation

As described in Sect. 3.2.2, estimating realistic covariance matrices for inverse models of atmospheric transport is difficult. To infer covariance matrices, the approach employed by Michalak et al. (2004) is adopted. In this approach, covariance matrices are parameterized, and the parameters estimated based on a restricted maximum likelihood approach (REML). The parameterization is presented in Sect. 5.1.6, while this section briefly outlines the optimization procedure.

The idea behind the optimization approach is to find covariance parameters $\boldsymbol{\theta}$ that maximize the probability of the observations $p(\boldsymbol{c}|\boldsymbol{\theta})$ (Michalak et al., 2004). Since this would require the as yet unknown posterior fluxes $\hat{\boldsymbol{f}}$ and regression model coefficients $\widehat{\boldsymbol{\beta}}$, these parameters are marginalized out by integrating over them:

$$p(\boldsymbol{c}|\boldsymbol{\theta}) = \int_{\boldsymbol{f}} \int_{\boldsymbol{\beta}} p(\boldsymbol{z}|\boldsymbol{f},\boldsymbol{\theta}) p'(\boldsymbol{f},\boldsymbol{\beta}|\boldsymbol{\theta}) d\boldsymbol{f} d\boldsymbol{\beta} \tag{17}$$

Here, $p(\boldsymbol{z}|\boldsymbol{f},\boldsymbol{\theta})$ is the probability of the observations given values for $\boldsymbol{f}$ and $\boldsymbol{\theta}$, and $p'(\boldsymbol{f},\boldsymbol{\beta}|\boldsymbol{\theta})$ is the joint prior probability of $\boldsymbol{f}$ and $\boldsymbol{\beta}$ given covariance parameters $\boldsymbol{\theta}$. In the abscence of prior knowledge on $\boldsymbol{\beta}$ (i.e. uniform probability), this probability is maximized by minimizing the cost function

$$L_{\boldsymbol{\theta}} = ln|\boldsymbol{\Psi}| + ln|\boldsymbol{X}^T\boldsymbol{H}^T\boldsymbol{\Psi}^{-1}\boldsymbol{H}\boldsymbol{X}| + \boldsymbol{z}^T\boldsymbol{\Xi}\boldsymbol{z} \tag{18}$$

with $\boldsymbol{\Psi}$ and $\boldsymbol{\Xi}$ as defined in Eq. (11) and (15), respectively. The optimal parameters $\widehat{\boldsymbol{\theta}}$ are the ones that minimize $L_{\boldsymbol{\theta}}$.

3.2.4 Non-negative posterior fluxes

In this study, sinks of atmospheric CH_4 are accounted for by modifying boundary conditions and footprints (Sect. 5.1.4). Therefore, negative fluxes (i.e. surface sinks of CH_4) would be unrealistic. Therefore, fluxes were restricted to positive values, which can greatly regularize the solution (Miller et al., 2014a). The implementation of the non-negativity constraint was adopted from Miller et al. (2014a), using Lagrange-multipliers, with the modification that the optimization was based on an L-BFGS-B- algorithm (Byrd et al., 1995) (Scot M. Miller, personal communication).

4 Year-round accurate measurements of atmospheric greenhouse gases at Ambarchik

To improve data coverage of the East Siberian Arctic Shelf, the new atmospheric greenhouse gas observation station Ambarchik was established. In this section, the measurements performed at Ambarchik, as well as processing, calibration and quality control of the data are presented. Data analysis is not included in this chapter; the CH_4 data that were used for estimating CH_4 emissions from the East Siberian Arctic Shelf in Chapter 5 are presented therein. The material presented in this chapter is an edited version of parts of a manuscript that was submitted to the journal Atmospheric Measurement Techniques. The manuscript is currently in review and available online as a discussion paper (Reum et al., 2018a). Here, the parts of the manuscript that are relevant in the context of this thesis are presented with minor edits. The work was performed in collaboration with Mathias Göckede, Jost Lavric, Olaf Kolle, Sergey Zimov, Nikita Zimov, Martijn Pallandt and Martin Heimann. Author contributions are as follows: MH, SZ and MG conceptualized the study. JL, MH, OK, NZ, FR and MG designed and set up the Ambarchik station. NZ and SZ coordinated setup and maintenance of the Ambarchik station. FR and MP performed calibration experiments. FR curated and analyzed the data. FR prepared the manuscript with contributions from all authors. MG supervised the project, and reviewed and edited the manuscript.

Quality control of Ambarchik data revealed shortcomings in a standard calibration approach of the greenhouse gas analyzer employed at the station, namely the correction of reported CO_2 and CH_4 mole fractions for the effects of water vapor in the sampled air stream. To address the shortcomings, an improved water correction method was developed and applied to data from Ambarchik. This work was described in a manuscript that is currently under review for Atmospheric Measurement Techniques as well (Reum et al., 2018b). Since the biases corrected with this new water correction method were small in comparison to the large signals investigated in this study, it is only briefly covered in the quality-control part of this chapter and in the appendix.

4.1 Station description

4.1.1 Area overview

Ambarchik is located at the mouth of the Kolyma River, which opens to the East Siberian Sea (69.62° N, 162.30° E; Fig. 1). The majority of the landscape in the immediate vicinity of the locality is wet tussock tundra. On ecoregion scale, Ambarchik is bordered by the Northeast Siberian Coastal Tundra ecoregion in the West, the Chukchi Peninsula Tundra ecoregion in the East, and the Northeast Siberian Taiga ecoregion in the South (ecoregion definitions from Olson et al., 2001). Major components contributing to the net carbon exchange processes in the area are tundra landscapes including wetlands and lakes, as well as the Kolyma River and the East Siberian Arctic Shelf.

Fig. 1: Ambarchik station location. Background based on Copernicus Sentinel data from 2016. Courtesy Martijn Pallandt (figure from Reum et al., 2018a).

4.1.2 Site overview

Ambarchik hosts a weather station operated by the Russian meteorological service (Roshydromet), whose staff is the entire permanent population of the locality. The closest town is Chersky (~100 km to the south, population 2,857 as of 2010), with no other larger permanent settlement closer than 240 km. The site therefore does not have any major sources of anthropogenic greenhouse gas emissions in the near field. The only regular anthropogenic CO_2 and potentially CH_4 sources that may influence the measurements are from the Roshydromet facility, including the building that hosts the power generator and the inhabited building.

The atmospheric carbon observation station Ambarchik started operation in August 2014. It consists of a 27 m-tall tower with two air inlets and meteorological measurements, while the majority of the instrumentation is hosted in a rack inside a building. The rack is equipped for temperature control, but due to the risk of overheating, it is open most of the time and thus in equilibrium with room temperature (room and rack temperature are monitored). Atmospheric mole fractions of CH_4, CO_2, and H_2O are measured by an analyzer based on the cavity ring-down spectroscopy (CRDS) technique (G2301, Picarro Inc.), which is calibrated against WMO-traceable reference gases at regular intervals (Sect. 4.2.2). The tower is located 260 m from the shoreline, with a base elevation of 20 m a.s.l. (estimated based on GEBCO_2014 (Weatherall et al., 2015), which in this region is based on GMTED2010 (Danielson and Gesch, 2011)).

4.1.3 Gas handling

The measurement system allows switching between two different air inlets and four different calibration gas tanks (Fig. 2). Component manufacturers and models of the individual components are listed in Table A.1.

Air inlets are mounted on the tower at 27 (“Top”) and 14 m a.g.l. (“Center”), respectively, and are equipped with 5 µm polyester filters (labels F1 and F2 in Fig. 2). The two air inlets are probed in turns (15 minutes Top, 5 minutes Center). Signals from the Center Inlet are mainly used for quality control purposes (Sect. 4.2.4). Air is drawn from the inlets (I1, I2) through lines of flexible tubing (6.35 mm outer diameter) by a piston pump located downstream of the measurement line branch (PP1). The cycles of the pump are smoothed by a buffer with a volume of about 5 liters. The combined flow through both inlet lines is about 17 l/min, monitored by a flow meter (FM1) and limited by a needle valve (NV1). The tubing enters the house at a distance of about 15 m from the tower. The air passes 40 µm stainless steel filters (F3, F4), behind which the sample line is branched from the high flow line using a solenoid valve (V1).

The sample line (between filters F3/F4 and the CRDS analyzer) is composed exclusively of components made of stainless steel; they include tubing (SS tube 1/8”), two 2 µm filters (F5, F6), a needle valve for sample flow regulation (NV2, usually fully open), a pressure sensor (P1), and a flow meter (FM2). Air is drawn from the high flow line into the sample line by a membrane pump downstream of the CRDS analyzer (MP1).

Calibration gases pass through a line composed exclusively of stainless steel components as well. Air from gas tanks (High, Middle, Low, Target) passes through pressure regulators (RE1–4), reducing their pressure roughly to ambient pressure. This way, the CRDS analyzer can cope with the pressure difference between sample air and calibration air from the tanks without an open split, which would normally be installed to equilibrate the line with ambient pressure. This setup was chosen in order to conserve calibration air. The lines from the gas tanks are connected to a multiposition valve (MPV1), which is used to select between gas tanks. Downstream of the multiposition valve, the calibration gas line is connected to the sample line by a solenoid valve (V3). The solenoid valves V2 and V3 are used to select between sample air from the tower and calibration air.

During calibrations, the part of the measurement line that is not part of the calibration line is continuously flushed by the high flow pump (PP1) through the purge line, which comprises solenoid valve V4 (which shuts off air flow from the gas tanks through the purge line in case of a power outage during a tank measurement), needle valve NV3 (which is used to match the purge flow to the usual sample flow), and flow meter FM3 (which monitors the purge flow).

The flow meters (FM1–3) and pressure sensor (P1) are used to diagnose problems such as weakening pump performance, clogged filters, leaks or obstructions.

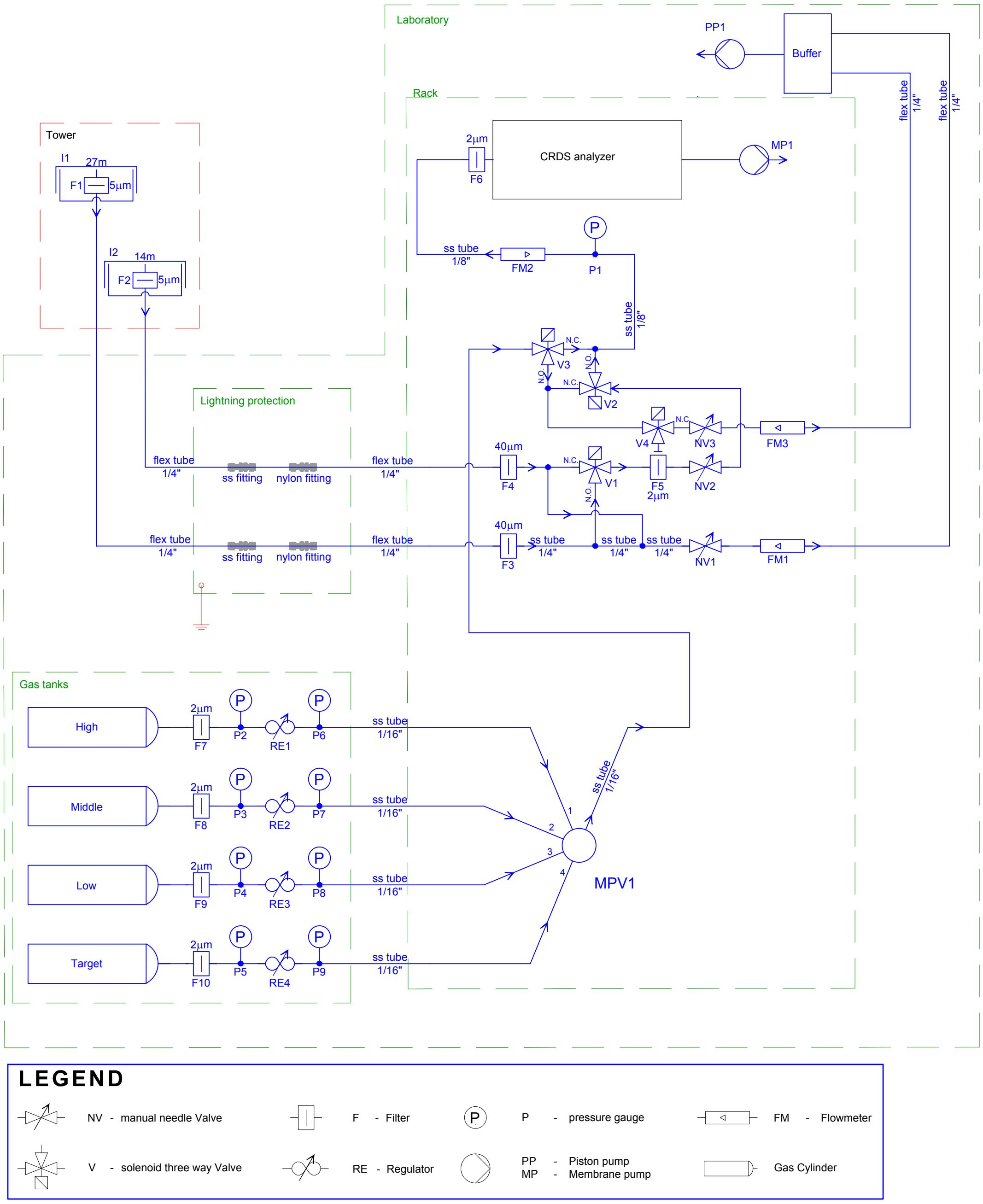

Fig. 2: Air flow diagram of Ambarchik greenhouse gas measurement system. See Sect. 4.1.3 for a description of component abbreviations (figure from Reum et al., 2018a).

4.1.4 Meteorological measurements

Meteorological measurements performed by MPI-BGC at Ambarchik include wind speed and direction at 20 m a.g.l., air temperature and humidity at 20 and 2 m a.g.l., and air pressure at 1 m a.g.l. (instruments listed in Table A.2). The measurements mainly serve to monitor atmospheric conditions like wind and stability of atmospheric stratification for quality control of the GHG data (described in Sect. 4.2.4). The 2D sonic anemometer, which is used to measure wind speed and direction, features a built-in heating to prevent freezing. The heating is switched on if temperature decreases below 4.5 °C and relative humidity is higher than 85 %, and switched off when temperatures increase above 5.5 °C.

4.2 Quality control

4.2.1 Water correction

In order to minimize maintenance efforts and reduce the number of components prone to failure, CO_2 and CH_4 mole fractions are measured in humid air. Hence, the values reported by the analyzer have to be corrected for the effects of water vapor to obtain dry air mole fractions. This is done by applying a water correction function to the raw data:

$$\boldsymbol{c_{dry}} = \frac{\boldsymbol{c_{wet}}(\boldsymbol{h})}{f_c(\boldsymbol{h})} \tag{19}$$

Here, $\boldsymbol{c_{wet}}$ is the mole fraction of CO_2 or CH_4 in humid air reported by the analyzer, h is the water vapor mole fraction (also measured by the CRDS analyzer), $f_c(\boldsymbol{h})$ is the water correction function, and $\boldsymbol{c_{dry}}$ is the desired dry air mole fraction. Picarro Inc. provides a factory water correction based on Chen et al. (2010), but to achieve accuracies within the WMO goals for water vapor mole fractions above 1 % H_2O, custom coefficients must be obtained for each analyzer (Rella et al., 2013). Here, we employ the novel water correction method by Reum et al. (2018b). Results are briefly summarized here, while more details are given in Appendix A.2.

Water correction experiments have been performed in 2014, 2015 and 2017. Differences between the water corrections based on the different experiments were on the order of magnitude of the WMO goals (Fig. 3). Given the small number of experiments conducted so far, it is unknown whether these differences represent drifts over long time scales, short-term variations and/or systematic differences between the experimental methods. Therefore, water correction coefficients were derived based on the averages of the individual water correction function responses for each species. The maximum deviations of the individual functions to the synthesis functions were 0.018 % CO_2 at 3 % H_2O, which corresponds to 0.07 ppm at 400 ppm dry air mole fraction, and 0.034 % CH_4 at 2.7 % H_2O, which corresponds to 0.7 ppb at 2000 ppb dry air mole fraction (Fig. 3).

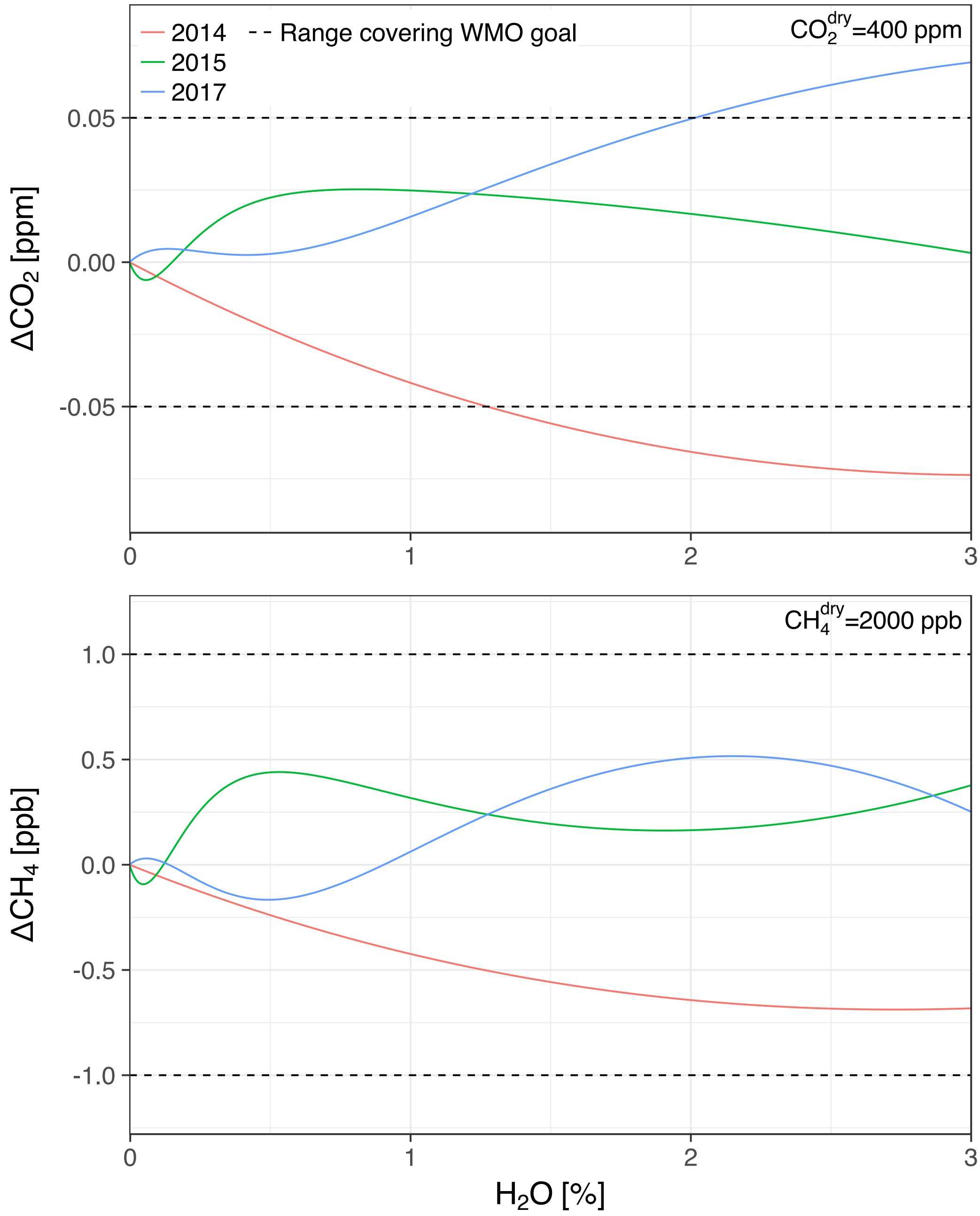

Fig. 3: Differences between individual water correction functions and the synthesis water correction function at dry air mole fractions of 400 ppm CO_2 and 2000 ppb CH_4. The dashed lines correspond to the WMO internal reproducibility goals (in the case of CO_2 in the northern hemisphere), a value that incorporates uncertainties in transferring the calibration scale from the highest level of standards to working standards and other uncertainties, for example related to gas handling (WMO, 2016) (figure from Reum et al., 2018a).

4.2.2 Calibration

Calibrations are performed with a set of pressurized dry air tanks filled at the Max Planck Institute for Biogeochemistry (Jena, Germany). The levels of GHG mole fractions of these tanks have been traced to the WMO scales X2007 for CO_2 and X2004A for CH_4 (Table A.4). Three calibration tanks (High, Middle, Low) are probed every 116 hours for 15, 10 and 10 minutes, respectively. The longer probing time of the first (High) tank serves to flush residual water molecules that adhere to the inner tubing and filter surfaces. From these three tanks, coefficients for linear calibration functions are derived. Due to the scatter of the coefficients over time, the coefficients are smoothed using a tricubic kernel with a width of 120 days (Fig. A.1). Individual measurements are calibrated by applying the smoothed coefficients, interpolated linearly in time. The impact of the smoothing on the calibration of ambient mole fractions is smaller than 0.02 ppm CO_2 and 0.3 ppb CH_4 (one standard deviation). The fourth tank (Target) is probed every 29 hours for 15 minutes. Its calibrated CO_2 and CH_4 mole fraction measurements (Fig. 4) serve as quality control of the calibration procedure (Sect. 4.2.3). Uncertainties associated with the calibration procedure, as well as possible future improvements, are discussed and quantified in Appendix A.5.

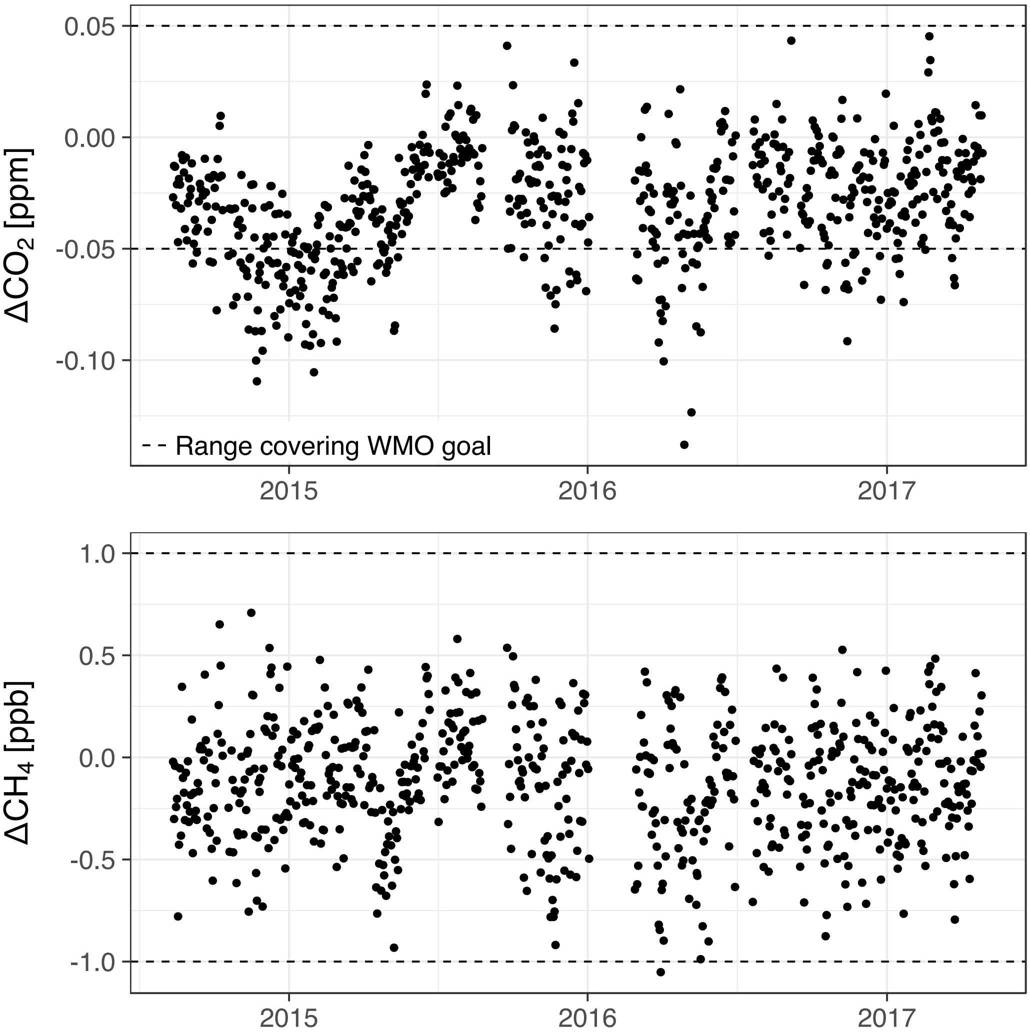

Fig. 4: Target tank bias over time for CO_2 and CH_4. As in Fig. 3, the dashed lines cover the WMO internal reproducibility goals (figure from Reum et al., 2018a).

4.2.3 Uncertainty in CO_2 and CH_4 measurements

Measurement uncertainties in the CO_2 and CH_4 data arise from instrument precision, the calibration and the water correction. We estimated time-varying uncertainties of hourly trace gas mole fraction averages based on the method by Andrews et al. (2014), with some modifications. Details of the procedure are given in Appendix A.5.

Average uncertainties at 1σ-level were 0.11 ppm CO_2 and 0.75 ppb CH_4. Both were dominated by the variability between the water vapor correction experiments at high water vapor mole fractions. These values may slightly underestimate the uncertainties due to errors that could not be fully quantified based on the available data, which is subject to future research (Appendix A.5). On the other hand, they slightly overestimate the uncertainties since the uncertainty due to water vapor may be overestimated at low water vapor mole fractions and because the increase in precision achieved by averaging calibration coefficients from multiple calibration episodes was ignored (Appendix A.5). Thus, the uncertainties given here are likely close to those estimated if the abovementioned factors are taken into account.

4.2.4 Data screening

After water correction and calibration, invalid data are removed before calculating hourly averages using filters for bad analyzer status (Sect. 4.2.4.1), flushing of lines (Sect. 4.2.4.2), times of calibration and maintenance, contamination from local polluters (Sect. 4.2.4.3) and water vapor spikes (Sect. 4.2.4.4). Additional variables reported in the hourly averages allow for further data screening, e.g. for using the data in inverse models (Table 2). Details on the gradient of virtual potential temperature are given in Sect. 4.2.4.5.

Table 2: Variables for data screening and a suggestion for a strict filter for background conditions.

Variable	Background filter example
Mole fractions without removing CO_2 spikes	Remove flagged spikes
Difference between inlets	$\lvert\Delta CO_2\rvert < 0.1$ ppm; $\lvert\Delta CH_4\rvert < 2$ ppb
Intra-hour variability	$\sigma(CO_2) < 0.2$ ppm; $\sigma(CH_4) < 4$ ppb
Gradient of virtual potential temperature	$\Delta T_{v,p} < 0$ K
Wind speed	$w_v > 2$ ms^{-1}
Time of day	1 pm – 4 pm

4.2.4.1 Analyzer status diagnostics

Picarro Inc. provides the diagnostic flags INST_STATUS and ALARM_STATUS that monitor the operation status of the analyzer. The values in Table 3 indicate normal operation. The flag ALARM_STATUS indicates both exceeding user-defined thresholds for high mole fractions (ignored here), and data flagged as bad by the data acquisition software. The code reported in INST_STATUS contains, among other indicators, thresholds for cavity temperature and pressure deviations from their target values. We created stricter filters for these two values based on their typical variation during normal operation of this particular measurement system. Occasionally, small numbers (< 5) of outliers are recorded after a period of lost data (e.g. due to high CPU load). These are removed manually.

Table 3: Diagnostic values indicating normal status of the CRDS analyzer.

Quantity	Filter
INST_STATUS	INST_STATUS = 963
ALARM_STATUS	ALARM_STATUS < 65536
Cavity temperature	$\lvert T_c - 45° C \rvert < 0.0035$ K
Cavity pressure	$\lvert p_c - 186.65$ hPa$\rvert < 0.101$ Pa

4.2.4.2 Flushing of measurement lines

Air from the two inlets at the tower and the calibration tanks flows through some common tubing (Fig. 2). Hence, air measured immediately after a switch is influenced by the previous air source. We remove the first 30 seconds from the record after a switch between inlets to avoid sample cross-contamination. Air from calibration tanks exhibits larger differences in humidity and mole fractions to ambient air. Hence, the first five minutes of ambient air measurements after tank measurements are removed from the record.

4.2.4.3 Contamination from local polluters

Possible frequent contamination sources in the immediate vicinity of the tower are the building hosting the power generator of the facility (65 m northwest from tower) and the heating and oven chimneys of the only inhabited building (30 m and 20 m northeast, respectively). These local polluters can cause sharp and short increases in CO_2 (and, depending on the source, CH_4) mole fractions on the timescale of seconds to a few minutes. These features cannot be modeled by a regional or global atmospheric transport model and should therefore be filtered out. We developed a detection algorithm to identify spikes based on their duration, gradients, and amplitude in the raw CO_2 data. Spike detection algorithms are often compared to manual flagging by station operators (El Yazidi et al., 2018). Parameters of our algorithm were tuned in this way based on the first year of data. Large CH_4 spikes often coincided with CO_2 spikes. Hence, the spike detection algorithm was developed for CO_2 and used to flag both CO_2 and CH_4, although this may remove some unpolluted CH_4 signals. The algorithm is described in Appendix A.4. The impact of the CO_2 spike flagging procedure is shown in Table 4. Impacts on the hourly mole fractions are small, more so when considering only data that pass other quality filters.

Table 4: Fraction of hourly averages of data from the Top inlet that contain flagged CO_2 spikes, and impact of removing them before averaging (ΔCO_2, ΔCH_4).

Metric	All data	Data with $w_v > 2$ ms^{-1} and $\Delta T_{v,p} < 0$ K
Cases that contain flagged spikes	15 %	6 %
Cases where $\Delta CO_2 > 0.1$ ppm	4 %	< 1 %
Cases where $\Delta CH_4 > 2$ ppb	< 1 %	< 1 %
Mean / median ΔCO_2	0.16 / 0.03 ppm	0.07 / 0.02 ppm
Mean / median ΔCH_4	0.5 / 0.03 ppb	0.2 / 0.02 ppb

4.2.4.4 Water vapor spikes

During winter, the CRDS analyzer occasionally records H_2O spikes with durations of a few seconds. The spikes typically exhibit much higher mole fractions than possible given ambient air temperature. This suggests that they are caused by small amounts of liquid water in the sampling lines in the laboratory upon evaporation. Since we observed the phenomenon exclusively during the cold season, we speculate that it is caused by small ice crystals that may form on the air inlet filters (F1, F2), detach, are trapped by one of the filters inside the laboratory, and evaporate.

Since fast water vapor variations deteriorate the accuracy of the water vapor correction, we remove the spikes before creating hourly averages. Spikes are identified using a flagging procedure similar to the one for CO_2 contamination described in Appendix A.4, with parameters adapted to the different shape of the H_2O spikes.

4.2.4.5 Virtual potential temperature

Regional and global scale atmospheric tracer transport models rely on the assumption that the boundary layer is well-mixed (e.g. Lin et al., 2003). This requirement is not satisfied when the air is stably stratified due to a lack of turbulent mixing (Stull, 1988). This may occur when the virtual potential temperature increases with height. To detect these situations, sensors for temperature and relative humidity are installed at 2 m and 20 m above ground level on the measurement tower (Table A.2). Based on these measurements, the virtual potential temperature is calculated for both heights, and the difference can be used as an indicator for stable stratification of the atmospheric boundary layer at the station (e.g. Table 2).

4.3 Summary

The site Ambarchik has been operational without major downtime since its installation in August 2014. Greenhouse gas measurements are calibrated about every five days using dry air from gas tanks with GHG mole fractions traced to WMO scales. Mole fractions of CO_2

and CH_4 are measured in humid air and corrected for the effects of water vapor using a novel water vapor correction method. An algorithm was developed to remove measurements influenced by local polluters, which affected a small fraction of the measurements. Measurements of the gradient of the virtual potential temperature and the two sampling heights allow for detection of stable stratifications of the atmospheric boundary layer at the station. Uncertainties of the GHG measurements, which were estimated based on measurements of dry air from calibrated gas tanks and water correction experiments, were on average 0.11 ppm CO_2 and 0.75 ppb CH_4, with potential improvements by future analyses and experiments. Thus, the CO_2 uncertainties were on the order of the WMO inter-laboratory compatibility goal in the northern hemisphere (0.1 ppm CO_2), while the CH_4 uncertainty was well within the WMO goal of 2 ppb CH_4. The accuracy of the CO_2 and CH_4 data obtained at Ambarchik make the Ambarchik station a highly valuable tool for carbon cycle studies in Northeast Siberia like estimating CH_4 emissions from the East Siberian Arctic Shelf to the atmosphere.

5 Methane emissions from the East Siberian Arctic Shelf to the atmosphere

In this chapter, CH_4 emissions from the East Siberian Arctic Shelf to the atmosphere are estimated based on the literature, concepts, methods and data introduced in the previous chapters. The chapter consists of a description of the model and its inputs, model results and their interpretation. Conclusions are given in Chapter 6.

5.1 Model description

In this section, the model used to estimate ESAS CH_4 emissions is introduced. It includes a brief overview of the implementation of the inverse modeling techniques outlined in Chapter 3, a description of the domain, atmospheric data, the model of atmospheric CH_4 transport, boundary conditions and covariance model. Lastly, in Sect. 5.1.7, a set of auxiliary variables is developed to describe the ESAS CH_4 emission processes introduced in Chapter 2, as well as terrestrial CH_4 emissions in the domain.

5.1.1 Optimization code

The code that implemented the GIM techniques described in Sect. 3.2.3 used in this work was developed by Miller et al. (2014b). This code, implemented mainly in MATLAB, features flux optimization, model selection, covariance parameter estimation, and the restriction to non-negative fluxes.

5.1.2 Domain

The domain extent for flux optimization was chosen to encompass the East Siberian Arctic Shelf and adjacent land areas so that none of the atmospheric observation stations is close to the domain boundary (Fig. 5). Other studies only included the Russian part of the Chukchi Sea (Shakhova et al., 2010a), but here, the East Siberian Arctic Shelf is defined as the area covering the Laptev Sea, the East Siberian Sea and the Chukchi Sea (similarly to Thornton et al., 2016b). Definitions of the three seas were taken from Spalding et al. (2007). Since this definition of the ESAS includes some small areas beyond the shelf (ocean depths dropping to 3000 m), the area was restricted to waters shallower than 500 m. This definition encompasses a total extent of 2.0×10^6 km^2. Another 1.2×10^6 km^2 in the domain is covered by other ocean areas. Adjacent land areas are tundra and taiga ecoregions, making up 1.9×10^6 km^2 in the domain.

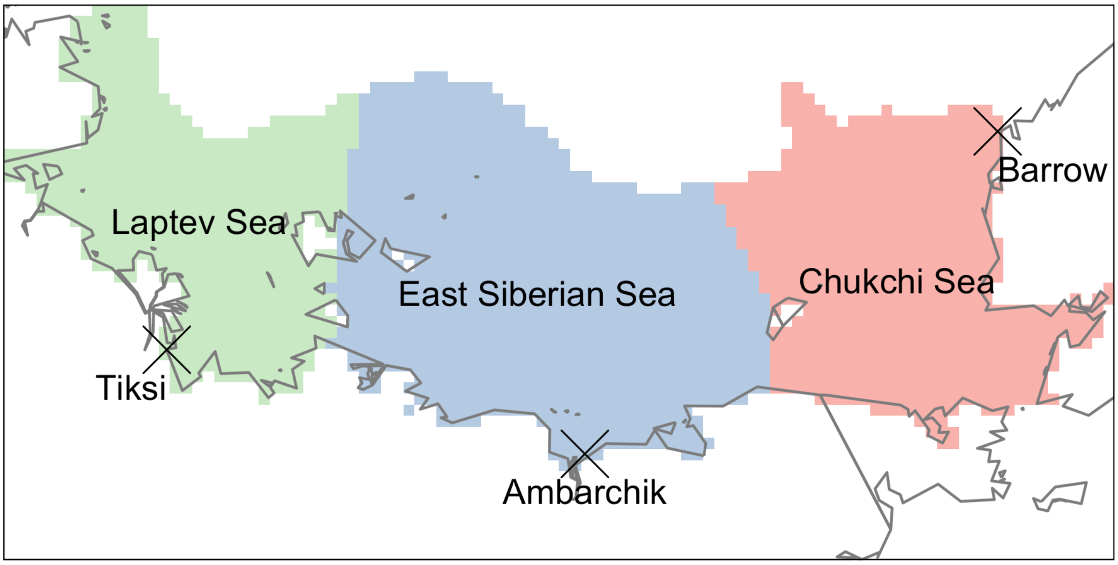

Fig. 5: Domain with the regions of the East Siberian Arctic Shelf and the atmospheric observation stations used for optimizing CH_4 emissions.

For the domain, a Lambert Azimuthal Equal Area projection (e.g. Evenden, 1990) was used, because in this projection, every grid cell has the same area. The choice of resolution for fluxes was guided by practical considerations of computational resources, and was set to 32 km × 32 km × 1 day. The period of optimization was July 2014 to December 2015. Table 5 shows the full domain definition.

Table 5: Definition of the spatiotemporal domain used in this study.

Projection (proj-string)	+proj=laea +lat_0=70 +lon_0=150 +ellps=WGS84
Extent (xmin, xmax, ymin, ymax)	-1200 km, 2000 km, -300 km, 1300 km
Spatial resolution	32 km
Number of grid cells (nx, ny)	100, 50
Area	5.1×10^6 km^2
Period	2014-07-01 – 2015-12-31
Temporal resolution	1 day
Number of time periods (nt)	549
Length of state vector (nx·ny·nt)	2,745,000

5.1.3 Atmospheric data

5.1.3.1 Stations

We used data from the three stations Ambarchik, Barrow and Tiksi to estimate CH_4 emissions in this study. Ambarchik (AMB) data were extensively described in Chapter 4, and an overview and references for all stations are given in Table 6. The data are shown in Fig. 6.

Table 6: Atmospheric CH_4 observations used in this study.

Station	Institution	Location	Inlets (a.g.l.)	Data coverage	Reference
Ambarchik	MPI-BGC	69.62N, 162.30E	14 m, 27 m	2014-08-09 – ongoing	(Reum et al., 2018a)
Tiksi	AARI, FMI	71.60N, 128.89E	10 m	2010 – ongoing	(Uttal et al., 2013)
Barrow	NOAA	71.32N, 156.61W	16.5 m	1986 – ongoing	(Dlugokencky et al., 1995)
SWERUS-C3 expedition	Stockholm University	See reference	4 m, 9 m, 15 m, 20 m, 35 m	2014-07-11 – 2014-08-17	(Thornton et al., 2016b)

Tiksi and Barrow were, during the period modeled here, the only other continuously operating atmospheric carbon observation stations located at the coast of the East Siberian Arctic Shelf. There is another station close to Chersky, about 120 km inland of Ambarchik. Chersky has been operated by NOAA until 2016, but has large data gaps in the study period. Therefore, it was not used to infer fluxes from the East Siberian Arctic Shelf here.

Data from the SWERUS-C3 expedition, which collected CH_4 data from the Siberian Arctic in summer 2014 (Fig. 7), were used for validation. From this data set, data from the upper two inlets were used, since these fell into the second level of the atmospheric transport model. Data from lower inlets, which were similar to those of the upper inlets (Thornton et al., 2016b), were ignored.

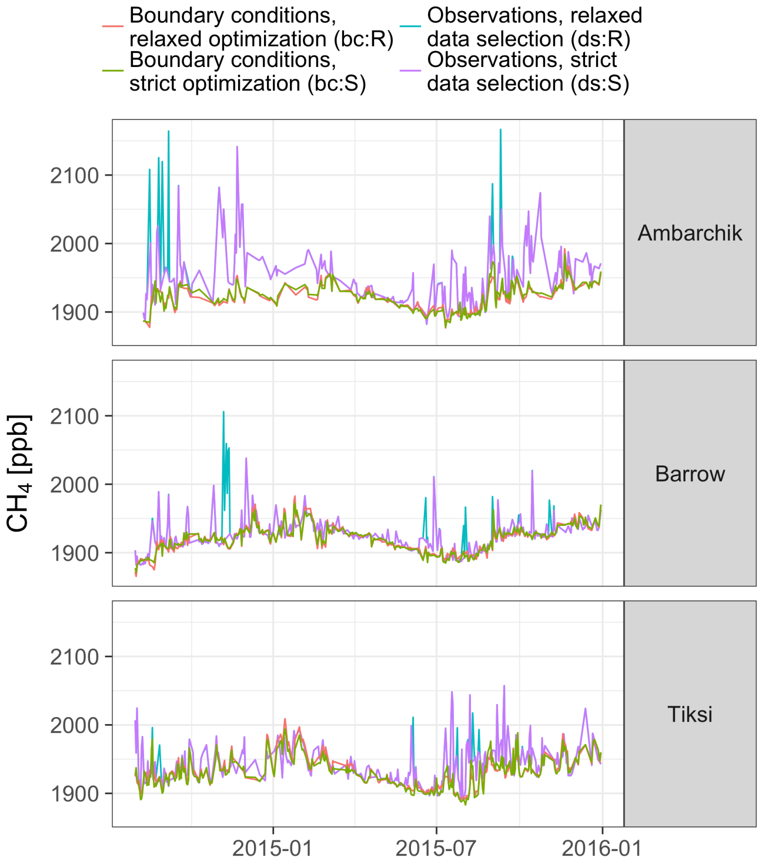

Fig. 6: Atmospheric data and boundary conditions used for optimizing fluxes in this study (daytime averages). Shown here are observations for two different data selection criteria (Sect. 5.1.3.2) and two different versions of boundary conditions (Sect. 5.1.5).

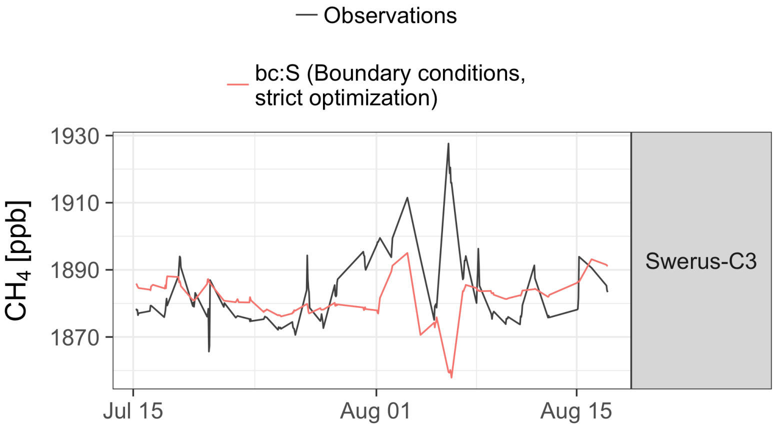

Fig. 7: Hourly averages of CH_4 observations from the SWERUS-C3 campaign and boundary conditions (strict optimization, see Sect. 5.1.5).

5.1.3.2 Atmospheric data selection criteria

In this section, the criteria that were used to select data for optimizing fluxes are described. Models of atmospheric tracer transport rely on several assumptions that not all atmospheric observations fulfill (see Sect. 3.1.3 for an overview). First, a set of filters was applied to the hourly data. To summarize, the filters included in all cases a daytime filter, as well as criteria for temperature gradients and wind speed. Additional criteria for the variability of CH_4 observations were used in some model runs, labeled "strict atmospheric data selection" ("ds:S"). In other model runs, these variability filters were omitted ("relaxed atmospheric data selection" or "ds:R"). Of these criteria, strict data selection (ds:S) represented a data set with all filters aimed at removing the influence of the near field. However, since the criteria are somewhat subjective, relaxed data selection was used to investigate whether strict data selection removed significant signals that the model was able to retrieve. Daily averages of the remaining data were used for optimization if almost all hourly data passed the quality filters. The data selection criteria are summarized in Table 7. Details on the individual filters are given below.

Table 7: Atmospheric data selection criteria.

Data selection criterion	Label	Applied filters	Number of daily averages that pass
Relaxed data selection	ds:R	Hourly: Daytime Temperature inversions (only Ambarchik) Wind speed Daily: "Clean day"	Ambarchik: 234 Barrow: 352 Tiksi: 329 (total: 915)
Strict data selection	ds:S	All of the above plus variability criteria	Ambarchik: 226 Barrow: 336 Tiksi: 322 (total: 884) SWERUS-C3: 19

Temperature gradients and daytime filter

To detect stably stratified boundary layers, temperature gradients were examined where available (Ambarchik, Barrow). At both sites, average temperature gradients had a seasonal cycle that indicated fewer temperature inversions during summer, which is expected due to the seasonal cycle of solar heating of the surface. They also exhibited a diurnal cycle, indicating the smallest fraction of measurements affected by temperature inversions was between 8 am and 4 pm local time on average (Ambarchik: < 30 %, Barrow: < 60 %). Based on these results, only daytime data from 10 am to 4 pm were used for modeling (the delay in the morning allows for some mixing of the newly formed turbulent layer) for all stations. Seasonal variations in the diurnal cycle of average temperature gradients were ignored here because they would have resulted in throwing out all winter data (December-January-February). Instead, results based on winter data are reported, but they may be less accurate than those for summer.

In addition to the general daytime filter, data obtained during temperature inversions were removed from the Ambarchik record, but not from Barrow. At Barrow, this would have restricted the usable data almost exclusively to the period from May to September, throwing out data points outside of this period that were classified by the station operators as "background" signals.

Wind speed

In many inverse models of atmospheric tracer transport, data obtained in calm air are not used. The reason behind this filter is the potential influence of local fluxes, which can build up to large signals in calm air locally. Dlugokencky et al. (1995) used a threshold of 1 ms^{-1} for analyzing the Barrow CH_4 timeseries, while Sweeney et al. (2016) used a threshold of 3 ms^{-1} for Barrow for inferring trends in it. Here, we used a threshold of 3 ms^{-1} for Barrow and Ambarchik, following Sweeney et al. (2016), while for Tiksi a threshold of 2.5 ms^{-1} was used, following the recommendation by station operators (Tuomas Laurila, personal communication).

CH_4 mole fraction variability

Highly variable CH_4 mole fractions may indicate emissions in the near field of a station that cannot be resolved by the model. Since one assumption of inverse models of atmospheric tracer transport is well-mixedness, signals that are difficult to model may be detected by short-term variability or differences between air sampled at different heights within the atmospheric boundary layer. Thresholds for both criteria are somewhat subjective. The former was used e.g. by Sweeney et al. (2016), who discarded data with an intra-hour variability of $1\sigma > 10$ ppb from the Barrow record for analyzing long-term changes in the CH_4 data. On the other hand, Thonat et al. (2017) used no data filter at all for a study about the detectability of CH_4 emissions from different sources in the Arctic. In this study, the impact of a variability data filter on the results is explored by performing inversions with and without variability filters (“strict” vs. “relaxed” data selection).

Differences between air inlets were taken into account where available, i.e. at Ambarchik. As for short-term variability, the practical implementation of the filter is subjective. One may argue that they should not exceed the WMO inter-laboratory compatibility goals.

However, in Ambarchik, air is not sampled simultaneously at both inlets, so differences can arise for other reasons like gradients in time, and too strict a data filter carries the risk of discarding events that could be resolved by the model (Steve Wofsy, personal communication). Therefore, a criterion of $|\Delta CH_4| < 5$ ppb was chosen based on the 10 ppb-threshold for intra-hour variability and the ratio of the median intra-hour variability and median absolute difference between the inlets. This "mixing"-criterion was used jointly with the variability criterion.

“Clean day”

A daily average was used for optimization only if all or all but one of the hourly daytime data points of this day passed the filters summarized above. The purpose of this last filter was to select for data with consistently favorable conditions throughout the day.

Criteria for SWERUS-C3 data

Data from the SWERUS-C3 expedition are distributed with quality control applied, including a filter for wind speeds above 2 ms^{-1}. In addition, the variability filter was applied, although its effect was negligible (one daily average was 3.8 ppb lower due to this filter). For consistency, the “clean day” filter for daily averages was applied as well.

5.1.4 Atmospheric transport

Inverse atmospheric transport was computed using the setup presented in Henderson et al. (2015). The model was based on the 'Stochastic Time-Inverted Lagrangian Transport' model STILT (Lin et al., 2003) coupled to WRF (Skamarock et al., 2008) and driven by the MERRA reanalysis (Rienecker et al., 2011). The resolution of the transport model in the domain was mostly 10 km horizontally, using 41 vertical levels. For each observation, backtrajectories of 500 particles were computed over 15 days. Surface influence of a particle was calculated as the time spent in the lower half of the atmospheric boundary layer. Backtrajectories were provided by John Henderson (AER). From these backtrajectories, the surface influence based on all particles ("footprint") was calculated for the domain used for flux optimization.

Atmospheric CH_4 chemistry (Sect. 3.1.2) was implemented by sampling reaction rates along the back trajectories and computing the cumulative CH_4 loss for both boundary conditions and footprints. Reaction rates were taken from Nuñez Ramirez (2019, in prep.).

Two sets of trajectories were used: one used the full 15 days, the other only the first 5 days. This differentiation was initially included to investigate differences. This was ultimately not pursued in depth, but there were small differences so both settings were kept as plausible implementations of the transport.

5.1.5 Boundary conditions

Backtrajectories were terminated at the domain boundary or after their specified maximum lifetime (5/15 days, see Sect. 5.1.4) was reached, at which point their CH_4 mole fraction was initialized.

Boundary conditions were derived from global CH_4 mole fraction fields from Nuñez Ramirez (2019, in prep.). They were obtained from a forward run of the TM3 model with CH_4 fluxes optimized using the Jena Inversion System. Fluxes were optimized for ground-based stations including the stations used for optimizing fluxes in this study in order to capture their baselines.

Two sets of boundary conditions were used. The first, herein referred "strict boundary condition optimization" ("bc:S"), was computed based on the global CH_4 mole fraction field obtained with optimized fluxes using the standard settings for covariance matrices $\boldsymbol{R}$ and $\boldsymbol{Q}$ of the global inverse model. Since this setting created some (unrealistic) negative CH_4 fluxes, another global CH_4 mole fraction field was used, which was optimized with the same setup but a 100-fold increase of the weight of the prior flux estimate. Thus, the constraint of the data on these boundary conditions was relaxed. Hence, these are referred to as "relaxed boundary condition optimization" ("bc:R").

The boundary conditions exhibited differences on synoptic and seasonal scales that were much larger than typical measurement uncertainties for hourly values (standard deviations of 3.8–5.6 ppb per station; Fig. 8). Thus, using both settings constituted a test for robustness of results against transport model and data uncertainties.

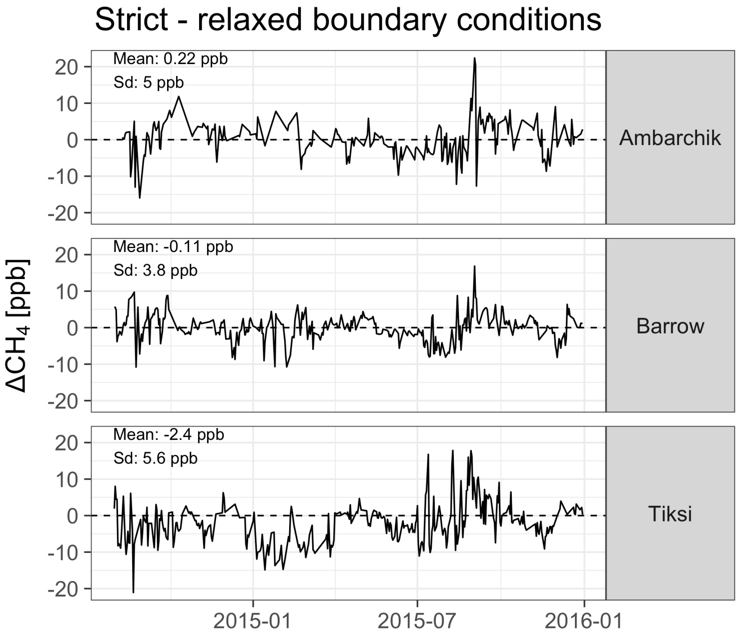

Fig. 8: Difference between strict and relaxed boundary condition optimization. Shown here are the values for 5-day backtrajectories and strict atmospheric data selection.

5.1.6 Spatiotemporal covariance model

As in many inverse modeling studies, the flux covariance matrix $\boldsymbol{Q}$ was based on the assumption that the stochastic flux component correlates over certain scales in length and time (Sect. 3.2.1). The flux covariance matrix $\boldsymbol{Q}$ was implemented using the decomposition into spatial and temporal correlations used by Yadav and Michalak (2013):

$$\boldsymbol{Q} = \sigma_Q \cdot \boldsymbol{D}_\tau \otimes \boldsymbol{E}_\xi \tag{20}$$

Here, $\boldsymbol{D}$ is the temporal covariance matrix, $\boldsymbol{E}$ is the spatial covariance matrix, $\otimes$ denotes the Kronecker product, and σ_Q is the square root of the variance of the fluxes. Often, exponential covariance models are chosen for $\boldsymbol{D}$ and $\boldsymbol{E}$. However, this way $\boldsymbol{Q}$ has many small, but no non-zero elements. By contrast, a spherical covariance model is zero beyond the correlation length, which makes covariance parameter estimation computationally less expensive (Kitanidis, 1997). Therefore, spherical covariance models were used here:

$$C_{ij}^{sph} = \begin{cases} 1 - 1.5 \cdot \dfrac{d_{ij}}{\delta} + 0.5 \cdot \left(\dfrac{d_{ij}}{\delta}\right)^3, & 0 \leq \dfrac{d_{ij}}{\delta} \leq 1 \\ 0, & \text{otherwise} \end{cases} \tag{21}$$

Here, C_{ij} denotes the elements of a covariance matrix ($\boldsymbol{D}$ and $\boldsymbol{E}$ in Eq. (20)), d_{ij} is the distance between elements i and j of the matrix, and δ is a distance parameter (τ and ξ in Eq. (20)). For spatial correlations, d_{ij} and δ are spatial lengths, referring to distances between cells of the spatial grid on which fluxes are estimated, while for temporal correlations, they are time differences.

The spatial covariance model was modified to remove correlations between land and ocean fluxes (Fig. 9):

$$D_{ij} = D_{ij}^{sph} \cdot \left(1 - \left|l_i - l_j\right|\right), \tag{22}$$

where l_i denotes the fraction of the grid cell i that is covered by land.

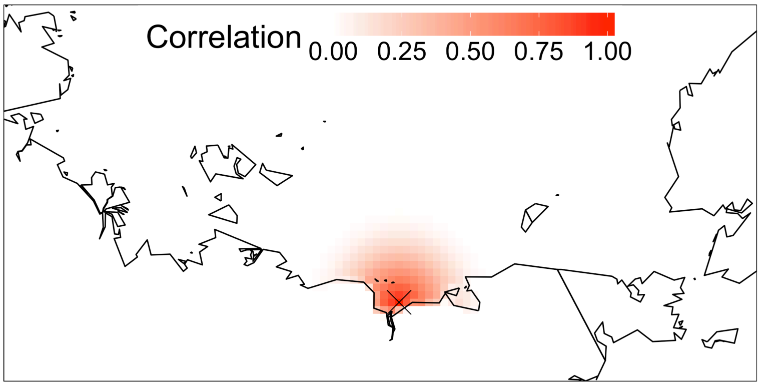

Fig. 9: Spatial correlations for one grid cell (marked by the cross), illustrating the decoupling of land and ocean in the covariance model used for optimizing fluxes.

5.1.7 Description of CH_4 emission processes using auxiliary variables

The processes that may govern CH_4 emissions from the ESAS to the atmosphere were described in Sect. 2. For the regression model of the geostatistical method (Sect. 3.2.3), these processes were described by various datasets, all of them restricted spatially to the ESAS (that is, in all regression models, ocean emissions outside of the ESAS were 0). For a full model of the CH_4 emissions in the domain, terrestrial fluxes have been described in the same way. A summary of all auxiliary variables used in this study is provided in Table 8.

Table 8: Brief descriptions of all auxiliary variables. Full descriptions and references are in the text.

Label	Description
ESAS spatial distribution of subsea emissions	
Hot spots	Hot spot map based on Shakhova et al. (2010a)
Const. ESAS	Constant ESAS emissions
ESAS<30m	Area of ESAS shallower than 30m
ESAS>30m	Area of ESAS deeper than 30m
Edge	ESAS edge (100 m – 500 m depth)
Diffusive gas transfer	
k	Gas transfer velocity
Ocean depth	
exp-10m	Exponential attenuation with ocean depth ($\alpha = 0.1\ m^{-1}$)
exp-20m	Exponential attenuation with ocean depth ($\alpha = 0.05\ m^{-1}$)
exp-100m	Exponential attenuation with ocean depth ($\alpha = 0.01\ m^{-1}$)
Sea ice	
Const. ESAS-Ice	ESAS fraction not covered by sea ice
Ice growth	Sea ice growth
Ice retreat	Sea ice retreat
Storms	
Storms-0.5-10	Storm occurrence ($d = 0.5\ m^{-1}s$, $w_{v,0} = 10\ ms^{-1}$)
Storms-1-10	Storm occurrence ($d = 1\ m^{-1}s$, $w_{v,0} = 15\ ms^{-1}$)
Storms-0.5-15	Storm occurrence ($d = 0.5\ m^{-1}s$, $w_{v,0} = 10\ ms^{-1}$)
Storms-1-15	Storm occurrence ($d = 1\ m^{-1}s$, $w_{v,0} = 15\ ms^{-1}$)
Kolyma mouth	
Kolyma mouth	Location of Kolyma mouth
Combinations of variables	
exp-10m-ice	"exp-10m" modulated by sea ice cover
exp-20m-ice	"exp-20m" modulated by sea ice cover
exp-100m-ice	"exp-100m" modulated by sea ice cover
ESAS<30m-ice	"ESAS<30" modulated by sea ice cover

ESAS>30m-ice	"ESAS>30" modulated by sea ice cover
Edge-ice	"Edge" modulated by sea ice cover
Hot spots-ice	"Hot spots" modulated by sea ice cover
Ice growth-edge	"Ice growth" multiplied with "Edge"
k-exp-10m	"k" multiplied with "exp-10m"
k-exp-20m	"k" multiplied with "exp-20m"
k-exp-100m	"k" multiplied with "exp-100m"
Process-based wetland models	
WSL	Climatology of CH_4 emissions based on model LPJ-WSL
SDGVM	Climatology of CH_4 emissions based on model SDGVM
DLEM	Climatology of CH_4 emissions based on model DLEM
ORCHIDEE	Climatology of CH_4 emissions based on model ORCHIDEE
LPJ-GUESS	Climatology of CH_4 emissions based on model LPJ-GUESS
Lake model	
bLake4Me	Climatology of CH_4 emissions based on model bLake4Me
Simple models for terrestrial emissions	
Const. land	Constant land emissions
SWM	Simple Wetland Model
ZCM	Zero Curtain Model

5.1.7.1 Oceanic CH_4 emissions

Hot spots ("Hot spots")

In previous studies, ESAS CH_4 emissions were divided into hot spot and background regions, linking hot spots to increased ebullition due to degraded permafrost cover. Thus, regions where seabed warming is above average (fault zones, river beds) are candidates for CH_4 emission hot spots (Sect. 2.6). Here, we used the most extensive dataset of observed CH_4 emission hot spots in the literature, which is the map by Shakhova et al. (2010a). Since we could not obtain the data from the authors directly, the data were extracted from the published plot. This dataset only covers the Laptev and East Siberian Seas. Datasets of the distribution of fault zones (cf. Nicolsky et al., 2012) or paleo-river beds (Frederick and Buffett, 2014) were not considered.

Spatial distributions of subsea permafrost, hydrate or gas ("Const. ESAS", "ESAS<30m", "ESAS>30m")

Several studies scaled up locally measured ESAS CH_4 emissions to the whole shelf area (Shakhova et al., 2010a, 2014; Thornton et al., 2016b). Therefore, one candidate for the spatial distribution of CH_4 emissions from the seabed associated with permafrost distribution was the geographical extent of the ESAS as introduced in Sect. 5.1.2 ("Const. ESAS"). However, there may be considerable spatial variations since the permafrost distribution in the seabed of the shelf may not be uniform. In several Arctic shelves, permafrost extends no further than about 20 m water depth, which lead Ruppel (2015) to work with an assumed permafrost extent to 30 m water depth (Sect. 2.1.2). Two implications are possible: the lack of a permafrost cover may enable CH_4 from gas hydrates or natural gas pools to migrate to the water, which would explain gas flares (Cramer and Franke, 2005; Portnov et al., 2013) (cf. Sect. 2.1.2). Furthermore, permafrost thaw may be less advanced in shallower parts of the shelf, since they were inundated more recently (Archer, 2015 and refrences therein; Portnov et al., 2013). On the other hand, widespread CH_4 seepage on the outer part of the shelf was not confirmed in the East Siberian Sea by one study (Thornton et al., 2016b), and the lack of subsea permafrost carbon may constitute a lack of carbon as substrate for methanogenesis (Sect. 2.2.1). Based on these considerations, two more candidates for the spatial distribution of CH_4 emissions were added, splitting the ESAS into areas where the ocean was shallower ("ESAS<30m") and deeper ("ESAS>30m"), respectively, than 30 m.

Shelf edge ("Edge")

At the shelf edge, CH_4 may escape due to exposure to warmer water temperatures (Sect. 2.2.1). The candidate variable describing CH_4 emissions from the shelf edge was defined as the part of the ESAS between 100 m and 500 m depth. The variable was still based on a preliminary ESAS definition that ignored the restriction to the ecoregion definition and thus included a slightly larger area (Appendix B).

Gas transfer velocity: proxy for turbulent diffusion ("k")

Turbulent diffusion (Sect. 2.5) was described following the approach by Nuñez Ramirez (2019, in prep.), who based the gas transfer velocity on Sweeney et al. (2007).

The functional dependence of the gas transfer velocity k follows Wanninkhof (1992):

$$k = 0.27 \cdot w_v^2 \cdot \left(\frac{Sc}{660}\right)^{-0.5}, \tag{23}$$

$$Sc = \frac{\mu}{\rho D} \tag{24}$$

Here, w_v is the wind speed at the surface, Sc the Schmidt number, μ the dynamic viscosity and ρ the density of seawater, and D the diffusion coefficient. These values were computed using the R package "marelac" version 2.1.6 (https://CRAN.R-project.org/package=marelac) based on wind speed, sea surface temperature and surface pressure taken from ERA-Interim (Dee et al., 2011). Sea surface salinity was set to a constant value of 35 g kg^{-1}. Variability of salinity was ignored because of data availability and its small impact (Wanninkhof, 1992).

This gas transfer velocity estimate mostly followed the square of the wind speed (correlation coefficient 0.99). Using 3-hourly wind speeds may introduce errors both due to ignoring the impact of instantaneous wind speeds (Wanninkhof, 1992), as well as ignoring the large-scale state of mixing of the water column, which would be better described by averaged wind speeds (Fenwick et al., 2017).

Since spatiotemporal variations of the partial pressures of CH_4 on both sides of the air-ocean interface are poorly known, turbulent diffusion was described solely based on the gas transfer velocity. This approach serves as a test whether wind speed dominates the CH_4 emission patterns.

Ocean depth: proxy for ebullition, terrestrial organic matter input and the pycnocline ("exp-10m", "exp-20m", "exp-100m")

CH_4 released from the seabed in the form of bubbles dissolves on the way through the water column. The fraction of CH_4 that reaches the air-water interface depends on several factors that are not well constrained (Sect. 2.3.2). However, as a general statement, the fraction decreases with ocean depth. Hence, this process was described by a simple exponential relationship:

$$f_{CH_4} \sim e^{-\alpha d} \tag{25}$$

where d is ocean depth. The attenuation factor α describes all mechanisms that control how much CH_4 dissolves on the way through the water column. Archer (2015) used $\alpha = \frac{1}{30}\, m^{-1}$. We computed auxiliary variables for several values of α:

$$\alpha \in (0.1\, m^{-1}, 0.05\, m^{-1}, 0.01\, m^{-1}) \tag{26}$$

Since the ESAS generally gets deeper with increasing distance to the coast, these variables result in coverage of a narrow strip along the coasts to a large fraction of the shelf area. Hence, terrestrial organic matter input may also be described by Eq. (25), since it is more prevalent closer to the coasts (cf. Sect. 2.1.1 and 2.2.2) and may provide a carbon source for CH_4 production (Paul Mann, personal communication).

Furthermore, this set of auxiliary variables may also be considered to describe the pycnocline that traps bottom-released CH_4 below a certain depth.

Sea ice barrier ("Ice")

To describe the physical sea ice barrier (Sect. 2.4), the remote-sensing sea ice concentration product ASI-SSMI (Kaleschke et al., 2001; Spreen et al., 2008) was used, which is distributed with a resolution of 12.5 km, spatially and temporally interpolated, and with a 5-day median filter applied (Kern et al., 2010).

Deep-water mixing processes: sea ice growth and storms ("Ice growth", "storms-XX-YY")

Several studies indicate that deep-water mixing may be a dominant process governing CH_4 release from Arctic shelves to the atmosphere, since it breaks the stable stratification that usually traps CH_4 below the surface (Sect. 2.3.1). In Arctic shelf seas, both storms (Shakhova et al., 2014) and sea ice growth (Sect. 2.4) have been identified as drivers of deep-water mixing. Heat loss has been identified as a driver for mixing in a shallow water reservoir (Liu et al., 2016), but was ignored here after first unsuccessful tests.

Sea ice growth. Sea ice growth was described by the differences between consecutive time steps of the sea ice concentration product; averaged over five days because the product had a five-day-median filter applied to it (Kern et al., 2010). This approach, postulating a quasi-instantaneous link between ice formation and CH_4 emissions, was not suitable for describing mixing of the complete water column to the average depth of the ESAS, which occurs on a timescale of months (Janout et al., 2016). However, it may capture mixing of upper water layers (Markus Janout, personal communication) or CH_4 release from brine (Sect. 2.4). This approach is conflated with increasing sea ice concentration at a given location due to drift. Although this may indicate high wind speeds that can likewise induce mixing, this represents another process and therefore reduces the quality of this variable. The problem was partly mitigated by applying a temporal filter that restricts the variable to times of overall growth of the Arctic sea ice cover. Thus usually corresponds to the period from September (annual Arctic sea ice minimum extent) to March (annual Arctic sea ice maximum extent). The final formulation reads:

$$f_{CH_4} \sim \begin{cases} abs\left(min\left(\bar{\Delta}_{sea\ ice\ conc.}, 0\right)\right), & \text{total Arctic sea ice extent increases} \\ 0, & \text{otherwise} \end{cases} \tag{27}$$

Shortcomings of this approach are sensitivity to noise of the sea ice concentration product and the conflation with drift during the period not excluded by the filter for increase of total Arctic sea ice extent. In addition, a better indicator for induced mixing would be the increase in sea ice volume.

Storms. Storms with wind speeds above about 15 ms^{-1} were previously suggested to induce considerable deep-water mixing of the ESAS (Shakhova et al., 2014). In the ERA-interim wind speed product used for the gas transfer velocity (see above), this applies to 0.5 % of all ocean voxels in the domain and period of this study. Although storms were already represented by the auxiliary variable describing the gas transfer coefficient, we tested whether the relationship changed at high wind speeds using a variable that attributed emissions only to periods of high wind speeds. Since only a small number of voxels was affected, a variable indicating the presence of a storm was used rather than a functional relationship increasing with wind speed. For this purpose, we used a logistic growth function with sharp transitions between wind speeds that were assigned weight 0 and those that were assigned weight 1:

$$f_{CH_4} \sim \left(1 + e^{-d\left(w_v - w_{v,0}\right)}\right)^{-1}. \tag{28}$$

Four combinations of coefficients were considered: $d \in (0.5,1)\, m^{-1}s$ and $w_{v,0} \in (10, 15)\, ms^{-1}$.

Winter ESAS emissions

The sea ice barrier in winter is not entirely impermeable. Most notably, parts of the ESAS remain open throughout the winter, especially the Great Siberian Polynya. In addition to opening the barrier, refreezing in leads can induce brine rejection and mixing similar to the sea ice growth period (Sect. 2.4). Large openings should be reflected in the sea ice concentration product, but smaller openings may not be captured adequately. This shortcoming may be addressed in a follow-up study by describing the spatiotemporal distribution of open water areas in the Arctic sea ice (e.g. Wang et al., 2016) or ice production within them. We accounted for the possibility of winter emissions by including candidate auxiliary variables that do not vary with sea ice cover, i.e. assuming constant emissions throughout the year. The role of sea ice permeability was not explicitly accounted for.

Sea ice retreat ("Ice retreat")

Methane accumulated below or in sea ice in winter may be released upon ice breakup (Sect. 2.4). This process was modeled similarly to sea ice growth based on differences between consecutive time steps of the sea ice concentration product (see above):

$$f_{CH_4} \sim max(\bar{\Delta}_{sea\ ice\ conc.}, 0) \tag{29}$$

Shortcomings of this approach are that it may be sensitive to noise in the sea ice concentration product, accumulation times are ignored, and that the resulting variable is sensitive to both sea ice melt and sea ice drift. Since melting sea ice results in a melt-water layer and potentially the release of CH_4 stored within sea ice (Sect. 2.4), these are two distinctly different processes, which may impact the performance of this candidate variable negatively.

Kolyma river mouth

Methane emissions associated with the Kolyma river mouth were represented by a manually created candidate variable. The spatial distribution was based on published measurements of CH_4 emissions in the area (Shakhova and Semiletov, 2007, Fig. 6) and corresponds to the location of the Kolyma mouth and the Kolyma gulf. The variable was not varied with time.

5.1.7.2 Terrestrial CH_4 emissions

For a complete description of CH_4 emissions in the study domain, terrestrial emissions had to be taken into account. The most important CH_4 sources at high northern latitudes are wetlands (e.g. Kirschke et al., 2013), but recently, lake emissions have come into focus as well (e.g. Wik et al., 2016). In addition, the importance of cold season emissions is emerging (Kittler et al., 2017; Mastepanov et al., 2013; Zona et al., 2016). Anthropogenic CH_4

emissions play a smaller role in the sparsely populated domain of this study and were ignored. The following land emission candidate variables were considered:

Process-based wetland CH_4 emission models ("SDGVM", "LPJ-WSL", "DLEM", "ORCHIDEE", "LPJ-GUESS")

Several process-based wetland CH_4 emission models were considered: several submissions to the WETCHIMP intercomparison (experiment 2) (Melton et al., 2013; Wania et al., 2013 and references therein), i.e. SDGVM, LPJ-WSL, DLEM and ORCHIDEE. In addition, LPJ-GUESS (Zhang et al., 2013, with updated climate forcing) was considered. For all models, climatologies were created, since model results in the period of interest were not available (WETCHIMP: 2000–2004, LPJ-GUESS: 2010–2014).

Simple Wetland Model ("SWM")

In addition to the complex process-based wetland CH_4 emission models, a simple Kaplan-type wetland model (Kaplan, 2002; Pickett-Heaps et al., 2011) was created based on the approach by Miller et al. (2014b). Miller et al. (2014b) incorporated a factor representing the presence of wetlands in a grid cell. However, maps of wetland extent have strong differences in Siberia (Bohn et al., 2015). Therefore, no map of wetland extent was used, and soil water content was used as an indicator for the magnitude of CH_4 emissions. Another factor, describing soil carbon content and turnover time, was ignored as well. Thus, the model read:

$$f_{CH_4} \sim w \cdot F \cdot e^{\frac{-309}{T-227}} \tag{30}$$

Here, w is soil water content, T is soil temperature in K, and F is an emission factor depending on soil temperature (see Miller et al. (2014b) for a full description). Thus, input datasets for this model were soil temperature and soil water content, which were taken from ERA-Interim. Following Miller et al. (2014b), the values of soil layer 2 (7–28 cm depth) were used. In addition to the simplifications described above, a shortcoming of this model is that modeled soil temperatures can be strongly biased during the cold season in permafrost regions (Chadburn et al., 2017). This was addressed with the Zero Curtain Model (see below).

Zero Curtain Model ("ZCM")

Zero curtain CH_4 emissions (Zona et al., 2016) from wetlands were modeled with a simple model tuned to roughly match cold season emissions measured using the Eddy covariance technique at a site near Chersky (Kittler et al., 2017) that were not captured by the Simple Wetland Model (SWM) described above. However, the ERA-Interim soil temperature data used as input did not feature a zero curtain period, i.e. modeled soil temperatures dropped below 0 °C without pause. Therefore, the zero curtain period was modeled using a functional temperature dependence that was not intended to represent real processes, but to roughly reproduce the seasonal variations at the Eddy site near Chersky. The presence of wetlands was modeled as in the simple wetland model, yielding:

$$f_{CH_4} \sim w \cdot max(T_{start} - T, 0)^2 e^{\frac{-max(T_{start} - T, 0)^2}{2(T_{start} - T_{max})^2}} \tag{31}$$

$$T_{start} = 5°\mathrm{C} \tag{32}$$

$$T_{max} = -1°\mathrm{C} \tag{33}$$

This function assigns emissions at soil temperatures below T_{start} with maximum emissions at T_{max}. The function is slightly asymmetric with a longer tail towards low temperatures (half points: -8.9 °C and 0.9°C). To exclude the thaw period, a filter restricted emissions from this variable to periods when the soil temperature was falling during the previous month.

Process-based lake CH_4 emission model ("bLake4Me")

Lake CH_4 emissions were described by monthly emission estimates from the model bLake4Me (Tan et al., 2015), averaged over the years 2005–2008 (Zeli Tan, personal communication).

Fire and anthropogenic emissions

Fire and anthropogenic CH_4 emissions are small in the study area and were ignored.

5.1.7.3 Combinations of variables

Since model selection can only combine candidate variables additively, a number of candidate variables were created by combining those described in the previous sections multiplicatively. Combinations were between variables that described the sea ice barrier (i.e. open ocean fraction), variables that described turbulent diffusion (e.g. gas transfer) velocity) or ebullition (e.g. exponential functions of ocean depth), and between variables that described spatial heterogeneity of fluxes (e.g. exponential functions of ocean depth) and diffusion (see Table 8).

5.1.8 Parameter sets for regression model selection and inversions

Regression models were computed and evaluated for different settings for atmospheric data selection, boundary conditions and backtrajectory length to allow evaluation of the robustness of the results against model settings. The parameter sets for model selection are outlined in Table 9.

Table 9: Parameter sets for regression model selection. Definitions of the atmospheric data selection criteria and boundary condition optimization are given in the respective sections referenced below.

Parameter set label	Atmospheric data selection (Sect. 5.1.3.2)	Boundary condition optimization (Sect. 5.1.5)	Backtrajectory length
ds:S-bc:S-bl:5	Strict	Strict	5
ds:S-bc:S-bl:5	Strict	Strict	15
ds:S-bc:R-bl:15	Strict	Relaxed	5
ds:R-bc:S-bl:5	Relaxed	Strict	5
ds:R-bc:S-bl:15	Relaxed	Strict	15

5.2 Results

5.2.1 Sensitivity of atmospheric observation network to ESAS emissions

Based on the backtrajectories run for 5 or 15 days, the atmospheric observations were most sensitive to the area on the order of few hundreds of kilometers around the measurement locations (Fig. 10). Northern parts of the Laptev and East Siberian Seas, as well as the southern Chukchi Sea were scarcely sampled. All stations intensely sampled both the ESAS and adjacent terrestrial ecoregions.

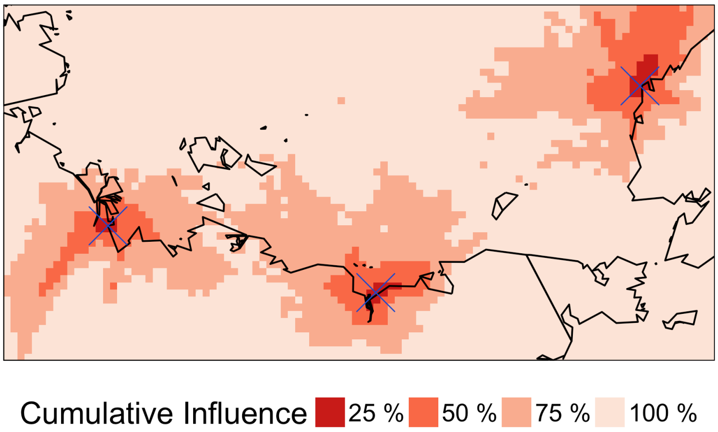

Fig. 10: Footprints of the atmospheric data used for optimization in this study, aggregated over the whole study period and sorted into bins covering 25 % of the cumulative influence each. Shown here is the case for strict atmospheric data selection and 5-day backtrajectories (see Table 9 for definitions).

5.2.2 Covariance parameters

Covariance parameters were estimated based on the restricted maximum likelihood method (Sect. 3.2.3.3) for several atmospheric data selection criteria and preliminary regression models. The results for prior uncertainty and model-data mismatch mostly depended on data selection (Fig. 11, left panel). Correlation length and time varied considerably for the case of relaxed data selection, in one case converging on a correlation time of 0 days (Fig. 11, right panel). Since covariance parameter estimation was computationally expensive, we opted for one set of parameters per atmospheric data selection version (Table 10). For relaxed data selection, we chose the parameter set with a shorter correlation length, because this was closer to the settings of a previous study on high latitude CH_4 emissions that employed the same method (Miller et al., 2016).

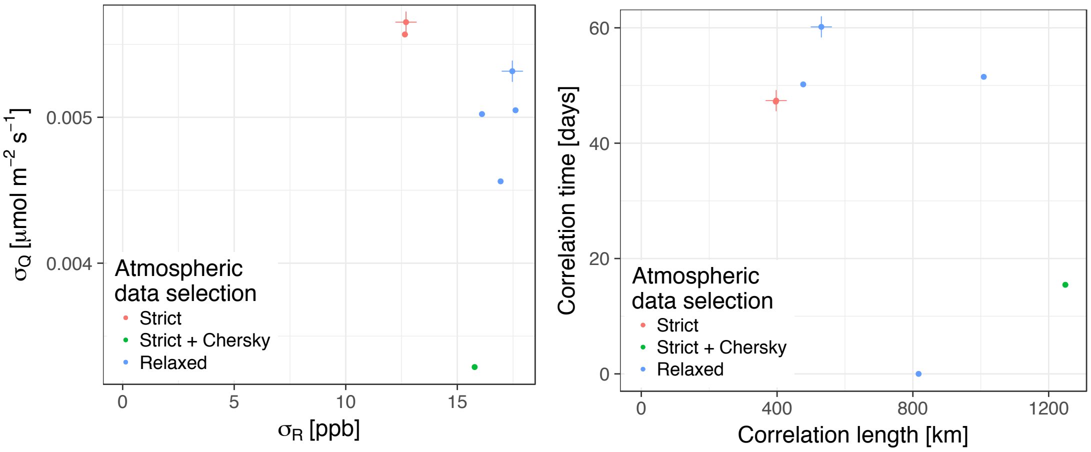

Fig. 11: Covariance parameters based on different regression models and atmospheric data selections. The crosses mark the parameters used for further analysis (values in Table 10). Left: Model-data mismatch and prior uncertainty. Right: Correlation length and time.

Table 10: Covariance parameter estimates used for further analyses.

Atmospheric data selection	Model-data mismatch (σ_R)	Prior uncertainty (σ_Q)	Correlation length	Correlation time
Strict	12.7 ppb	5.65 ×10^{-3} µmol m^{-2}s^{-1}	397 km	47.4 days
Relaxed	17.5 ppb	5.31 ×10^{-3} µmol m^{-2}s^{-1}	530 km	60.2 days

5.2.3 Regression models

In this section, we evaluate regression models and individual auxiliary variables for the purpose of selecting suitable models for inversions. Furthermore, we present insights on processes that can be deduced based on the large variety of considered regression models.

For model selection, the large number of auxiliary variables n (cf. Sect. 5.1.7) required the number of variables k in each regression model to be restricted, since the number of possible combinations ($n!/(k!\,(n-k)!)$) quickly became computationally intractable. After reducing the number of variables that describe terrestrial emissions (Sect. 5.2.3.2), $n = 33$

variables remained. We considered $k = 1, \dots, 7$ variables per model, which resulted in 5,663,889 regression models per parameter set.

In Sect. 5.2.3.1, evaluation criteria for regression models are introduced. Based on these methods, we first selected the best auxiliary variables for terrestrial emissions, which allowed more variables describing oceanic emissions to be considered in subsequent model selection runs (Sect. 5.2.3.2). In Sect. 5.2.3.3, we describe the range of annual CH_4 emissions that regression models attributed to the ESAS. In Sect. 5.2.3.4, we present insights on processes based on comparisons of individual auxiliary variables. In Sect. 5.2.3.5 we describe how atmospheric CH_4 data were modeled by the regression models.

5.2.3.1 Criteria for regression model evaluation

Based on the set of auxiliary variables (Table 8), regression models and their BIC scores were computed as described in Sect. 3.2.3.2. Models where any regression model coefficient $\boldsymbol{\beta}$ was negative were excluded from further analysis, since negative CH_4 emissions are unrealistic (CH_4 sinks were accounted for in the transport model, see Sect. 3.1.2). From these models, we selected models with a BIC score difference of less than 10 compared to the best BIC score. These models are subsequently referred to as "well-scoring" models. This threshold included models that clearly performed worse in terms of BIC than others: following Eq. (16), the probability that one model describes the data better than another model given a BIC score difference of 10 is $1{:}10^{-4}$. However, in our opinion, BIC score differences had less explanatory power than is suggested by Eq. (16) because of the large RMSE of modeled atmospheric CH_4 mole fractions compared with the data. We illustrate this assessment with an example. In the case that two models consist of the same number of auxiliary variables, the BIC score evaluates absolute differences in the residual sum of squares (RSS), and not relative differences: models with RSS of 10 and 20, respectively, have the same BIC score difference as models with RSS of 1010 and 1020, respectively, although the relative performance difference of the former would be considered much more significant than that of the latter. We decided to evaluate models with a relatively large threshold of $\Delta BIC<10$, because this selected between 113 and 182 well-scoring models for each parameter set, a number that allowed ranking individual auxiliary variables. In some cases, we present conclusions based on a stricter criterion. For the stricter criterion, we selected those of the well-scoring models that were among the 30 best models in terms of BIC score, as well as RMSE, correlation and mean bias between modeled and observed atmospheric data. This criterion selected between 3 and 8 models per parameter set, which we henceforth call the "best-scoring" models. The vast majority of both the well-scoring and the best-scoring models contained fewer than the maximum considered seven auxiliary variables. This suggests that, although considering regression models with more auxiliary variables could improve the fit to the atmospheric data, considering more complex models would not change the results based on BIC.

Variance inflation factors were generally less than 4 in well-scoring regression models and thus indicated no collinearity. This was expected since BIC selects against redundancy. Hence, collinearity is not discussed further in the evaluation of regression models.

5.2.3.2 Preparatory step: auxiliary variables for terrestrial CH_4 emissions

In order to reduce the number of auxiliary variables in the model selection for oceanic variables, the best auxiliary variables for terrestrial CH_4 emissions were determined in a preparatory step. For this purpose, model selection was run on the full set of variables that describe terrestrial emissions, with only few variables that describe ocean emissions. This split was possible because most of the important ocean variables from the full set were in the set of variables used here (cf. below). This was done for four parameter sets: strict and relaxed atmospheric data selection, and 5- and 15-day backtrajectories, in all cases with strict boundary condition optimization.

The largest contributions to the terrestrial CH_4 budget were from the Simple Wetland Model (SWM) and the constant land flux, either or both of which were chosen for each well-scoring model. WSL was part of the vast majority of well-scoring regression models, and thus far outperformed all other process-based wetland models. Its contribution to the budget was small compared to the contributions from Simple Wetland Model and constant land flux. The majority of the well-scoring models also contained the Zero Curtain Model (ZCM). In some cases with relaxed data selection, the lake emission model (bLake4Me) was selected as well.

Based on these observations, we computed and analyzed regression models with the full set of ESAS-related variables with only the Simple Wetland Model, the constant land flux, WSL, the Zero Curtain Model and bLake4me to describe terrestrial CH_4 emissions. Other auxiliary variables for terrestrial emissions – i.e. all process-based wetland models besides WSL – were excluded from further analyses.

5.2.3.3 Annual ESAS CH_4 budget of regression models

We evaluated the range of annual ESAS CH_4 budget estimates supported by the atmospheric data by computing them for the well-scoring regression models. For this purpose, the budgets of all auxiliary variables that described ESAS emissions were added for the period Oct 2014 – Sep 2015. Here, we report ranges and averages of the annual ESAS regression model budget depending on parameter set. Contributions of individual variables to the ESAS regression model budget are shown in Sect. 5.2.3.4.

Varying with selected variables, the ESAS regression model budget ranged between 0 and 1.4 Tg CH_4 yr^{-1} (Fig. 12). The largest ESAS budgets were obtained with relaxed atmospheric data selection, strict boundary condition optimization, and 5-day backtrajectories (parameter set “ds:R-bc:S-bl:5”); other parameter sets returned maximum budgets of 1.3 Tg. The average ESAS budgets among the well-scoring models were 0.7–0.9 Tg CH_4 yr^{-1}

depending on the parameter set, with runs with 15-day backtrajectories and relaxed data selection yielding the slightly smaller budgets. When further selecting for best-scoring models, the range of the ESAS budget estimate across all parameter sets was narrowed down to 0.6–1.2 Tg CH_4 yr^{-1} for strict data selection, and 0–1.2 Tg CH_4 yr^{-1} for relaxed data selection with larger averages for strict atmospheric data selection (0.9 – 1.0 Tg) than relaxed data selection (0.6 – 0.7 Tg). The ESAS budget slightly correlated negatively with the budget attributed to terrestrial emissions for each parameter set, but with large variances (illustrated by the large scatter in Fig. 12). Terrestrial emission budgets ranged from 2.5 to 5.3 Tg CH_4 yr^{-1} (average: 3.7–4.6 Tg CH_4 yr^{-1}) and thus were assigned the majority of the emissions in the domain.

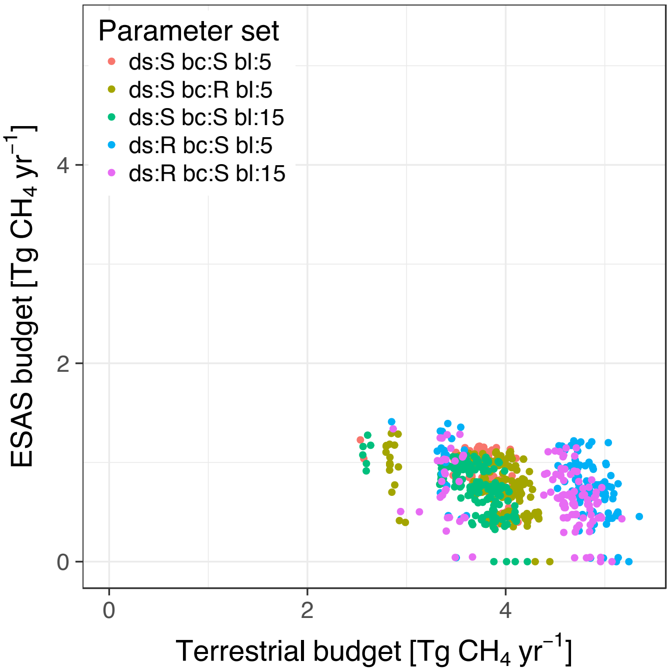

Fig. 12: Annual CH_4 budgets assigned by well-scoring regression models to ESAS and land regions (Oct 2014 – Sep 2015).

5.2.3.4 Process insights based on regression models

We compared the performance of individual auxiliary variables or set thereof by two different metrics. The first metric was the fraction of regression models (well- or best-scoring) that contained the variable (or either of the variables in a set). Since this metric may be sensitive to the pool of considered regression models, a second metric for the comparisons was the rank of the first regression model that contained the variable (or either of a set of variables) in terms of their BIC score (normalized to the range 0–1). To further assess the relevance of certain auxiliary variables, we investigated annual budgets assigned to them.

We used this method to compare auxiliary variables that described shallow parts of the ESAS to those that described deeper parts of the ESAS, and to compare the performance of variables that were modulated by sea ice cover. Furthermore, we identified low-ranking variables.

Larger CH_4 emissions attributed to shallow than deep ESAS

Among the ESAS-related variables that selected for ocean depth, there was a clear preference of variables that attributed emissions to shallow waters over those that attributed emissions to deeper waters. This finding was consistent across the two different evaluation metrics introduced above and all parameter sets (Fig. 13). The maximum budget attributed to individual shallow-ocean variables was larger than for deep-ocean variables (Fig. 14). The variables modulated by sea ice cover were assigned budgets of up to 0.5 Tg CH_4 yr^{-1}, while those without modulation reached up to 1.2 Tg CH_4 yr^{-1}. Note that, in the above assessment, the sea ice growth variable, which attributed emissions throughout the shelf, was ignored because it primarily attributed emissions to fall. The results held when models that featured this variable were excluded (not shown).

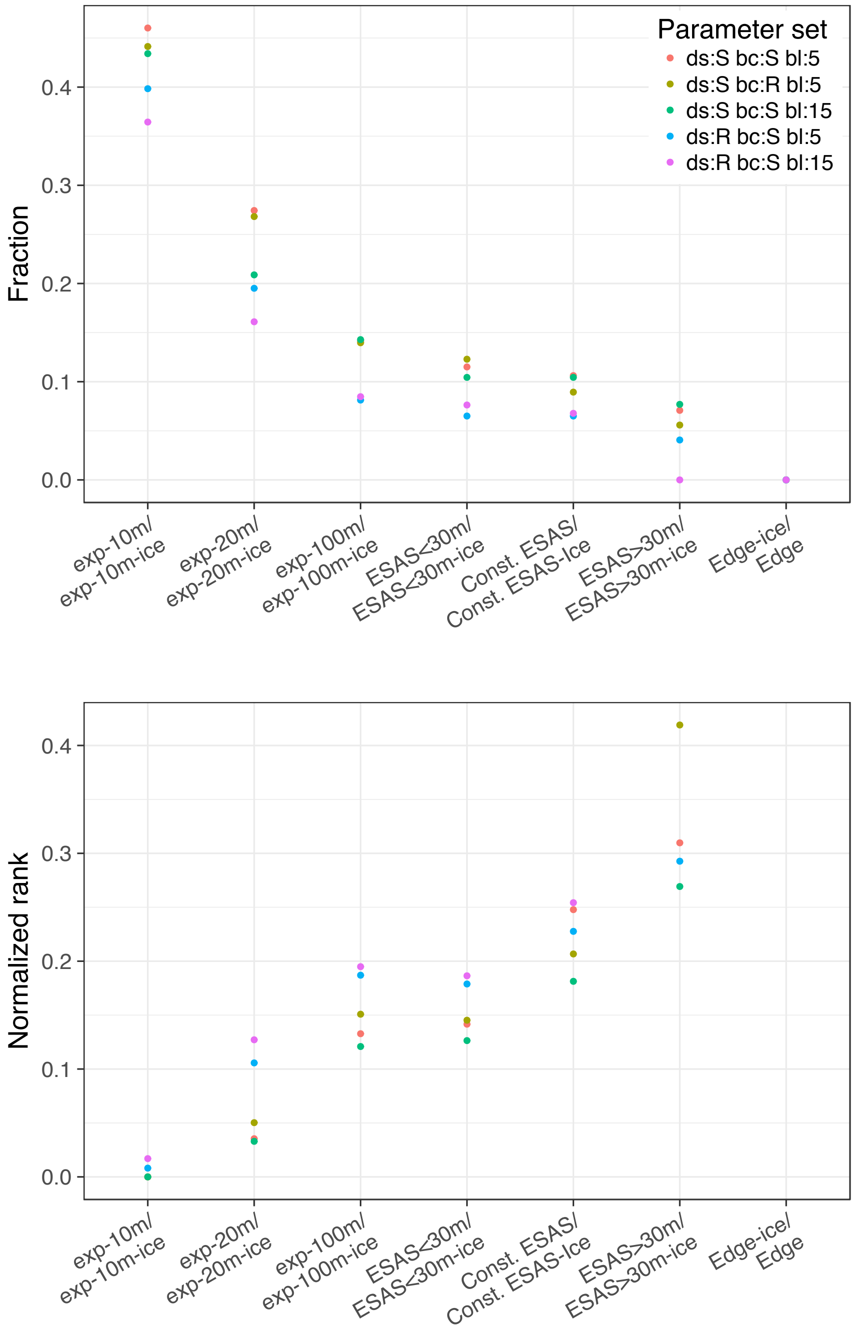

Fig. 13: Evaluation metrics as defined in Sect. 5.2.3.1 for auxiliary variables that assign ESAS emissions depending on ocean depth. Each data point corresponds to two auxiliary variables with the same depth distribution, one constant in time and the other modulated by sea ice. The sea ice growth variable was ignored in this test because it primarily attributed emissions to fall. Other ESAS-related variables were ignored because they were much less frequently selected and did not impact the result. The abscissae are sorted by the average performance of each depth distribution (same result in both metrics). Top: Fraction of well-scoring regression models that contained at least one of the two variables with a specific depth distribution. Bottom: BIC-rank of the first model that contained at least one of these variables (normalized to the range 0–1).

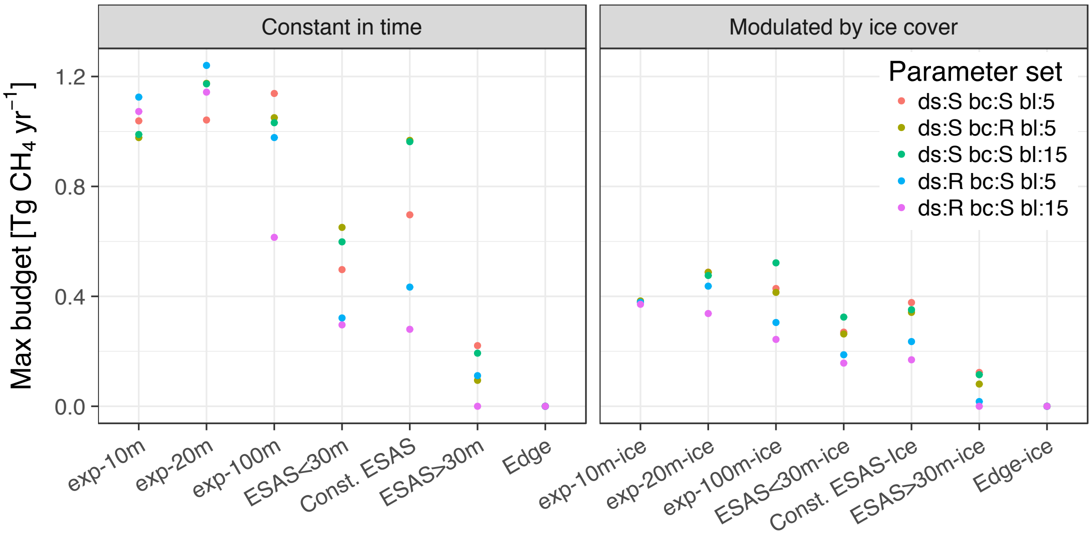

Fig. 14: Maximum annual CH_4 budget attributed to auxiliary variables that vary with ocean depth (sorted as in Fig. 13). Left panel: variables without seasonal variation. Right panel: the same variables modulated by sea ice cover.

Sea ice cover as a barrier for CH_4 emissions

Among the well-scoring models, variables that were modulated by sea ice cover ranked slightly lower than those without the modulation, but with larger differences between parameter sets than between the two groups (Fig. 15). Among the best-scoring models, the variables without modulation by sea ice cover were preferred as well.

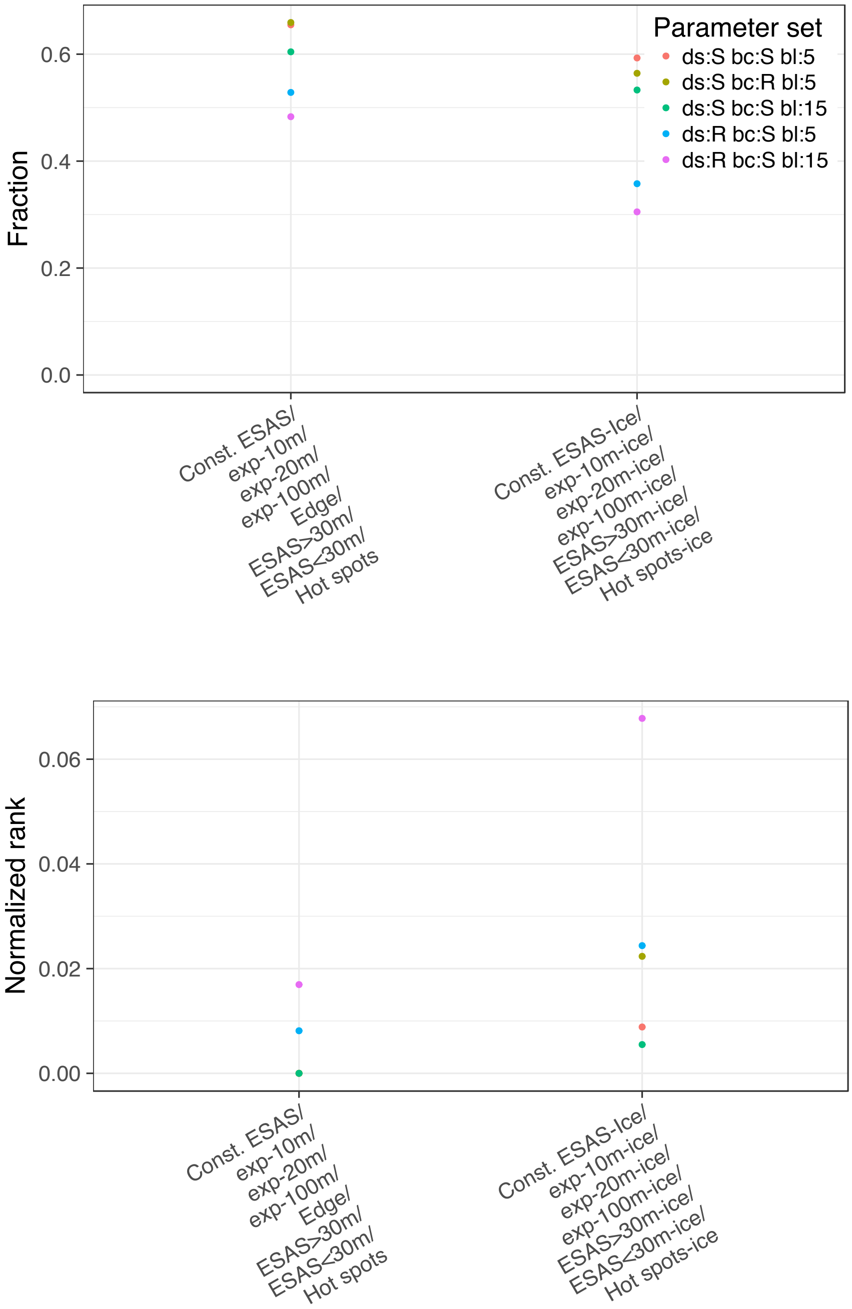

Fig. 15: Evaluation of auxiliary variables for ESAS CH_4 emissions that are constant in time (left) or modulated by sea ice cover (right). The metrics are the same as in Fig. 13 and were introduced in Sect. 5.2.3.1.

Sea ice growth

The sea ice growth variable was contained in 70–83 % of well-scoring models, and 60–80 % of best-scoring models for the individual parameter sets, making it the single highest scoring auxiliary variable describing ESAS CH_4 emissions. Emissions attributed to this variable were substantial in comparison to the variables that describe ESAS CH_4 emissions throughout the year, ranging 0.3–0.5 Tg CH_4 yr^{-1} (average 0.4 Tg CH_4 yr^{-1}) across the well-scoring regression models for the different parameter sets.

Sea ice retreat

The variable describing sea ice retreat was rarely selected and ranked low among the well-scoring models. The annual budget attributed to the pattern was less than 0.1 Tg CH_4 yr^{-1} in all cases.

Hot spot pattern

The hotspot map extracted from Shakhova et al. (2010a) ranked low among the well-scoring models, both with and without modulation by sea ice cover. In the cases it was included in the regression model, the annual budget attributed to this pattern was below 0.1 Tg CH_4 yr^{-1}.

Wind speed

All variables linked to wind speed – i.e. gas transfer velocity and storms – were rarely selected and ranked low among the well-scoring models.

Kolyma river mouth

The Kolyma river mouth variable ranked high among the well-scoring models in the cases with relaxed atmospheric data selection, and low in the cases with strict atmospheric data selection. In either case, the budget attributed to the variable was less than 0.05 Tg CH_4 yr^{-1}. Regression models that contained the variable attributed smaller annual budgets to the ESAS. While lower budget estimates were not affected, budget estimates on the high end (above 1.2 Tg CH_4 yr^{-1}) were on average reduced by 0.11 Tg and 0.24 Tg with strict and relaxed data selection, respectively.

Terrestrial CH_4 emissions

Results of variables that described terrestrial CH_4 emissions were similar as in the preparatory step that included far fewer oceanic variables (Sect. 5.2.3.2). The vast majority of well-scoring regression models contained several auxiliary variables related to terrestrial emissions. In particular, most well-scoring models contained either the Simple Wetland Model or the constant land emissions, or both. The latter cases yielded the higher terrestrial budgets in Fig. 12. Most of the best-scoring models contained both of these variables, with the exception of the parameter set "ds:S bc:S bl:5", where the Simple Wetland Model was only selected in two out of the eight best-scoring models. Furthermore, WSL was selected in most well-scoring models. The Zero Curtain Model was selected in all best-scoring models, while the lake model (bLake4Me) ranked low in these model selection runs.

5.2.3.5 Atmospheric data modeled by regression models

Summary statistics

Atmospheric observations modeled by the regression models yielded moderate agreement with observations. Here, we present statistics on the mismatches between modeled and observed atmospheric data, focusing on averages of well-scoring regression models per parameter set. Results are displayed in Table 11 and summarized in the following paragraphs. Qualitatively, most results agreed across all parameter sets, and also held for both the well-scoring and best-scoring regression models. The quantitative results depended on atmospheric data selection, but much less on boundary conditions and trajectory length.

Modeled atmospheric mole fractions correlated better with data from Tiksi than Ambarchik and Barrow. With the relaxed model selection, the correlations of the latter two improved over the strict model selection, while that of Tiksi was similar. On the other hand, root mean squared errors were larger with relaxed data selection, indicating larger variability of the data that was harder to capture for the auxiliary variables. RMSE for Ambarchik was clearly higher than at Tiksi and Barrow. The regression models underestimated Ambarchik data on average, while they overestimated Tiksi data and Barrow was in between. This indicates differences in the spatial distribution of emissions across the domain or in the vicinity of the stations that were not captured by the auxiliary variables.

Table 11: Summary statistics of the mismatch between observed and modeled atmospheric CH_4 mole fractions. Shown here are averages and standard deviation of the well-scoring regression models for the model selection runs with trajectory length of 5 days and strict boundary condition optimization.

	Correlation coefficient		RMSE [ppb]		Mean bias [ppb]	
	Strict	Relaxed	Strict	Relaxed	Strict	Relaxed
Ambarchik	0.40±0.05	0.48±0.03	32.3±0.9	39.1±0.9	-3.3±2.2	-4.3±3.7
Barrow	0.41±0.04	0.49±0.06	15.9±0.5	21.8±0.6	1.9±0.5	-1.1±1.0
Tiksi	0.59±0.05	0.61±0.03	21.2±0.6	23.0±0.5	6.6±0.9	8.1±2.3
All data	0.55±0.02	0.56±0.02	23.0±0.3	27.7±0.4	2.3±0.9	1.4±1.8

Seasonality of biases

Seasonal biases of modeled atmospheric mole fractions are summarized in Table 12. The largest seasonal offsets were observed at Ambarchik, followed by Tiksi. Ambarchik observations were clearly underestimated by the models in fall and winter. The opposite applied to Tiksi, while the results for Barrow were mixed. By contrast, observations in spring and summer were overestimated at Ambarchik and Tiksi (neutral at Barrow). These overestimations may be linked to the large underestimation of cold season signals at Ambarchik.

Table 12: Seasonal biases of the well-scoring regression models averaged over all parameter sets. The errors are one standard deviation. All values are in ppb.

	Winter (DJF)	Spring (MAMJ)	Summer (JA)	Fall (SON)
Ambarchik	-7.1±2.4	9.7±1.0	5.2±2.3	-16.0±0.9
Barrow	4.4±0.8	1.4±0.8	0.5±1.0	-2.5±3.1
Tiksi	12.0±3.2	7.2±2.1	3.9±3.6	7.3±1.6

Relative impact of terrestrial and oceanic auxiliary variables on modeled atmospheric CH_4 signals

On average, contributions from variables describing oceanic emissions to modeled atmospheric signals were smaller than those describing terrestrial emissions in the well-scoring models (Fig. 16). In a few cases, the largest average oceanic contributions were on par with those of terrestrial emissions (Fig. 16).

We investigated the relative impact of oceanic and terrestrial emissions on the seasonality of modeled atmospheric data. For this purpose, we computed average regression model biases for two subsets of the well-scoring regression models that excluded seasonally varying oceanic and terrestrial variables, respectively. The seasonality of the biases depended mostly on the variables that described terrestrial emissions (not shown).

Thus, terrestrial emissions contributed more strongly to modeled atmospheric signals than oceanic emissions.

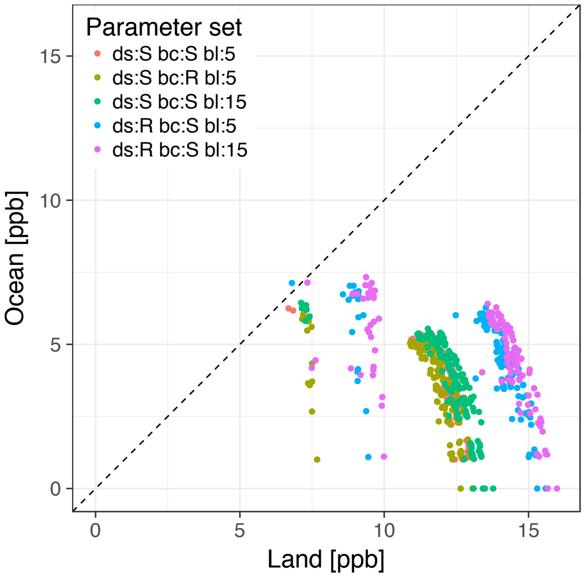

Fig. 16: Average contribution of terrestrial and oceanic emissions to modeled atmospheric CH_4 signals in all well-scoring regression models.

Atmospheric signals modeled by regression models: Impact of individual auxiliary variables and ambiguous attribution

In the following paragraphs, we present how individual auxiliary variables contributed to modeled observed atmospheric signals at the three sites used for optimization in different regression models.

Fig. 17 shows atmospheric CH_4 mole fractions at Tiksi for two regression models. The model in the left panel featured the constant land flux; the model to the right did not. As a consequence, the model on the left modeled higher CH_4 signals in winter and spring, filling some gaps and overestimating other signals. This demonstrates the influence of the terrestrial variables on seasonality of model bias that was briefly described above. The plots also demonstrate how individual spikes can be attributed to either land or ocean emissions. I.e. in spring, a number of signals were attributed partially to the constant land flux and the ESAS variable (left panel).

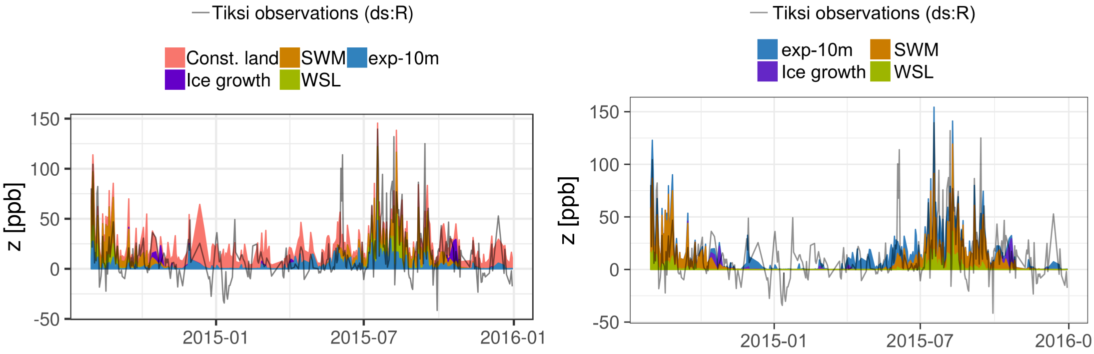

Fig. 17: Atmospheric CH_4 mole fractions at Tiksi modeled by two different regression models. Both panels show results obtained with relaxed atmospheric data selection.

Fig. 18 shows modeled CH_4 mole fractions at Ambarchik. All examples expose the inability of the regression models to model fall and winter signals at the station, revealing the seasonal biases presented above. The sea ice growth variable contributed a part of this missing signal, which may be why the variable ranked high in the model selection.

The model in the top right panel of Fig. 18 featured the variable for coastal ESAS emissions (exp-10m) with a budget of 0.8 Tg CH_4 yr^{-1}, the one on the top left featured the Kolyma mouth with variable with a budget of 0.04 Tg CH_4 yr^{-1} instead. Despite the vast budget difference, the variables contributed similarly to the modeled atmospheric signal, on average 4.7 ppb and 2.6 ppb, respectively. This demonstrates that emissions in the near field of an observation station can have a large impact on modeled atmospheric data and emissions.

Like Fig. 17, Fig. 18 also demonstrates how certain signals can be attributed to different processes by the regression model. Signals in winter were attributed to both the constant land flux and, where included, the shallow ocean or Kolyma-mouth variable.

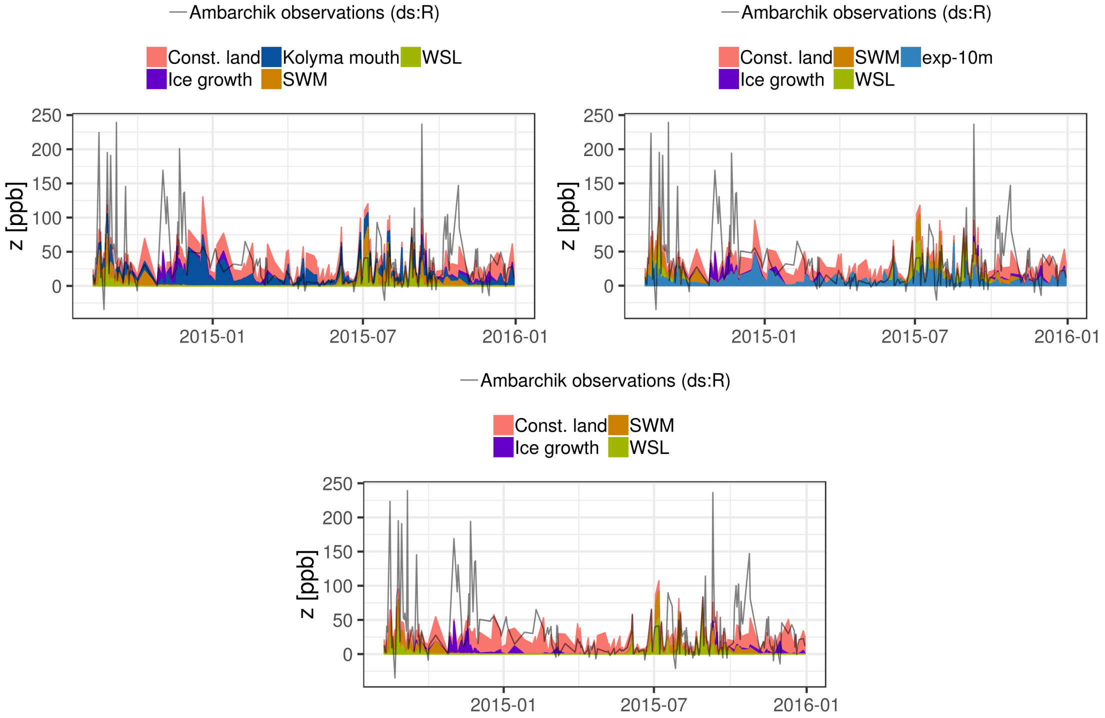

Fig. 18: Atmospheric CH₄ mole fractions at Ambarchik modeled by three different regression models. All panels show results with relaxed data selection. The difference between the regression models is the ESAS variable with year-round emissions. Top left: Kolyma mouth. Top right: shallow ocean (exp-10m). Bottom: No ESAS variable.

Fig. 19 shows two examples of modeled atmospheric mole fractions at Barrow. Here, the difference between strict and relaxed data selection is illustrated, the latter including larger signals. The figure demonstrates that even a well-scoring auxiliary variable may not describe data at all stations in the domain well: here, the sea ice growth variable, which was part of most well-scoring and best-scoring models, produced atmospheric signals that were not observed, for example in December 2015 in both models.

A large number of signals observed at Barrow were modeled very well by the variable for constant land emissions.

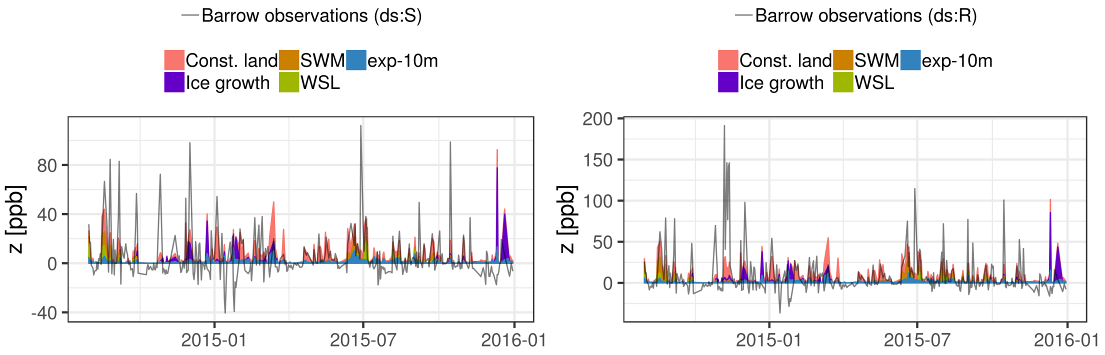

Fig. 19: Atmospheric CH_4 mole fractions at Barrow modeled by two different regression models. The panel on the left shows results with strict data selection, while the example on the right is for relaxed data selection.

The results of this section demonstrated why certain auxiliary variables were featured among the well-scoring models, and showcase that signal attribution to auxiliary variables can be ambiguous.

5.2.4 Inversions

5.2.4.1 Inversion scenarios

Based on the results of regression model selection, settings for an ensemble of inversions were chosen. In summary, the primary influential elements that need to be considered for further interpretation were the regression model, but smaller differences between the options for atmospheric data selection and backtrajectory length were considered as well. The boundary conditions had little influence on the results (see Sect. 5.3.1.3 for more details), and therefore, all inversions were performed with strict boundary condition optimization.

Due to the large number of model setups, in particular well-scoring regression models, we selected a small number of setups to perform inversions. The primary difference between these "inversion scenarios" was the regression model. We considered scenarios that either (a) were most compatible with the atmospheric data (best-scoring regression models), or (b) yielded lowest and highest ESAS budgets among the well-scoring models, or (c) featured less successful oceanic auxiliary variables that were nonetheless suitable for certain tests (e.g. constant ESAS emissions or variables modulated by sea ice cover). The different scenarios are summarized in Table 13 and explained in the following paragraphs.

(a) Best-scoring regression models

Coastal emissions and sea ice growth

The best-scoring regression models tended to feature the shallowest ocean variable, not modulated by sea ice cover (exp-10m) and the sea ice growth variable, both of which were therefore chosen for inversions. Since the Kolyma mouth variable ranked among the well-scoring regression models with relaxed data selection, it was included in an additional inversion. Terrestrial variables in the best-scoring models were the constant land flux, the Simple Wetland Model, the Zero Curtain Model, and WSL.

(b) Boundaries of ESAS budget

Low ESAS budget scenarios

The prior ESAS budget was lowest in regression models without an ESAS-related variable or only the Kolyma mouth- variable, of which there were some among the well-scoring models (cf. Fig. 12). When 5-day backtrajectories were used, regression models without ESAS-related variables were not selected in the case of strict atmospheric data selection (cf. Fig. 12), and ESAS budgets with 15-day backtrajectories were on average slightly lower; therefore, 15-day backtrajectories were used in the Low ESAS emissions scenarios. Furthermore, a regression model with a high terrestrial budget was used (i.e., both the Simple Wetland Model and the constant land flux were included), since low terrestrial budgets yielded slightly higher ESAS budgets. The Kolyma mouth variable was included in one Low ESAS budget scenario to assess the impact the variable has on the lower bound of ESAS budget estimates.

High ESAS budget scenario

The highest ESAS budgets were obtained in models with relaxed atmospheric data selection (cf. Fig. 12). The regression models that yielded the highest ESAS budgets contained a shallow-ocean variable (cf. Fig. 14) without modulation with sea ice cover, and the sea ice growth variable. Backtrajectories of 5 days (instead of 15 days) and lower terrestrial budgets tended to yield more models with higher ESAS budgets and were therefore used in the High ESAS budget scenario. For this scenario, a small modification of the model with the highest budget among the well-scoring regression models was chosen. It originally featured the shallowest ocean variable (exp-10m), but since individually, exp-20m yielded slightly higher budgets than exp-10m, this variable was used instead. The idea behind this modification was to avoid underestimation of the upper bound of the budget.

(c) Tests with less successful ocean variables

No sea ice growth

The sea ice growth variable was highly successful in the regression model selection but strongly influences the seasonality of prior emissions. Inversions without this variable serve to investigate where this seasonality is retrieved if it is absent in the regression model. The regression models for these scenarios were the same as in the best-scoring models, but without sea ice growth.

No Simple Wetland Model

The Simple Wetland Model was selected in a lower fraction of well-scoring regression models for one parameter setting (ds:S bc:S bl:5) than the others. Therefore, this setting was chosen for an additional inversion.

Modulation with sea ice cover

Although the variables modulated by sea ice cover were slightly less successful than their unmodulated counterparts, inversion results with ESAS variables modulated by sea cover were performed to shed light on the detection of the seasonality of ESAS emissions. The best-scoring ESAS-related variable modulated by sea ice cover was the coastal emission variable exp-10m-ice. Therefore, inversions were performed with regression models as in the cases without sea ice growth (above), but replacing the non-varying ESAS variable exp-10m with its sea-ice-modulated version exp-10m-ice.

Constant and deep ESAS emissions

Inversions were performed with a constant ESAS prior, and with a prior that assigned ESAS emissions only to the deeper part of the shelf. Despite the low ranking of these variables in the model selection, these inversions serve to evaluate how prior emissions far from the coastal atmospheric observations are redistributed in the optimization.

Table 13: Model settings of the 15 performed inversions, sorted into the categories described in the text.

Scenario	Atmospheric data selection	Regression model	Backtrajectory length
Best-scoring regression models			
Coastal emissions + sea ice growth (strict)	Strict	Simple Wetland Model, constant land flux, WSL, Zero Curtain Model, exp-10m, sea ice growth	5 days
Coastal emissions +	Relaxed	Simple Wetland Model,	5 days

sea ice growth (relaxed)		constant land flux, WSL, Zero Curtain Model, exp-10m, sea ice growth	
Coastal emissions + sea ice growth + Kolyma mouth	Relaxed	Simple Wetland Model, constant land flux, WSL, Zero Curtain Model,, exp-10m, sea ice growth, Kolyma mouth	5 days
Extreme ESAS budgets			
High ESAS budget	Relaxed	Simple Wetland Model, WSL, exp-20m, sea ice growth	5 days
Low ESAS budget (strict)	Strict	Simple Wetland Model, constant land emissions, WSL, Zero Curtain Model	15 days
Low ESAS budget (relaxed)	Relaxed	Simple Wetland Model, Constant land emissions, WSL, Zero Curtain Model	15 days
Low ESAS budget + Kolyma mouth	Relaxed	Simple Wetland Model, constant land emissions, WSL, Zero Curtain Model, Kolyma mouth	15 days
No sea ice growth			
Coastal emissions (strict)	Strict	Simple Wetland Model, constant land flux, WSL, Zero Curtain Model, exp-10m	5 days
Coastal emissions (relaxed)	Relaxed	Simple Wetland Model, WSL, Zero Curtain Model, exp-10m	5 days
No Simple Wetland Model			
Coastal emissions (strict, no SWM)	Strict	Constant land flux, WSL, Zero Curtain Model, exp-10m	5 days
Sea ice cover			
Coastal emissions, sea ice cover (strict)	Strict	Same as “Coastal emissions”, but exp-10m replaced by exp-10m-ice	5 days
Coastal emissions, sea ice cover (relaxed)	Relaxed	Same as “Coastal emissions”, but exp-10m	5 days

		replaced by exp-10m-ice	
Constant and deep ESAS			
Constant ESAS emissions (strict)	Strict	Same as “Coastal emissions”, but exp-10m replaced by const. ESAS	5 days
Constant ESAS emissions (relaxed)	Relaxed	Same as “Coastal emissions”, but exp-10m replaced by const. ESAS	5 days
Deep ESAS emissions	Relaxed	Simple Wetland Model, WSL, Zero Curtain Model, ESAS>30m	5 days

5.2.4.2 Annual budget of posterior ESAS emission estimates

Posterior ESAS budget estimates were higher than those of the regression models in the Low ESAS budget scenarios, and matched them in the High ESAS budget scenario (Fig. 20). The regression model budgets in the inversions were 0.1–1.4 Tg CH_4 yr^{-1}. Note that this deviates slightly from the range reported in Sect. 5.2.3.3 because it was computed with a different method. The budgets in Sect. 5.2.3.3 were calculated by summing the budgets of ESAS-related auxiliary variables. By contrast, here we summed the emissions from each grid cell multiplied by the fraction of the grid cell that falls into the ESAS. This method suffers from some “leakage” of terrestrial emissions into the ESAS budget at coastal grid cells, which is the reason why the regression model budgets computed for the Low ESAS budget scenarios were 0.1 Tg CH_4 yr^{-1}, despite featuring no ESAS-related auxiliary variable. Thus, posterior budgets and flux rates of the ESAS were slightly overestimated, especially at the low end. Since the impact of 0.1 Tg was insignificant for the conclusions of this work, and subtracting the terrestrial regression model contribution would result in some negative emissions, no correction for coastal grid cells was applied.

The range of budget estimates of posterior emissions was 0.4–1.5 Tg CH_4 yr^{-1}. The posterior budget estimate depended not only on the inversion settings, but also on the period for which it was calculated (see caption of Fig. 20). This hints at the influence that short events can have on the budget. More details on the flux variations over time are presented in Sect. 5.2.4.5.

One pair of inversions (apart from the Low ESAS budget scenarios) differed only in the inclusion of the Kolyma mouth variable in the regression model. In this example, regression model emissions of the ESAS were 0.17 Tg lower when the Kolyma mouth variable was included, and the difference between the posterior budget estimates was 0.13 Tg.

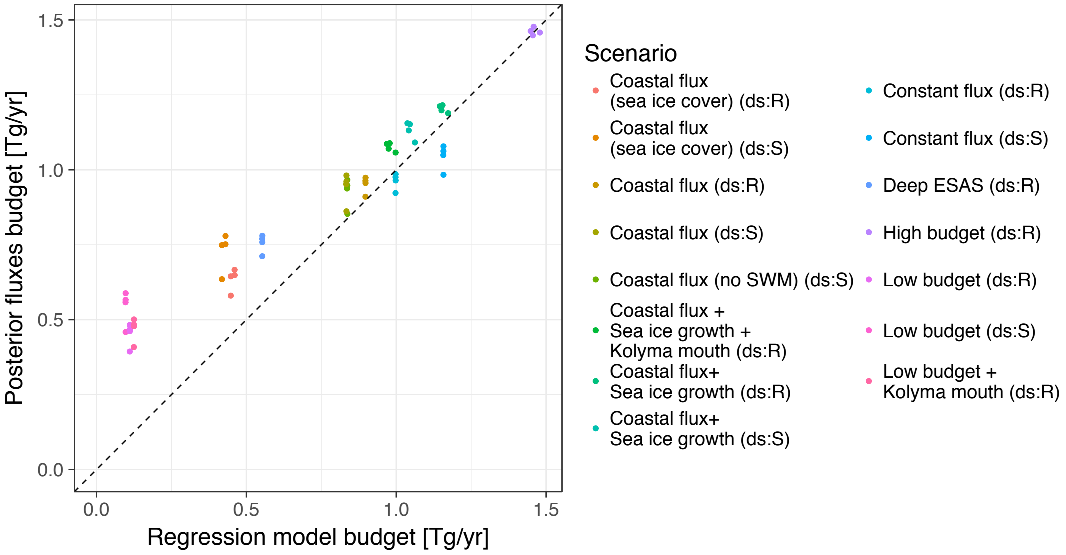

Fig. 20: ESAS CH_4 budgets estimated based on regression models and posterior fluxes of all performed inversions. For each inversion, budgets were calculated for four periods, i.e. 365 days starting Sep 1–Dec 1, 2014 in steps of one month, respectively.

5.2.4.3 ESAS CH_4 emission rates

We computed emission rates to facilitate comparison to other CH_4 sources at high northern latitudes for the interested reader. Average emission rates and annual budgets differed between the Laptev, East Siberian and Chukchi Sea (Fig. 21). In all cases, average Chukchi Sea emission rates were lower than East Siberian Sea emission rates. The emission rates from the Laptev Sea were mostly between those of the Chukchi and East Siberian Sea in the low budget scenarios, and higher than the emission rates from the East Siberian Sea in the inversions that yielded higher total budgets. The ranges of average annual flux rates across all inversions were 0.5–2.5 mg CH_4 m^{-2} d^{-1} (Laptev Sea), 0.6–2.1 mg CH_4 m^{-2} d^{-1} (East Siberian Sea) and 0.5–1.5 mg CH_4 m^{-2} d^{-1} (Chukchi Sea), with shelf-wide averages of 0.5–2.0 mg CH_4 m^{-2} d^{-1}.

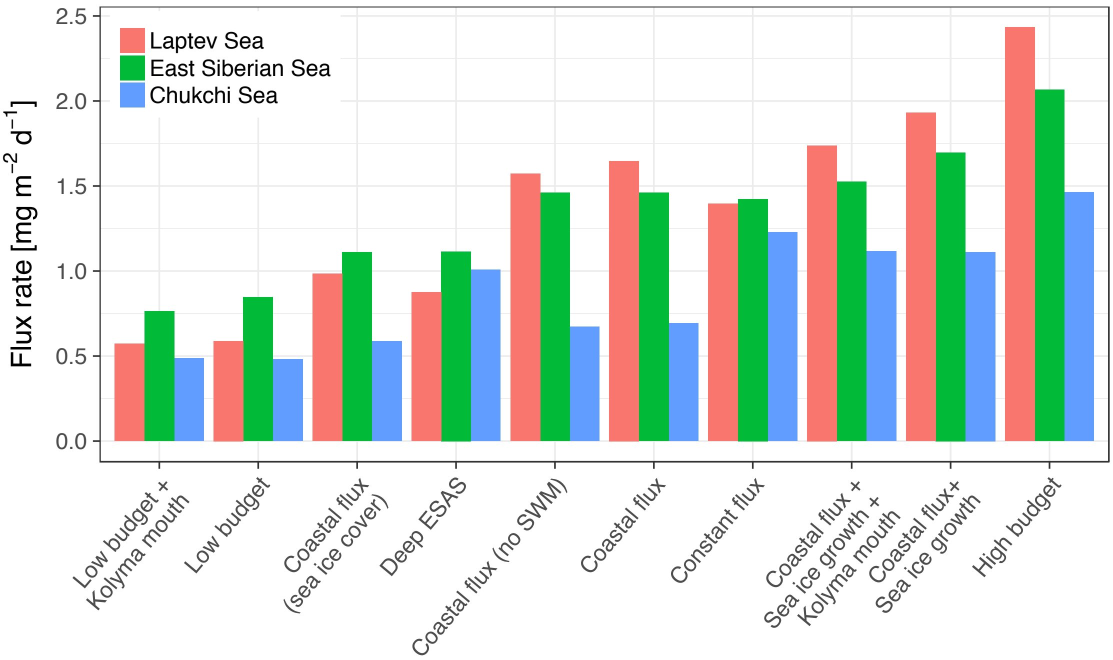

Fig. 21: Emission rates of posterior fluxes averaged over settings for atmospheric data selection and averaging period (see caption of Fig. 20). The values were ordered from low to high posterior ESAS budgets.

Since emissions were not uniformly distributed across the shelf seas (see Sect. 5.2.4.6), we also computed the range of ESAS emission rates at the scale of the grid resolution. Average annual emission rates of individual grid cells were up to 7.2 mg CH_4 m^{-2} d^{-1} (Laptev Sea), 8.1 mg CH_4 m^{-2} d^{-1} (East Siberian Sea) and 4.6 mg CH_4 m^{-2} d^{-1} (Chukchi Sea). Peak daily emission rates of individual grid cells were up to 31 mg CH_4 m^{-2} d^{-1} (Laptev Sea), 38 mg CH_4 m^{-2} d^{-1} (East Siberian Sea) and 30 mg CH_4 m^{-2} d^{-1} (Chukchi Sea). In almost all inversions, the maximum emission rates of the Laptev Sea were located in its southern part. In the East Siberian Sea, maximum emission rates were located either in the Kolyma mouth or at the coast south of the New Siberian Islands. The locations of the emission maxima in the Chukchi Sea, which were in almost all cases much lower than those in the Laptev and East Siberian Sea, scattered more between the inversions and were in some cases located further off the coast than in the other two regions.

5.2.4.4 Terrestrial emission budgets and rates

The budgets of terrestrial emissions were 3.2–4.7 Tg CH_4 yr^{-1} depending on the inversion scenario. By comparison, the budgets of the process-based wetland models considered for the regression models in this study were 0.4–2.0 Tg CH_4 yr^{-1} (WSL: 1.2 Tg), and the budget of the lake model bLake4Me was 2.1 Tg CH_4 yr^{-1}. Average flux rates were 4.6–6.8 mg CH_4 m^{-2} d^{-1}. Flux rates for individual pixels were up to 19 mg CH_4 m^{-2} d^{-1} averaged over one year, and up to 115 mg CH_4 m^{-2} d^{-1} on individual days. Thus, terrestrial emission estimates dominated over ESAS emission estimates.

5.2.4.5 Seasonal variation of ESAS emissions

Fig. 22 shows aggregated posterior and regression model emissions from the three ESAS seas. The largest variability and deviations of the posterior from the prior emissions were present in the East Siberian Sea. Here, the estimated emissions followed a distinct temporal pattern partly independently of the regression model: the highest emissions were assigned to fall 2014, and considerable emissions occurred well into the ice-covered period, exceeding the estimates of the regression models. The lowest emissions were assigned to April and May, where emissions from the regression models in which ESAS emissions were not modulated by sea ice cover were adjusted to lower values. Compared to fall 2014, emissions in fall 2015 followed the regression model more closely and were thus considerably lower if the sea ice growth variable was not included. The regression models that featured seasonally varying ESAS emissions reproduced aspects of this pattern in the East Siberian Sea: the High ESAS budget scenario featured the largest emissions in both fall periods and higher emissions in December than in summer, which was due to the sea ice growth auxiliary variable that was part of this model. The regression model in which coastal emissions were modulated with sea ice cover also resulted in comparatively large fall emissions; with both fall and winter emissions adjusted upwards in the posterior estimate compared to the regression models.

In both the Laptev and Chukchi Sea, the seasonal variations of the posterior emission estimates closely followed those of the regression model, with the exception of the Low ESAS budget scenarios. These results indicate that the seasonality of estimated emissions was mainly driven by the results for the East Siberian Sea, to which Ambarchik was most sensitive.

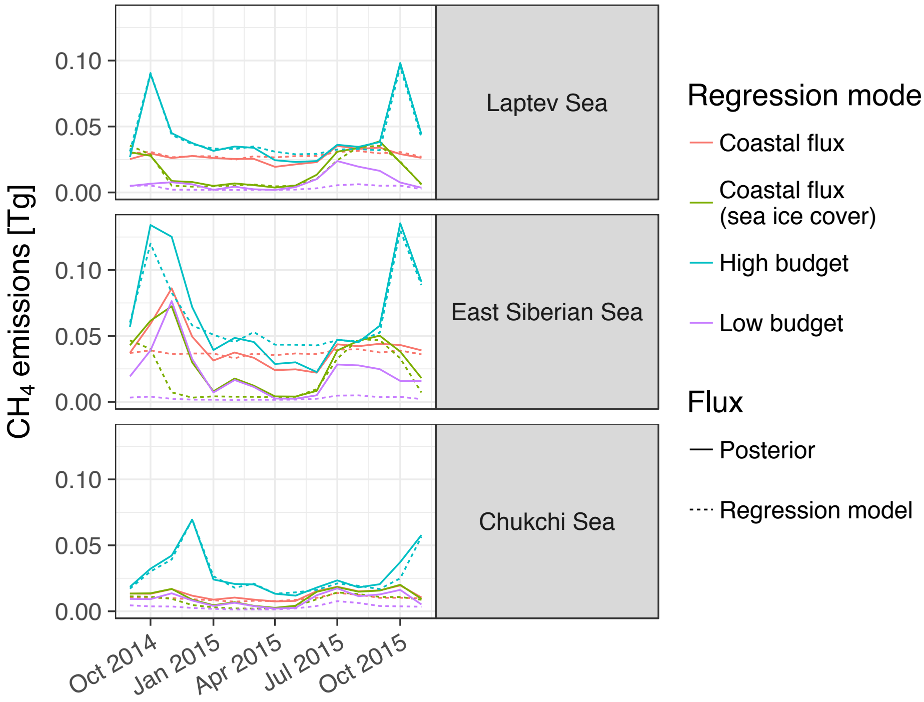

Fig. 22: Monthly CH4 emissions from the three parts of the ESAS between September 2014 and November 2015 for four inversions. The inversions were selected to represent the range of budget estimates and the influence of varying the regression model with sea ice cover.

Averaged over the ESAS, the emission rates during high ice cover (defined here as December until end of May) were 0.3–1.7 mg CH_4 m^{-2} d^{-1} depending on the scenario. During the period of lowest ice cover (August – September), emissions were 0.8–1.6 mg CH_4 m^{-2} d^{-1}. Thus, in scenarios that yielded high budgets, estimated emissions during the ice-covered period rivaled those of the period of lowest ice cover (Fig. 23, let panel).

Average emission during the period of the bulk of sea ice growth (October–November) were 0.9–3.8 mg CH_4 m^{-2} d^{-1} (Fig. 23, right panel) and thus far exceeded those of all other periods in many inversion scenarios. During sea ice retreat (June–July), emission rates were 0.7–1.4 mg CH_4 m^{-2} d^{-1}, slightly smaller than those of the period of lowest ice cover.

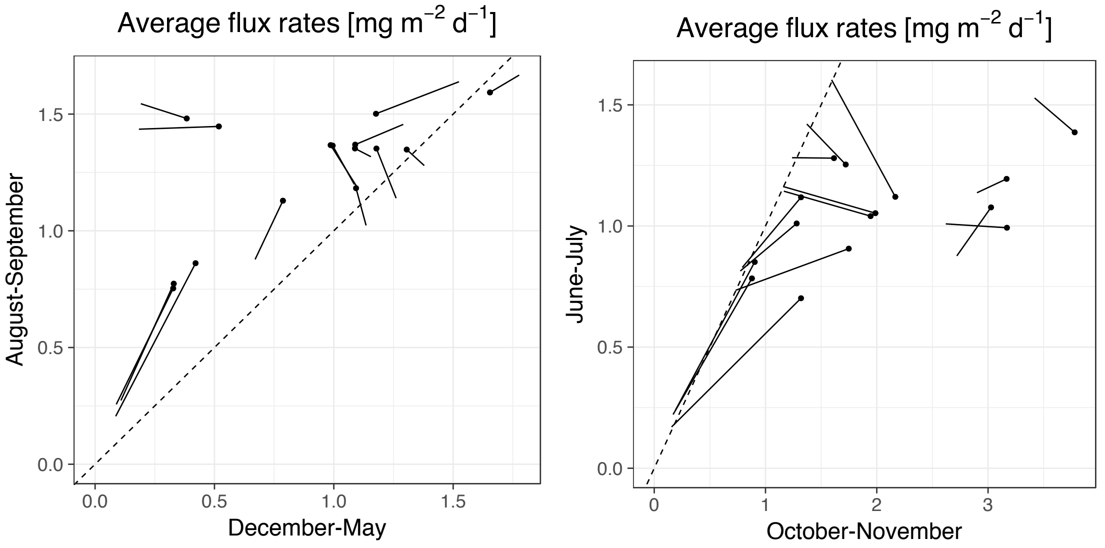

Fig. 23: Emission rates averaged over the ESAS for different states of sea ice cover. Posterior emission estimates are marked with a dot, and connected to regression model estimates via straight lines. Left: Low ice cover (August–September) vs. high ice cover (December–May). Right: Months of sea ice growth (October–November) and sea ice retreat (June–July).

5.2.4.6 Spatial patterns of posterior ESAS emissions and their deviation from the regression model

Deviations of posterior fluxes from the regression model (i.e. the stochastic flux component) reveal shortcomings of the latter. Here, we present spatial patterns of the cumulative annual stochastic flux component in the context of the posterior emissions.

The interpretation of the stochastic component of the non-negativity code has a caveat: in the optimization, the regression model is implicitly adjusted. Conceptually, the reason behind this is that non-negative fluxes do not follow a Gaussian probability distribution (i.e. their probability to be negative is 0), but regression model coefficients do. Thus, the stochastic component can be biased, which can cause boundaries between auxiliary variables (e.g. northern ESAS boundary in Fig. 25, left middle panel). Thus, we restricted the interpretation of the stochastic component to relative flux redistributions within the ESAS.

The stochastic component in the Low ESAS budget scenarios shows the minimum ESAS emissions that are required to explain the atmospheric data. In these scenarios, the inversions assign the largest ESAS emissions to southern parts of the Laptev and East Siberian Seas, forming hot spots close to the observation stations. No such hot spot was detected in the Chukchi Sea. There was a seasonal variation in the hot spot distribution: when including fall 2015 instead of fall 2014, there were two hot spots, close to Tiksi and Ambarchik, respectively. When including fall 2014 instead of fall 2015, other high-emission regions showed up at the coast between the former two and in the central part of the East

Siberian Sea (compare Fig. 24 with Fig. 25, top left panel). We continue analysis with the period Dec 2014 – Nov 2015, since observations were analogous for the period Sep 2014 – Aug 2015. A similar hot spot pattern as in the Low ESAS budget scenario was present in the scenario with constant ESAS emissions. Here, part of the constant prior flux was redistributed to the hot spots of the Low ESAS budget scenario (Fig. 25, middle panels). In the High ESAS budget scenario, the spatial pattern of the posterior emissions followed the auxiliary variable that described emissions from the shallow ocean. In this scenario, the hot spots from the Low ESAS budget scenario appeared to be part of a larger pattern of stronger emissions from the shallower parts of the ESAS (compare bottom and top right panels of Fig. 25).

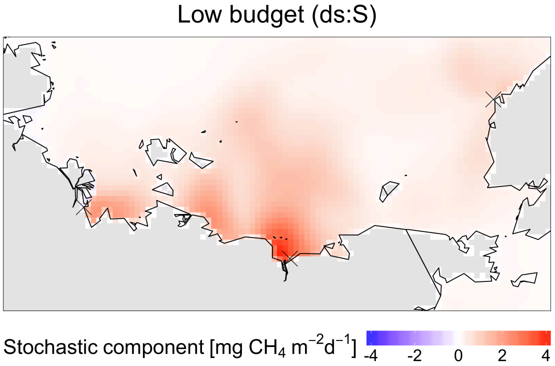

Fig. 24: Annual sum of the stochastic flux component of the Low ESAS budget scenario with strict atmospheric data selection for the period Sep 2014 – Aug 2015.

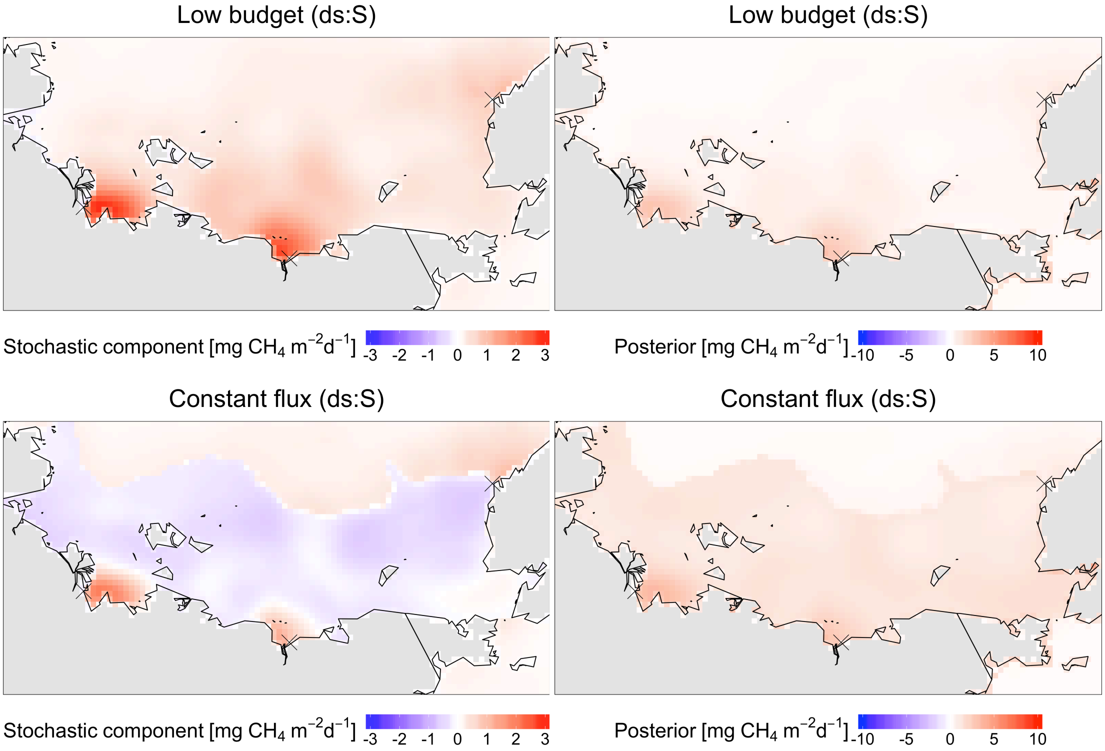

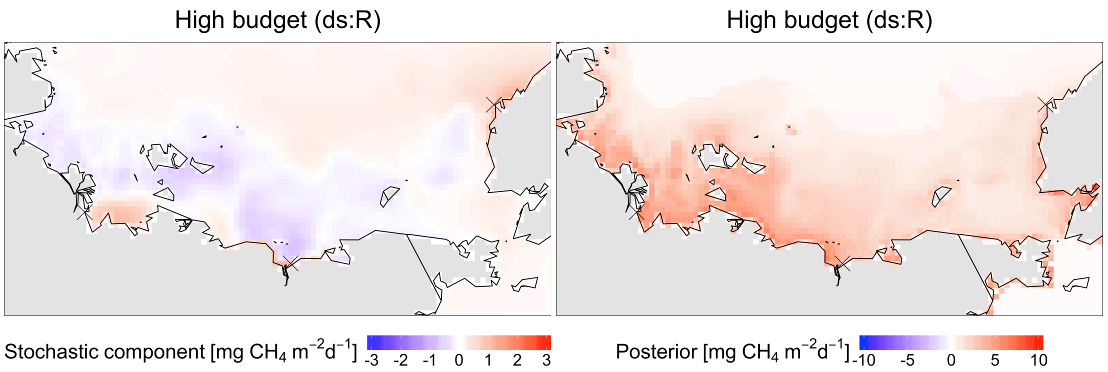

Fig. 25: Average stochastic flux component (left panels) and posterior emissions (right panels) of three inversions (Dec 2014 – Nov 2015). The titles refer to the inversion scenario. Terrestrial emissions were masked because including them would have hidden some of the patterns in the ESAS emissions. The panels on the left and on the right share one color scale, respectively.

5.2.4.7 Validation with independent data (SWERUS-C3 expedition)

Data from the SWERUS-C3 expedition were modeled using regression models and posterior emissions. The largest observed CH_4 excess over boundary conditions in this dataset, which was previously linked to high CH_4 concentrations in surface water (Thornton et al., 2016b), was reproduced by the Simple Wetland Model (Fig. 26). All ESAS-related auxiliary variables modeled signals that were not observed, including those that were modulated by sea ice cover (Fig. 26).

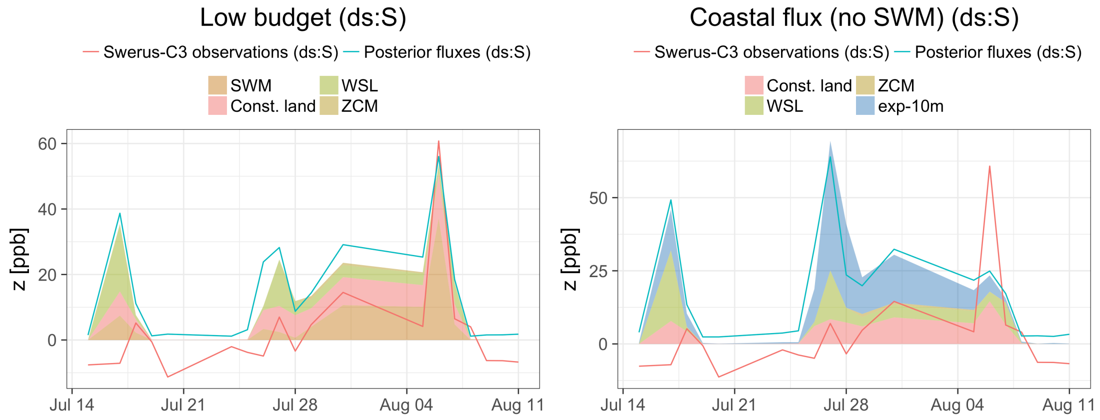

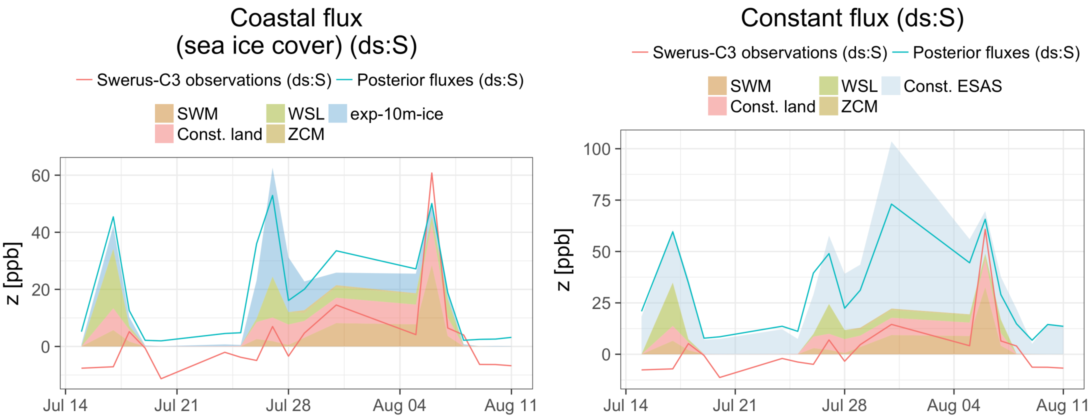

Fig. 26: Data from the SWERUS-C3 expedition modeled by regression models (stacked shaded areas) and posterior fluxes from selected inversions. SWERUS-C3 observations were filtered as in the strict data selection filter.

5.2.4.8 Ambiguous attribution of atmospheric signals to terrestrial vs. oceanic emissions

Footprints for many observations were sensitive to both terrestrial and oceanic emissions (not shown). Therefore, while some atmospheric signals were clearly attributed to either land or ocean emissions, others could be explained by either region. For example, individual CH_4 signals at Ambarchik in fall 2014, as well as persistently high mole fractions in December 2014, were explained both by oceanic and terrestrial emissions (Fig. 27, middle panel). By contrast, the fraction of signal explained by oceanic emissions was lower in early 2015 at this station, as well as in fall and winter 2015. This demonstrates that high fall and winter signals at Ambarchik, which were presumably the reason behind large posterior emissions from the East Siberian Sea in these periods (cf. Fig. 22), could also be attributed to terrestrial emissions.

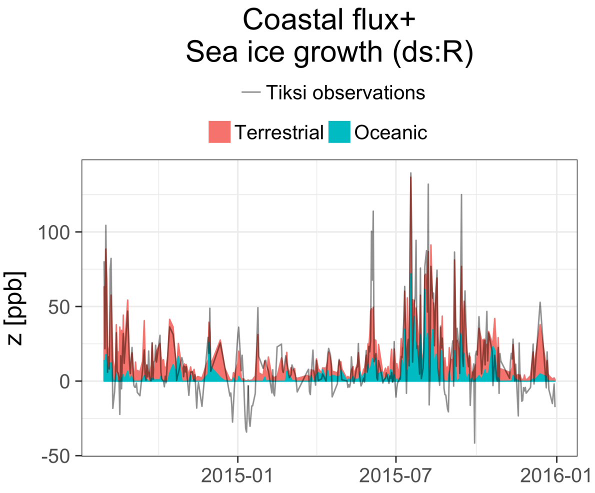

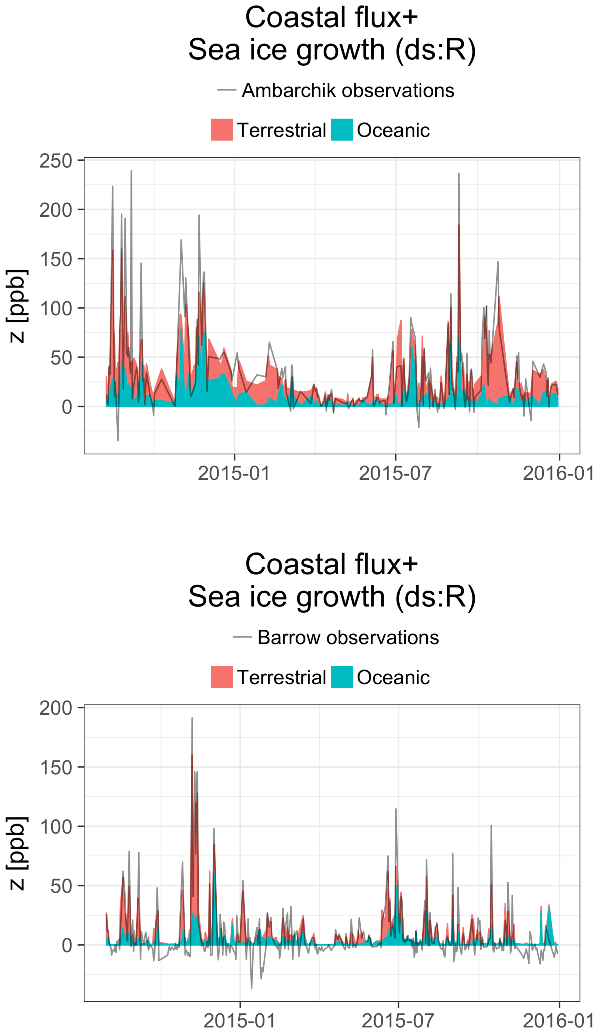

Fig. 27: Modeled atmospheric CH_4 mole fractions at Tiksi, Ambarchik and Barrow based on posterior emission estimates of the inversion scenario "Coastal flux + Sea ice growth" with relaxed atmospheric data selection.

5.2.5 Probing the robustness of key results with sensitivity studies

Key results of regression model selection and inversions were the low annual ESAS CH_4 budget in comparison to some literature estimates, the focus of the emissions on coastal areas, considerable emissions in fall associated with sea ice growth, and sustained emissions during the ice-covered season. We tested their robustness against several shortcomings of the model with additional simulations with modified data input. Motivation, implementation, and results of these sensitivity studies are presented in the following sections.

5.2.5.1 Bias correction for boundary conditions

Motivation

The boundary conditions overestimated some of the baseline observations at Tiksi (Fig. 17) and Barrow (Fig. 19), particularly in winter. Thus, boundary conditions may have had negative biases, in which case the cumulative CH_4 emissions inside the domain would have been underestimated. However, it is not certain that the negative CH_4 enhancements induced biases in the annual ESAS budget: since the boundary conditions at times explained large portions of the variability in the atmospheric data (Fig. 6), they may have been influenced by regional CH_4 sources that may have been difficult to model by the comparatively coarse global inverse model they were based on. Thus, on a seasonal timescale, the boundary conditions may be too smooth instead of biased, which would not indicate an overall bias. Furthermore, the impact of potential biases may be limited, since they occurred mainly when footprints were not influenced by ESAS emissions: at Barrow, negative signals occurred mostly when backtrajectories left the domain north of the station quickly after release. At Tiksi, they were mostly associated with backtrajectories that left quickly through the western domain boundary. Nonetheless, since a key result was that the estimated annual ESAS CH_4 budget was low compared to some estimates in the literature, the possibility of an underestimation due to biased boundary conditions was explored.

Implementation

The impact of negative CH_4 signals was quantified by performing regression model selection and inversions with atmospheric data modified with a simple bias correction. Since the seasonality of the biases at Tiksi and Barrow were similar, we assumed a seasonally varying bias that was consistent throughout the domain. It was estimated by fitting a baseline to all atmospheric data used in the optimization. The baseline consisted of a linear component and 10 harmonics (Thoning et al., 1989). It was constructed by fitting it to the lowest points in the atmospheric data by iteratively fitting it to the data and removing the data with the largest deviations from the fit until the result followed the vast majority of negative signals (Fig. 28). The baseline was between +1 and -35 ppb, with an average of -8.1 ppb. Model selection and inversions were run with one parameter setting: relaxed atmospheric data selection, strict boundary condition optimization and 5-day backtrajectories (label ds:R bc:S bl:5). A subset of inversion scenarios from the main set of inversions was chosen based on regression model selection similarly to the procedure in Sect. 5.2.4.1. They were a Low ESAS budget scenario, the High ESAS budget scenario, a scenario with coastal emissions and sea ice growth, and a constant ESAS flux scenario. For a comparison with data from the SWERUS-C3 campaign, a simple bias correction was implemented for this dataset as well, i.e. subtraction of a constant value.

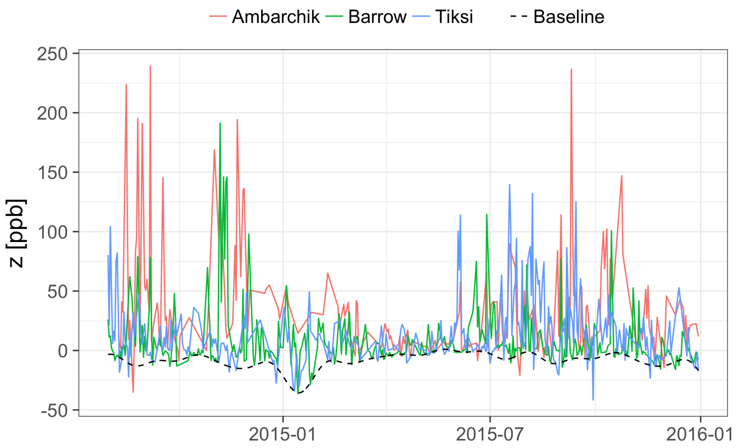

Fig. 28: Atmospheric data (relaxed data selection) after subtraction of boundary conditions, and the baseline subtracted from the data in the test of the impact of boundary condition biases.

Results

Key results on the spatiotemporal distribution of the emissions were robust with the modified data: emissions from shallow ESAS regions were preferred over those from deeper regions, variables modulated by sea ice performed slightly worse than those without the modulation, and the sea-ice-growth variable was among most well-scoring models with similar budgets assigned to it. The modification had an influence on the budgets of terrestrial regions and the ESAS: the range of the annual estimated ESAS budget was 0.6–1.8 Tg CH_4 yr^{-1}, compared to 0.4–1.5 Tg in the standard inversions, thus increasing the upper limit by 0.3 Tg. The budget of terrestrial regions increased to 3.7–6.0 Tg CH_4 yr^{-1}, compared to 3.4–4.7 Tg in the standard inversions. A comparison with data from the SWERUS-C3 campaign yielded similar results as without the bias correction.

5.2.5.2 Separation of signals of terrestrial and oceanic origin

Motivation

Atmospheric observations that were influenced by the ESAS were often also influenced by land areas, i.e. footprints rarely covered the ESAS exclusively (not shown). Since retrieved ESAS emissions were smaller than those retrieved for the land areas in the domain (Sect. 5.2.4.3 and Sect. 5.2.4.4), small errors in the terrestrial emissions may have caused large errors in the retrieved ESAS emissions. This could have caused the model to assign larger emissions to coastal areas of the ESAS than were actually present, und thus overestimate the ESAS CH_4 budget and explain the dominance of the shallow ocean in the regression models and posterior emissions. Furthermore, the cold season emission estimates may have been affected by cross-influence: the inversions assigned particularly large emissions to the East Siberian Sea in fall. This pattern was not consistently retrieved in the other ESAS regions, where the seasonality largely followed the respective regression models. This suggests that large fall emissions and their association with sea ice growth were primarily driven by data from Ambarchik. The vast majority of Ambarchik data during this period were obtained during southwesterly winds, and the signals from this direction were much larger than those obtained during northerly winds (Reum et al., 2018a). This suggests that signals assigned to the East Siberian Sea in fall might have originated from terrestrial emissions. An example for this situation is given in Fig. 29.

For these reasons, the robustness of the key results was tested against optimizing for a subset of the atmospheric data for which land and ocean areas were more clearly separated.

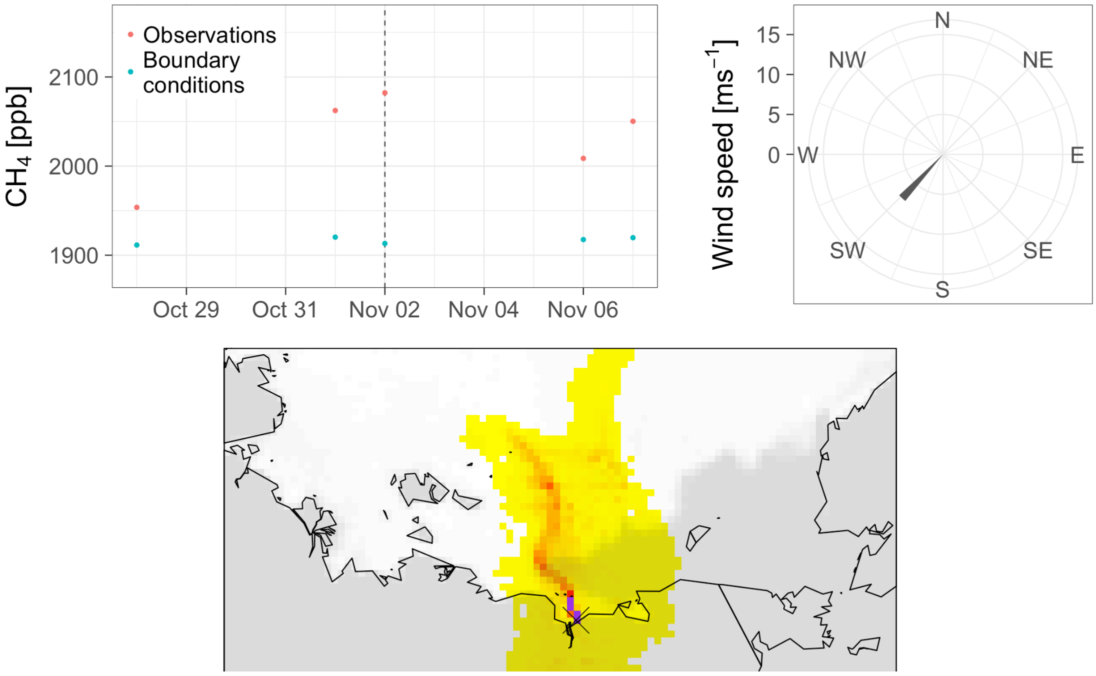

Fig. 29: Example of an atmospheric CH$_4$ signal potentially of terrestrial origin associated with an oceanic footprint. The large CH$_4$ enhancement over background conditions of almost 200 ppb (top left panel) was obtained during wind from southwest (measured on site; top right panel). By contrast, the modeled footprint (bottom panel) indicated influence from the ocean in the north.

Implementation

The atmospheric data (strict data selection) were selected for situations where 80% of the footprint covered either land or ocean regions, and where the locally measured wind direction matched the selection. Since footprints for data from both Tiksi and Barrow almost never covered the ESAS exclusively, the filter was applied only to Ambarchik. The valid wind direction window was 90° … 270° for land footprints, and 270° … 90° for ocean footprints. About one third of Ambarchik data matched these criteria. With these data, regression model selection was performed and a set of inversion scenarios developed. They represented a Low ESAS budget, High ESAS budget, coastal emissions, and an ice-cover scenario.

Results

In the regression model selection with the footprint filter, the annual posterior emissions aggregated over the shelf were 0.3–0.7 Tg CH_4 yr^{-1} depending on the regression model, compared to 0.4–1.4 Tg in the standard inversions. The dominance of auxiliary variables that attribute emissions to shallow parts of the ESAS over those that attribute emissions to deeper parts of the ESAS was similar as in the standard inversions. Regarding temporal emission variations, the relative contributions of fall and winter emissions were smaller than in the standard inversions (Fig. 30). First, by contrast to the standard inversions, the sea ice growth variable was rarely selected and ranked low among the well-scoring regression models. Consistent with this change, area-integrated emission rates in fall (0.4–1.1 mg CH_4 m^{-2} d^{-1}) were, on the high end, on par with those during the period of lowest ice cover (0.7–1.1 mg CH_4 m^{-2} d^{-1}), instead of far exceeding them as in the standard inversions. Second, emissions during the highest ice cover (December–May) were 0.2–0.8 mg CH_4 m^{-2} d^{-1}, and thus did not, as in the standard inversions, rival emissions during the period of lowest ice cover. Emissions during strongest sea ice growth (June and July) were slightly smaller (0.6–0.9 mg CH_4 m^{-2} d^{-1}) than during the period of lowest ice cover (August and September), as it was the case in the standard inversions. Unlike in the standard regression model selection, the best-scoring regression models featured more ESAS variables modulated by sea ice cover than not. The hot spot map by Shakhova et al. (2010a), modulated by sea ice cover, was selected in 8% of well-scoring regression models, compared to 4 % in the corresponding standard inversion with the same setup (ds:S bc:S bl:5). The map was attributed a maximum of 0.17 Tg CH_4 yr^{-1}. Posterior terrestrial emissions in this setup were also lower than in the standard inversions (2.3–3.5 Tg compared to 3.4–4.7 Tg). Unlike in the standard inversions, the large spike in the SWERUS-C3 data was not reproduced (possibly because the Simple Wetland Model was not included in the inversion scenarios, since it ranked low in the regression model selection) while, similarly to the standard inversions, ESAS-related variables still modeled signals that were not observed.

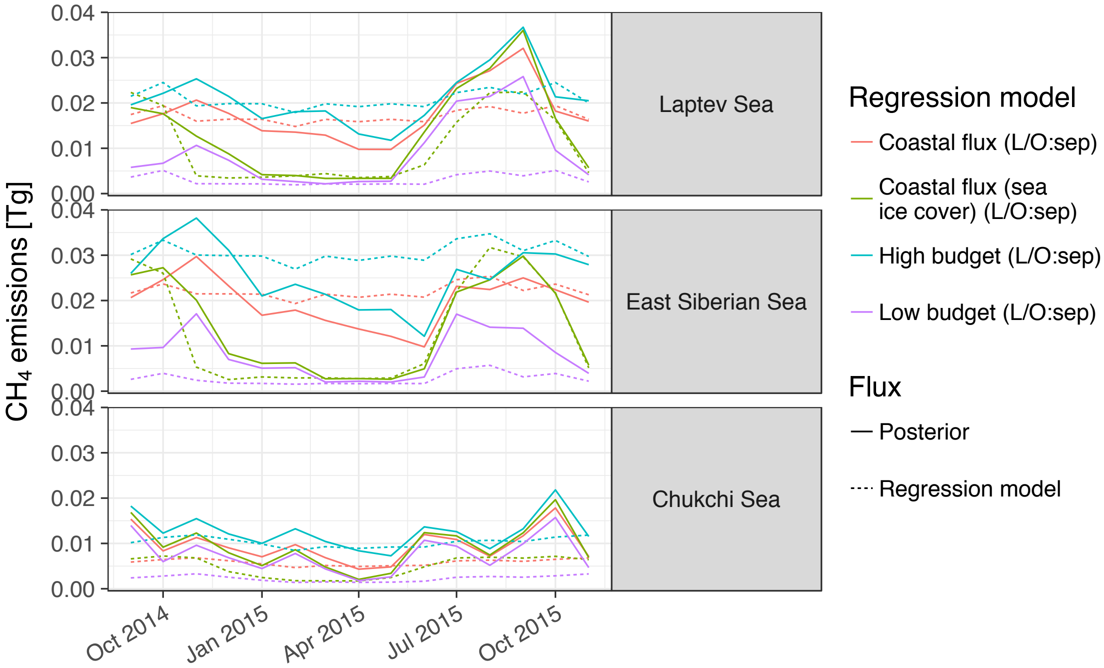

Fig. 30: Monthly CH4 emissions from the three parts of the ESAS between September 2014 and November 2015 for the inversions of the sensitivity study for separating land and ocean signals.

5.2.5.3 Overestimation of terrestrial emissions

Motivation

All best-scoring regression models contained simple auxiliary variables for terrestrial emissions, which were not restricted to estimates of wetland extent that are used by more complex process-based wetland models. These included the constant land flux, the Simple Wetland Model and the Zero Curtain Model. This choice by the model, while fitting the atmospheric data best, invites the question whether ESAS emissions were underestimated because the spatial extent and, in the case of the constant land flux, cold season emissions from the land regions in the domain were overestimated. One inversion was performed in which one of these wide-extent variables (Simple Wetland Model) was not included, because this choice was compatible with the model selection results for one setting (scenario “Coastal flux (no SWM)”). This inversion yielded only minor differences in budgets and flux rates compared to including the Simple Wetland Model (scenario “Coastal flux”, see Fig. 20 and Fig. 21). However, since the constant land flux and the Zero Curtain Model were included, this setup did not exclude an effect of wide-extent terrestrial variables on the ESAS budget.

Implementation

An inversion was performed in which the regression model only featured process-based estimates for terrestrial CH4 emissions. For this setup, the wetland model LPJ-WSL was chosen because it was the most successful one among the wetland models considered in this study. Furthermore, the lake emission model bLake4Me was added. Although it did not rank high among the well-scoring regression models, the fact that the simple models ranked high suggests that LPJ-WSL underestimates the emission area in regions that the station network was sensitive to. Therefore, a regression model that featured both wetland and lake emissions was considered more realistic. For ESAS emissions, only exp-10m was used as auxiliary variable. Sea ice growth was omitted so as to not bias the model towards attributing fall emissions to the ESAS, since the Zero Curtain Model, as the only variable that specifically described terrestrial fall emissions, was not included in the setup either. Results from this inversion were compared to the scenario “Coastal flux”, which featured all of the wide-extent terrestrial variables (constant land flux, Simple Wetland Model, Zero Curtain Model) and LPJ-WSL for terrestrial emissions, and only the coastal variable exp-10m for ESAS emissions.

Results

In the inversion with wide-area terrestrial auxiliary variables, the posterior terrestrial emission budget was 3.5 Tg CH_4 yr^{-1}, whereas in the inversion with only process-based terrestrial auxiliary variables, it was 1.7 Tg CH_4 yr^{-1}. Yet, maximum terrestrial emission rates on the scale of individual grid cells were similar as in the standard inversions (maximum annual average: 20 CH_4 m^{-2} d^{-1}, maximum individual day: 106 mg CH_4 m^{-2} d^{-1}). Emissions from the ESAS increased from 0.9 Tg CH_4 yr^{-1} in the former setup to 1.1 Tg CH_4 yr^{-1} in the latter. Thus, although excluding wide-area variables from the terrestrial emission model reduced the terrestrial budget by 1.8 Tg, it increased the estimate for ESAS emissions only by 0.2 Tg. Therefore, the estimated ESAS emission budget was not strongly affected by potentially overestimated terrestrial emissions in the domain.

The fit to SWERUS-C3 data was only slightly improved due to the lower terrestrial contributions to the signal.

5.2.5.4 Shift in ERA-Interim variables

Due to an oversight in input data preprocessing, ERA-Interim variables were shifted to the south and east by half their original resolution of 0.75°. Thus, in our domain the spatial error in these variables was about 45 km primarily in north-south direction. These variables were used as the basis for several auxiliary variables: gas transfer velocity, Simple Wetland Model and Zero Curtain Model. The preprocessing error was corrected and its impact tested. This may be viewed as a sensitivity test for potential bias in the localization of data grids and horizontal biases in footprint areas. First, the impact on modeled atmospheric mole fractions was tested by comparing modeled signals based on a forward run of the variables with the transport model. Correlations of modeled atmospheric signals were above 0.97 for all variables, indicating the difference between the corrected and uncorrected variables was small. Next, model selection results based on the corrected and uncorrected auxiliary variables were compared for one parameter set (ds:S bc:S bl:5). The comparison of model selection results indicated that there were only minor impacts on all key results. I.e. the spatial and temporal distribution of ESAS emissions, the ranking of all auxiliary variables (affected and unaffected by the error), budgets attributed to individual variables and the ESAS budget range were barely changed. This confirms that our modeling framework was robust against potential biases in the localization of flux controls and or horizontal shifts in footprint position, as long as these shifts are small compared to the overall extension of the model domain. Since the adjustment of ERA-Interim variables was done at a late stage of this work, extensive sets of results had already been produced based on the former, uncorrected input data version. Since our experiments with model selection as described above yielded only minimal effects of incorporating the shifted ERA-interim variables, further inversions with the corrected variables were not performed and all results shown herein are still based on the uncorrected data. However, the previous experience with the model, gained through analyzing the main results and sensitivity tests, indicated that differences of key results like the upper bound of the ESAS budget were typically small between model selection and inversion results. Therefore, we are confident that this oversight did not affect the conclusions of this work.

5.3 Discussion

5.3.1 Influence of model parameters on results

5.3.1.1 Covariance parameters

The large scatter of covariance parameters estimated using RML (Fig. 11) was previously interpreted as low sensitivity of atmospheric data to these parameters (Miller et al., 2016). The sensitivity of the results (budget and spatiotemporal distribution of ESAS CH_4 emissions) on covariance parameters was investigated only in narrow limits in our study, by using the different sets of covariance parameters obtained for strict and relaxed atmospheric data selection, respectively. Thus, uncertainties in covariance parameters were not fully explored. For example, the lower bound of the ESAS CH_4 budget was determined by emission hot spots in the Low ESAS budget scenario whose spatial extent was likely determined by the correlation length. However, in an early stage of this work, very different covariance parameters were estimated because they were based on optimizing for hourly data instead of daily averages. In particular, correlation times were much shorter (2 days compared to 50 days) and model-data mismatches much lower (3 ppb compared to 13 … 17 ppb). This setup was abandoned in favor of daytime averages partly because these covariance parameters indicated overfitting of the atmospheric data. Despite the differences in the model settings, ESAS budgets in these optimizations were similar. Thus, although the uncertainty due to covariance parameters was not fully explored, at least the sensitivity of the annual budget to uncertainties in covariance parameters was likely small.

5.3.1.2 Atmospheric data selection

Regression model selection and inversions were performed with both strict and relaxed atmospheric data selection. Key results were independent of this setting, i.e. the spatial distribution of retrieved emissions and the results related to sea ice were consistent. Only with relaxed atmospheric data selection was the Kolyma mouth variable included in the best-scoring regression models. Since the Kolyma mouth variable attributed highly localized fluxes to the close vicinity of one of the stations used in the optimization (Ambarchik), this result may reflect that relaxed atmospheric data selection included more observations influenced by sources in the near field. Relaxed atmospheric data selection included larger signals into the optimization, which explains why regression model budget estimates were largest with this setting. However, including the Kolyma mouth variable countered the influence of these larger signals on the budget: it attributed atmospheric signals at Ambarchik to a source in the near field that was negligible on the scale of the ESAS, replacing emissions from larger patterns and consequently reducing the budget. This demonstrates the sensitivity of the inverse model to processes in the near field, and highlights both the need for realistic prior emission patterns in the regression model, and the importance of resolving the processes that affect the atmospheric data in order to obtain unbiased results.

5.3.1.3 Boundary conditions

A key factor in the performance of inverse models is the accuracy of boundary conditions. Therefore, we included two sets of boundary conditions in the analyses; both based on a global atmospheric transport model and optimized CH_4 emissions. The difference between the two sets was that for one the influence of the atmospheric data on the global optimization was reduced, and it therefore followed the prior emissions more closely. The idea behind this setting was that it would be less sensitive to the atmospheric data, which may not be realistically modeled by the coarse global model (it mitigated negative emissions in the global optimization). This may imply larger signals attributed to the inside of the domain. However, in the regression model selection, the parameter set with relaxed boundary condition optimization yielded only small differences to the other parameter sets. The relaxed boundary conditions yielded, only among the best-scoring regression models, slightly elevated lower boundaries for and averages of the ESAS budget compared to other settings. Since the setting influenced none of the key results (the range of ESAS budget and the spatiotemporal distribution of the emissions), relaxed boundary condition optimization was omitted in the inversions.

Both sets of boundary conditions may have exhibited seasonally varying biases. A sensitivity test with a simple bias correction (Sect. 5.2.5.1) resulted in a small increase of the upper limit of the ESAS budget (0.3 Tg CH_4 yr^{-1}), but the results on the spatiotemporal distribution of ESAS emissions were not affected by the modification. We do not exclude that a more thorough investigation of boundary condition biases may reveal additional sensitivities, but the key results were fairly robust against the investigated uncertainties and biases in the boundary conditions, which covered both synoptic and seasonal scales.

5.3.1.4 Backtrajectory length

Fluxes were optimized based on two settings for the backtrajectory lengths, i.e. 5 and 15 days. Regression models obtained with the longer backtrajectory length of 15 days tended to yield slightly smaller prior ESAS budgets (average 0.06 Tg), and more models with no ESAS-related auxiliary variables (or only the Kolyma mouth variable) were among the well-scoring models with this setting. Otherwise, spatiotemporal ESAS emission patterns were consistent between the short and long backtrajectories. Similarly, average terrestrial budgets were smaller with the longer backtrajectories (average 0.13 Tg). These results may indicate a bias in the footprints that accumulated over time or different weighting of auxiliary variables (some budgets associated to individual variables were larger with 15-day backtrajectories). However, the observation was not explored further. Instead, both sets of backtrajectories were included in the estimation of the ESAS budget as plausible implementations of the transport by performing inversions for Low ESAS budget scenarios with backtrajectories of 15 days, and the High ESAS budget scenarios with 5 days.

5.3.1.5 Regression model

The regression model had the largest impact on the budget and spatiotemporal distribution of ESAS emissions among the considered parameters. Individual results are discussed in subsequent sections.

5.3.2 Spatial distribution of ESAS emissions

Regression model selection and inversions assigned the largest ESAS emissions to shallow parts of the ESAS. In Sect. 5.3.2.1, the implications of these results for the ESAS CH_4 cycle are discussed. However, the result may also be explained by limitations of the data coverage and model, which is discussed in Sect. 5.3.2.2.

5.3.2.1 Possible process-based explanations of spatial emission patterns

Larger CH_4 emissions to the atmosphere from shallow parts of the ESAS compared to deeper parts of the ESAS suggest that either larger sources to the water column were present there, e.g. due to permafrost degradation, hydrate availability (Sect. 2.6.2) or possibly input of terrestrial carbon (Sect. 2.1.1), or that CH_4 released from the seafloor in deeper parts of the ESAS could be trapped in the water column (Thornton et al., 2016b) due to the pycnocline and dissolution of bubble plumes, and subsequent microbial oxidation. Retrieved emission hot spots in the Low ESAS budget scenarios may be explained by unique local conditions, e.g. dissolved CH_4 carried by the Kolyma river (Shakhova and

Semiletov, 2007) or warming of the seafloor e.g. by the Lena river (Semiletov et al., 2005). Shallow ocean variables assigned lower emission rates to the Chukchi Sea compared to Laptev and East Siberian Seas, and may therefore also imply differences between those regions other than ocean depth or permafrost and hydrate availability like marine biogeochemistry (Sect. 2.1.1).

5.3.2.2 Limitations

Uneven sensitivity of the atmospheric observation network

It was not investigated whether the dominance of shallow ESAS regions or non-detection of other spatial emission patterns like the hot spot map by Shakhova et al. (2010a) was a result of a lack of sensitivity of the atmospheric observations to these patterns. In particular, hot spots identified in the inversions without ESAS variables in the regression model were close to the stations Ambarchik and Tiksi, respectively. Thus, they may be the result of the large sensitivity of the stations to their vicinity. By contrast, deeper parts of the ESAS were comparatively scarcely sampled (Fig. 10), and emissions from these areas may thus have been undetected. In the inversions with constant prior emissions from the ESAS, emissions were partly redistributed towards the coast. Although this analysis does not replace better sampling, it suggests that the preference of coastal emissions was not an artifact of the sensitivity of the atmospheric observation network.

Cross-influence of terrestrial emissions on retrieved ESAS emission patterns

As explained in detail in Sect. 5.2.5.2, estimated coastal ESAS emissions may have been influenced by terrestrial emissions, which were estimated to be larger than ESAS emissions, due to the ambiguity of atmospheric transport. The dominance of shallow ocean variables was robust against removing ambiguous data from the Ambarchik record (Sect. 5.2.5.2), suggesting that it may not be the result of cross-influence from terrestrial emissions. However, this sensitivity test did not provide conclusive evidence against the cross-influence hypothesis, because ambiguous data from Tiksi and Barrow were not removed due to a shortage of data from these stations that dominantly sampled the ESAS, and because transport model accuracy was not investigated. Another argument against the cross-influence hypothesis is that the models that fit the atmospheric data best were those that featured an auxiliary variable for oceanic emissions, suggesting that terrestrial emissions alone did not explain the atmospheric data. Furthermore, Variance Inflation Factors did not indicate collinearity, suggesting that the model was able to distinguish between oceanic and terrestrial emissions. Overall, the emission pattern of dominant emissions from shallow waters appeared robust, but confusion with terrestrial emissions was not ruled out conclusively as the reason behind the pattern.

5.3.3 Cold season emissions and the role of sea ice

In fall, estimated ESAS CH_4 emissions were larger than was predicted by regression models and higher than during other times of the year in many inversion scenarios. The large emissions were linked to sea ice growth. In the period of highest ice cover, the observations were compatible with a wide range of emission estimates, between the lowest during the study period to rivaling those of the lowest ice cover in summer. During sea ice retreat, no outstanding emission spike was detected on a monthly timescale. The implications of these results for the controls of emission processes related to sea ice are discussed here. As was the case with the spatial distribution of the emissions, limitations of the model and the atmospheric observation network were important for the interpretation of these results and are discussed subsequently.

5.3.3.1 Possible process-based explanations temporal emission patterns

Large CH_4 emissions were modeled in fall in particular in the East Siberian Sea, far exceeding emissions in summer and linked to the sea ice growth auxiliary variable. This link suggests considerable CH_4 emissions due to mixing of the water column and/or brine rejection during sea ice formation. Although gas transfer velocity and thus wind speed was not linked to the high fall emissions by the model, they nonetheless roughly fit the temporal pattern (Fig. B.1) and were, due to limitations of all auxiliary variables, not ruled out as a potential control of the large fall emissions.

Modeled winter emissions were larger than was suggested by regression models that modulated ESAS emissions with sea ice cover, which suggests the presence of CH_4 emissions through areas of open water in winter. This has been observed in the central Arctic ocean before (Kort et al., 2012) and suggested for the ESAS as well (Shakhova et al., 2015). Emissions in winter may be enhanced by brine rejection during refreezing of leads, analogous to sea ice growth in fall. Strongly enhanced emission rates compared to the open ocean would be necessary to explain the high area-average emission rates during this period, since the smaller emission area would have to be balanced by the emission rate. Given literature estimates on enhanced air-sea gas transfer in openings in sea ice cover (Sect. 2.4), this may be possible. In April and May, estimated emissions were lower and in some inversion scenarios close to zero for all regions of the shelf. This may be explained if the cumulative open water area that the atmospheric observation network is sensitive to was smaller during this period, and/or refreezing ceased (total Arctic sea ice cover already decreased during this period). Seasonal patterns of lead area fraction may be compatible with this hypothesis. The seasonality of lead area fraction in the Beaufort Sea would fit (Fig. 1c in Wang et al., 2016). Actual conditions in the ESAS, in particular considering the spatial distribution of posterior emissions, were not investigated. Therefore, this hypothesis remains speculative. Overall, the description of cold season emissions from the ESAS may be improved by including auxiliary variables that describe the area of and ice production in leads and polynyas in the regression model.

The retreat of sea ice was not identified as a pattern correlating with considerable CH_4 emissions, and no outstanding spike of emissions during this period was detected in optimized fluxes either. Thus, the release of CH_4 that may have accumulated under (or in) ice was limited. This result suggests that accumulation below and in sea ice was limited, that release of large amounts of CH_4 was prevented by increased stratification due to the melt water layer (Damm et al., 2015a; Kitidis et al., 2010), or both. Limited accumulation is compatible with our result of sustained CH_4 emissions in winter, which may be attributed to fractures in the ice cover. Accumulation may also be limited due to microbial consumption of trapped CH_4 (compare e.g. Li et al., 2017) and under-ice lateral transport to other parts of the Arctic Ocean (Damm et al., 2018; Shakhova et al., 2015).

5.3.3.2 Limitations

The high ESAS emissions retrieved for fall and associated with sea ice growth were sensitive to data selection. In the sensitivity study with data filtered for a clear separation of land- and ocean-influenced signals at Ambarchik, the detection of the sea ice growth variable vanished, and shelf-wide integrated fall emission rates did not exceed those of summer (Sect. 5.2.5.2). Thus, this sensitivity study suggests that strong atmospheric signals in fall at Ambarchik that were attributed to the East Siberian Sea may have been of terrestrial origin instead (possibly from the near field not resolved by the model). Thus, brine rejection and subsequent water column mixing in fall may have played a considerably less important role than inferred based on the "standard" atmospheric data selection criteria. This highlights the importance of selecting atmospheric data for transport situations that can be modeled reliably in inverse modeling studies.

The wide range of emission estimates for winter emissions indicates dependence on the prior and thus low sensitivity of the atmospheric data to such emissions. The result was partly influenced by the large emissions estimated for fall 2014, but winter emissions were also retrieved in the sensitivity study for confusion of land and ocean fluxes, where this fall signal was removed (Sect. 5.2.5.2). In general, winter results may be less accurate than summer results, since the frequent temperature inversions during this period are difficult to capture by atmospheric transport models (Kilpeläinen et al., 2012) and may cause overestimation of emissions (John Henderson, personal communication). Large CH_4 enhancements over background conditions were recorded at Ambarchik throughout the winter (Fig. 6). Although the data were filtered for difficult transport situations like temperature inversions and low wind speeds, influence by the abovementioned problems was not excluded. To summarize, there may be considerable CH_4 emissions from the ESAS during the ice-covered period, but the result might have been influenced by model limitations.

The fact that the auxiliary variable that described sea ice retreat was not identified as an emission pattern may have had to do with shortcomings of the variable (Sect. 5.1.7.1). Nonetheless, posterior emission estimates also did not indicate outstanding emissions during this period; unlike it was the case with fall emissions. Thus, CH_4 emissions due to sea ice melt appeared to be limited.

5.3.4 No direct detection of link between CH_4 emissions and wind speed

Auxiliary variables that linked emissions to wind speed (gas transfer velocity and occurrence of storms) were not detected as dominant CH_4 emission patterns. The auxiliary variables were based on daily average wind speeds and thus represented gas exchange at the air-sea interface. However, another wind effect is mixing of the water column, and this would likely be better represented by wind speed averages over longer periods (Markus Janout, personal communication). On the other hand, the effect of wind speed may indeed be limited, as the depth of mixing due to typical wind speeds in the ESAS may be small (Thornton et al., 2016b). The effects of wind speed on CH_4 emissions could have been masked by other variability. In particular, the gas transfer velocity variable had its largest values in the Chukchi Sea (Fig. B.1). This area was consistently retrieved as a small emitter compared to other parts of the ESAS. This might be related to smaller seafloor emissions from this area. Modifying wind speed- related auxiliary variables accordingly may yet make an influence of wind speed on CH_4 emissions from the ESAS detectable through regression model selection.

5.3.5 Heterogeneity of ESAS CH_4 emissions

Posterior emission estimates varied significantly in space and time. Annual average flux rates on the grid scale (32 km × 32 km) were up to 5 times the maximum estimate of the annual ESAS-wide average flux rate (9.2 vs. 1.9 mg CH_4 m^{-2} d^{-1}). Flux rates on individual days on grid scale were up to 20 times the ESAS-wide average (37 mg CH_4 m^{-2} d^{-1}). These numbers depend on the covariance parameters, i.e. shorter correlation lengths and times would result in more localized and shorter emission spikes with higher emission rates. Thus, these numbers do not cover localized, short emission events that can occur in the ESAS. Rather, the results demonstrate that the atmospheric data are compatible with a large heterogeneity of ESAS CH_4 emissions on the scales of the correlation lengths and times in this study, i.e. on the order of 400–500 km and 50–60 days.

5.3.6 Kolyma mouth

The hypothesis of elevated CH_4 emissions from the Kolyma mouth region compared to other parts of the ESAS fit the general flux pattern of the Low ESAS budget and Constant ESAS emissions scenarios, in which posterior emissions were elevated compared to the regression model in the area. However, the emissions may have been part of the larger pattern that ESAS emissions were attributed primarily to shallow waters and not exceptionally high compared to other coastal regions. As part of regression models, the variable was assigned a negligible budget (< 0.05 Tg CH_4 yr^{-1}) despite the large impact it had on modeled atmospheric signals at Ambarchik when selected (Sect. 5.2.3.5). This had a small impact on ESAS budget calculations (see 5.3.8).

As the area was part of the coastal emission flux pattern, elevated emissions attributed to the Kolyma mouth delta may have been confounded by signals that originated from adjacent land areas (cf. Sect. 5.3.2.2).

5.3.7 Evaluation of comparison with SWERUS data

Modeling SWERUS-C3 data supported the Low ESAS budget scenarios, since ESAS-related auxiliary variables overestimated the atmospheric signals observed during this campaign. However, the largest CH_4 excess over boundary conditions, which was convincingly linked to a local oceanic CH_4 seep by Thornton et al. (2016b), was attributed to the Simple Wetland Model, and not reproduced when this variable was not included in the regression model. This demonstrates that individual local CH_4 sources far from the stations were hard to capture for the inverse model. It also suggests that the Simple Wetland Model overestimated terrestrial CH_4 emissions.

SWERUS-C3 data were more sensitive to areas around the New Siberian Islands than other coastal regions. Thus, the results suggest that the ESAS-related auxiliary variables, which produced atmospheric signals not observed by SWERUS-C3, are not valid in this area.

However, the explanatory power of results based on the SWERUS-C3 dataset is limited: the data set was short, with only 19 daily averages over a period of 1 month of observations passing quality control. Modeled atmospheric data used in the optimization also exhibited considerable biases on this timescale (Fig. 27). In addition, SWERUS-C3 covered the period July 15–August 11, 2014, but atmospheric data for optimization were used only from August 1, 2014. This start date was chosen to keep the atmospheric network consistent over the inversion period (the Ambarchik record started on Aug 9, 2014). Therefore, posterior emissions used to model SWERUS-C3 data may be less accurate than during the rest of the inversion period. To summarize, the model-data mismatch with SWERUS-C3 data supports the Low ESAS budget scenario, but also reveals that the coastal atmospheric observation network lacks sensitivity to individual local emission hot spots in off-shore parts of the ESAS.

5.3.8 ESAS CH_4 budget range and its uncertainties

Posterior budget estimates (0.4–1.5 Tg CH_4 yr^{-1}) were on the lower end of literature estimates. While the exact magnitude of posterior ESAS CH_4 budget estimates varied with the regression model and through various sensitivity studies, the main conclusion that ESAS emissions were low remained robust. In the following paragraphs, we evaluate the bounds of the budget range and discuss factors that may alter the result.

The High ESAS budget scenario (1.5 Tg CH_4 yr^{-1}) featured a shallow ocean variable (exp-20m) and the sea ice growth variable, the latter of which was assigned up to 0.5 Tg CH_4 yr^{-1} in the well-scoring regression models. This variable did not distinguish between shallow and deep parts of the ESAS. Since emissions appeared to be higher in shallower parts of the ESAS (Sect. 5.3.2), this variable may fit the atmospheric data better if it were modulated by ocean depth. Also note that the success of the sea ice growth variable was driven by signals observed at one station (Ambarchik) and may have been the result of confusion with terrestrial (near field) signals (discussed below).

ESAS CH_4 budget estimates may have been influenced by potential biases in the boundary conditions, which overestimated some of the baseline observations at Tiksi (Fig. 17) and Barrow (Fig. 19). A sensitivity study with a simple bias correction yielded posterior ESAS budgets of up to 1.8 Tg CH_4 yr^{-1}, compared to 1.5 Tg in the standard inversions (Sect. 5.2.5.1). However, it is not certain that all negative CH_4 enhancements indicated biased boundary conditions: the large variability of the boundary conditions suggests that they may have been influenced by regional CH_4 sources that are difficult to represent with the comparatively coarse global inverse model that was used for inferring the boundary conditions (Fig. 6). Thus, the boundary conditions may be smoothed instead of biased. The 0.3 Tg increase in the ESAS budget estimate yielded by the sensitivity study on the simple bias correction was used as the order of magnitude of the uncertainty due to boundary condition biases.

In the Low ESAS budget scenarios the regression model assigned zero emissions to the ESAS, or only the emissions of the Kolyma mouth variable that were negligible compared to the range of shelf-wide budget estimates. Thus, posterior emissions in these scenarios reflected the lowest ESAS emissions that were necessary to explain the atmospheric data, i.e. it attributed emissions to areas the observations were sensitive to, and no "extrapolation" of these signals via the regression model took place. Posterior emissions in the Low ESAS budget scenarios were 0.4–0.6 Tg CH_4 yr^{-1} depending on whether the averaging period included fall 2014. The Kolyma mouth variable did not influence the lower bound of the ESAS budget estimates. Posterior emissions in the Low ESAS budget scenarios could have been part of the larger pattern that ESAS emissions in shallow waters dominated. In this and other inversions with prior ESAS budgets of less than about 1 Tg CH_4 yr^{-1}, posterior emissions were also larger than prior emissions, but the difference became smaller with larger prior estimates. This indicates that the flux patterns used in these scenarios, including the lower bound of our budget estimates, underestimated the total emissions as seen by the atmospheric data.

We speculate that emissions attributed to the ESAS might have been confounded with terrestrial emissions in the domain (Sect. 5.2.5.2). This applies in particular to fall emissions associated with sea ice growth (Sect. 5.3.3.2), but was also not conclusively excluded as a reason behind the model's preference for coastal emissions (Sect. 5.3.2.2). Thus, the upper bound of the ESAS CH_4 budget may be much smaller than was estimated here. The budget range in the sensitivity study designed to test this was 0.3–0.7 Tg CH_4 yr^{-1} (Sect. 5.2.5.2), reducing the upper bound by 0.8 Tg compared to the standard setup. Since the terrestrial budget was also lower in this test, the influence might be from the near field of Ambarchik, provided the atmospheric transport model captured the large-scale circulation sufficiently well. Thus, the results of this sensitivity study supported a lower range for the ESAS CH_4 budget.

A possible overestimation of terrestrial emissions only had a small effect on ESAS emission estimates. A sensitivity test with only process-based terrestrial emission models yielded a decrease of 1.8 Tg CH_4 yr^{-1} of the terrestrial budget, but only a 0.2 Tg increase of the ESAS budget. The reason may be that process-based models locate large emissions close to the atmospheric stations and at some coastal areas. Therefore, the budget reduction in this sensitivity test may have stemmed from inland regions to which the atmospheric observations were not sensitive and that were unlikely to be mixed up with signals that originated from the ocean. The results of this test indicate that the ESAS budget was not considerably underestimated due to a possible overestimation of the terrestrial emissions.

Assigning emissions to the Kolyma mouth partly explained atmospheric signals at Ambarchik and therefore reduced ESAS regression model budget estimates on the high end by 0.24 Tg CH_4 yr^{-1} in the case of relaxed data selection (average). One pair of inversions was performed that differed only in the inclusion of the Kolyma mouth variable in the regression model. In this example, regression model budgets were 0.17 Tg smaller when including the Kolyma mouth variable, and posterior emissions were 0.13 Tg smaller. Thus, the effect of the variable on the budget was reduced in the posterior estimate. Based on these numbers, we estimate that the reduction of the upper bound of the ESAS budget estimate when the Kolyma mouth variable was included was on the order of 0.2 Tg CH_4. As concluded in Sect. 5.3.1.2, this highlights the influence that near field emissions can have on inversion results and the need for realistic CH_4 emission patterns for the regression model.

A comparison with data from the SWERUS-C3 campaign, which covered central parts of the shelf, revealed that local CH_4 sources far offshore might have been difficult to capture by the coastal atmospheric observation network. Although there were indications that widespread large emissions further offshore compared to coastal emissions were not compatible with the atmospheric data (Sect. 5.3.2), the ability of the observations to constrain emissions far offshore was likely limited (Fig. 10).

As discussed above, the estimated ESAS budget was sensitive to the regression model. Given the moderate agreement between regression models and atmospheric data (Sect. 5.2.3.5), the considered regression models may have been incomplete. More realistic regression models could alter the range of budget estimates.

To summarize, although the estimated budget range was sensitive to several factors, none of the quantified influences altered the main conclusion that the budget was low compared to literature estimates.

5.4 Summary

In this section, the results of the study presented in this chapter are summarized, along with possible interpretations and a summary of the limitations. A summary of which estimates and hypotheses in the literature are supported by the main results can be found in the conclusions of the thesis (Chapter 6).

In this chapter, CH_4 emissions from the East Siberian Arctic Shelf to the atmosphere were estimated. The study was based on a geostatistical inverse model of atmospheric CH_4 transport and atmospheric CH_4 mole fractions measured continuously at three sites located at the coast of the shelf (Ambarchik, Barrow and Tiksi) for the period July 2014 – December 2015.

Key results on the shelf-wide spatiotemporal distribution of ESAS CH_4 emissions, possible interpretations as well as the most important limitations of their validity, were as follows:

1. Estimated annual CH_4 emissions from the ESAS to the atmosphere were 0.4–1.5 Tg CH_4 yr^{-1}, and thus on the low end of literature estimates (Table 1). The range depended primarily on the regression model.

   The range of ESAS budgets as cited above may be over- or underestimated due to potential systematic biases in input data. Factors that may have contributed to an underestimation of the upper limit of the budget were biases in boundary conditions (+0.3 Tg) and overestimation of terrestrial emissions (+0.2 Tg). Additional factors of unknown quantity include incomplete regression models and a lack of sensitivity of the coastal observation network to far offshore parts of the ESAS. Factors that may have contributed to an overestimation of the budget were confusion of ESAS signals with those from terrestrial (possibly near field) emissions (-0.8 Tg) and a potential local influence of emissions from the Kolyma mouth on data from Ambarchik (-0.2 Tg). The latter may also be viewed as an indication for the general sensitivity of the results on emissions in the near field of the observation network.

   The combined effects of these factors on the budget were not computed and may be different than their sum.

   To summarize, several factors might have contributed to an over- or underestimation of the budget, but none indicated an alteration of the main conclusion that the estimated budget was on the low end of those in the literature.
2. The atmospheric observation network attributed ESAS CH_4 emissions primarily to shallow waters. Deeper, further off-shore regions were not detected as dominant emitters. This result indicates that CH_4 emissions from the seafloor are trapped in the water column in deeper waters, and/or that emissions from shallow waters are higher. The pattern also correlated with the result that Chukchi Sea emissions were in general estimated to be smaller than those from the Laptev and East Siberian Seas, which may also be related to marine biogeochemistry. We speculate that the result may have been influenced by confusion of ESAS signals close to the shore

with terrestrial emissions, and by a lack of sensitivity to deeper parts of the ESAS. There were indications that the result was robust against both errors (see Sect. 5.2.5.2 and Sect. 5.2.4.6, respectively), but the conducted analyses did not conclusively exclude them.

3. The highest CH_4 emissions from the ESAS may have occurred during fall. This would indicate an important role of sea ice formation on CH_4 release to the atmosphere via brine rejection and subsequent mixing of the water column, and/or increased wind speeds during this period. However, the outstanding fall signal may have been confounded by terrestrial signals, possibly from the near field around Ambarchik, as it was not retrieved in a sensitivity study designed to test for this possibility (Sect. 5.2.5.2).
4. During the ice-covered period, the atmospheric data were compatible with a wide range of emission rates, on the low end lower than during all other times of the year, and on the high end rivaling those from the period of lowest ice cover. Emissions during this period may be related to areas of open water in the ice cover, i.e. leads and polynyas. In these open water areas, considerably elevated rates of gas exchange compared to open water have been reported in the literature and linked to water column mixing due to cooling and refreezing. However, the wide range of estimates indicates limited sensitivity of the atmospheric data to winter emissions and dependence on the regression model. Furthermore, we speculate that the atmospheric transport model may be less accurate in winter due to difficult-to-model transport situations like temperature inversions, which may cause large atmospheric CH_4 signals to build up and be erroneously interpreted as large emissions by the model. To summarize, while the results indicated potentially considerable emissions during the ice-covered period, their magnitude was both less well constrained than during summer and possibly biased towards higher values.
5. Emissions during ice breakup were limited. This result could indicate limited accumulation of CH_4 under the ice, and/or that the melt water layer inhibited release to the atmosphere. Sustained emissions during the ice-covered period, which were compatible with the atmospheric data (see above), are one factor that could explain limited accumulation. Limited sensitivity of the atmospheric data as a factor contributing to this result was not investigated.

The uncertainties common to several key results were a potential confusion between atmospheric terrestrial and oceanic emissions, as well as limited sensitivity of the atmospheric observation network and difficult-to-model transport situations. In addition, not detecting a direct link between a process and CH_4 emissions does not necessarily imply that the process was not relevant, but may also be due to shortcomings of the auxiliary variables, lack of sensitivity of the atmospheric network, or masking by other variability, as using BIC for the evaluation of regression models put a strong focus on first order controls. Uncertainties of the results on fall and winter emissions highlight the need to investigate transport model accuracy and select atmospheric data for transport situations that can be reliably modeled.

Besides the main results on shelf-wide emission patterns, a number of additional results were obtained:

1. Emission estimates had a large spatiotemporal variability. This may make upscaling of local measurements difficult, and may contribute to differences between estimates of the annual ESAS CH_4 budget in the literature.
2. The Kolyma mouth may be one of the regions of enhanced CH_4 emissions to the atmosphere in the ESAS, but may also be part of the larger pattern that emissions in shallow waters of the ESAS dominate.
3. The hotspot map by Shakhova et al. (2010a) ranked low among the well-scoring regression models and attributed low emissions (< 0.2 Tg CH_4 yr^{-1} in any scenario or sensitivity test).
4. In all scenarios, emissions from the Chukchi Sea were on the low end of the respective estimate. This result may be related to ocean depth, but also to marine biogeochemistry and emissions from the seafloor.
5. A comparison of modeled atmospheric CH_4 mole fractions with data from the SWERUS-C3 campaign indicated that the model could not capture localized CH_4 seeps in the outer part of the shelf.

The method required optimizing terrestrial emissions in the domain. Although these were not the focus of this study, some observations may be of interest to the reader:

1. Terrestrial emissions were best described by a combination of simple models (constant flux from the whole land surface in the domain, Simple Wetland Model), a process-based wetland model (LPJ-WSL), and a crude description of zero curtain emissions.
2. The majority of the terrestrial CH_4 emissions budget was attributed to the simple models. These models assigned emissions to the whole land area in the domain, whereas in the process-based wetland models that were considered here, emissions were spatially limited to estimates of wetland extent. Therefore, we speculate that estimates of wetland extent, which differ considerably between models (Melton et al., 2013), may be inaccurate in the vicinity of the atmospheric stations used in this study.
3. Estimated terrestrial emission budgets in the domain were compatible with the sum of bottom-up estimates of emissions based on process-based wetland and lake models. However, such sums suffer from ambiguity between small lakes or ponds and wetlands and thus double-counting of emissions (Thornton et al., 2016a).

Therefore, our estimates of the terrestrial emissions may be larger than suggested by process-based models. A comparison of modeled atmospheric CH_4 mole fractions with data from the SWERUS-C3 campaign indicated that terrestrial emissions might have been overestimated by the Simple Wetland Model. When restricting prior terrestrial emission estimates to process-based models, the budget decreased by 50 %, which may, for the above reasons, be more realistic.

4. The fact that the crude model of zero curtain emissions was important for explaining atmospheric signals indicates that terrestrial emissions in the area in fall were not well described by process-based models.

In addition to the result-specific limitations outlined above, all results are subject to general limitations of the methods and uncertainties that were not fully explored. These include the accuracy of boundary conditions (see Sect. 5.3.1.3), general transport model accuracy (see Sect. 3.1.3), sensitivity of the atmospheric observations to certain processes and transient or localized sources (see e.g. Sect. 5.3.7), accuracy of covariance parameters (see Sect. 5.3.1.1), as well as near field emissions and representativeness of observations (see Sect. 3.1.3).

6 Conclusions

6.1 Summary, context and relevance of research findings

With this thesis, two major goals were pursued: improving the data coverage on CH_4 emissions from the East Siberian Arctic Shelf to the atmosphere and using these data to estimate these emissions. The results on both objectives are presented in the following sections.

6.1.1 Accurate greenhouse gas observations at Ambarchik

To improve the data coverage on CH_4 emissions from the East Siberian Arctic Shelf to the atmosphere, the new atmospheric greenhouse gas observation station Ambarchik was established. The station delivers data with precision and accuracy suitable for inverse modeling studies without major downtime since its installation in August 2014. The station is a valuable addition to the sparse network of atmospheric greenhouse gas observations in the Siberian Arctic. Thus, the data obtained at Ambarchik hold the potential to improve our knowledge on CO_2 and CH_4 exchange processes and the carbon cycle in this region, which currently experiences rapid climate change. This is of particular interest in light of the vast carbon reservoirs in the region, which, if destabilized, could constitute a positive feedback to global climate change. The Ambarchik station continues to operate and the data are documented in an article that is currently under review for the journal Atmospheric Measurement Techniques (Reum et al., 2018a). The data are available to the community upon request.

A side product of the calibration efforts for Ambarchik was an improvement in the correction of the effects of water vapor on CO_2 and CH_4 measurements with the widely used greenhouse gas analyzers manufactured by Picarro, Inc. Since the improvement was small compared to the large signals analyzed in this study, it was not presented in detail. Nonetheless, the new method contributes to keeping the uncertainty of measurements obtained with Picarro analyzers within the WMO inter-laboratory compatibility goals for atmospheric CO_2 and CH_4 observations, which were set to ensure the accuracy of fluxes estimated based on inverse modeling techniques. Like the Ambarchik station description, this work is currently in review for the journal Atmospheric Measurement Techniques (Reum et al., 2018b).

6.1.2 Constraints on CH_4 emissions from the East Siberian Arctic Shelf to the atmosphere

Emissions of CH_4 from the ESAS to the atmosphere were estimated in an inverse modeling study. It was the first study to approach the subject by optimizing shelf-wide emissions on high spatial and temporal resolution. It further expanded on previous work by exploiting data from the new station Ambarchik and by utilizing geostatistical inverse modeling techniques to provide a top-down perspective on spatiotemporal emission patterns. One aspect of the geostatistical method is the representation of prior knowledge on emissions via a linear combination of emission patterns optimized for the atmospheric data. A set of potentially relevant emission patterns was developed based on the literature on ESAS CH_4 emissions and their underlying mechanisms. Evaluating which combinations ("regression models") fit the atmospheric data best allowed some insight into the first-order controls of the emissions and assessment of the underlying mechanisms. Further results were obtained from optimizing fluxes starting with these regression models as initial guesses. Here, we summarize which estimates of the magnitude and hypotheses on controls on ESAS CH_4 emissions in the literature are supported by this study. A more comprehensive summary including minor results and additional details on limitations was given in Sect. 5.4.

The estimated CH_4 emission budget of the ESAS (0.4–1.5 Tg CH_4 yr^{-1}; see Sect. 5.3.8 for details on possible over- or underestimation) was on the lower end of literature estimates. It was previously suggested that ESAS CH_4 budget estimates on the high end might be related to a focus of observations on coastal areas (Thornton et al., 2016b). This assessment is compatible with a key result of the present study, i.e. the dominance of CH_4 emissions from shallow ESAS waters compared to deeper waters, as the coastal areas of the ESAS are also its shallowest areas. The controls compatible with this pattern are trapping of CH_4 in the water column in deeper waters, as was previously inferred for the Beaufort Sea (Sparrow et al., 2018), and/or comparatively large CH_4 emissions to the shelf water in shallow regions of the ESAS compared to deeper regions. Besides the pattern of dominating shallow-water emissions, our results also support a large spatiotemporal heterogeneity of the emissions (Sect. 5.3.5), which, on the one hand, makes upscaling sparse data difficult, and on the other hand implies that emissions may be different in areas the atmospheric data in our study were not sensitive to (i.e. far off-shore, deeper parts of the shelf). Both limitations could have contributed to differences between budget estimates of this and previous studies. Lastly, other top-down studies put larger upper bounds on the budget, but argued that these may have been too high. Assuming emissions from deeper ESAS waters are indeed small as suggested by Thornton et al. (2016b) and thus not overlooked, our study narrowed down the plausible range of the annual ESAS CH_4 budget.

The fate of CH_4 during the ice-covered period was previously identified as a knowledge gap (e.g. Thornton et al., 2016b). One hypothesis is accumulation of significant amounts of CH_4 during the ice-covered period and sudden release to the atmosphere during sea ice melt (Shakhova et al., 2010a). However, our estimated CH_4 emission rates during this period, integrated over the whole shelf area, did not exceed those of summer, which suggests that release of accumulated CH_4 during the melt period was limited. This result is consistent with limited accumulation (Damm et al., 2018; Kitidis et al., 2010; Kort et al., 2012; Shakhova et al., 2015) and/or restricted release during melt (Damm et al., 2015b; Kitidis et al., 2010). Of the various mechanisms that may be responsible (Sect. 5.3.3), only sustained CH_4 venting during the ice-covered period could be assessed within this study. The results during this period were uncertain but compatible with sustained winter emissions. These may be associated with fractures and open water areas, i.e. leads and polynyas, which are present in Arctic sea ice throughout the winter. Gas exchange rates through these fractures can be much larger than in open water areas due to mixing of the water column induced by refreezing (e.g. Else et al., 2011). Thus, high emission rates from fractures in the sea ice may be a key mechanism for CH_4 release from the ESAS to the atmosphere and the effectiveness of sea ice as a barrier for CH_4 emissions from the ESAS to the atmosphere appears limited.

Previous work suggested high CH_4 emissions from the ESAS during fall due to mixing of the water column during storms (Shakhova et al., 2014). Our results were compatible with strong fall emissions compared to the rest of the year, but possibly related to sea ice growth. We regard this result with caution because a sensitivity test suggested it might have been influenced by terrestrial (possibly near field) emissions at Ambarchik.

To summarize, the results of the study on ESAS CH_4 emissions indicated they are on the low end of literature estimates. Patterns of the spatial and temporal distribution of emissions were retrieved that lend support to certain hypotheses on the dominant emission controls from the literature, in particular a dominance of emissions from shallow waters, no outstanding emission peak during sea ice melt, as well as possibly large emissions during fall and sustained emissions during the ice-covered period. However, these patterns may have been influenced by several limitations of the model and data coverage. In particular, ESAS emission estimates may have been confounded by terrestrial emissions, atmospheric data lacked sensitivity to offshore, deep parts of the shelf, and the transport model may have been less accurate in winter than in summer (see Sect. 5.4 for a comprehensive summary of the limitations). Several sensitivity studies indicated robustness of the key results with respect to some of the limitations, with the exception of outstanding fall emissions. Nonetheless, the retrieved patterns should be understood as indications rather than conclusive evidence. Ways to overcome key limitations of this study are proposed in Sect. 6.2.

6.2 Outlook: improving ESAS CH_4 emission estimates based on atmospheric data

In this section, we discuss how key limitations of this study on ESAS CH_4 emissions could be overcome.

Key limitations of this study were the role of separation of terrestrial from oceanic signals and limited sensitivity of the observations to deeper parts of the shelf. A simple way to test for these limitations would be observation system simulation experiments (OSSEs). For example, one could create artificial atmospheric data based only on terrestrial emissions and test whether the model selection indicates the presence of emissions from shallow ESAS areas, as it was the case with the real data. For such tests, uncertainties of the observations and of the transport model need to be represented adequately, for example by generating artificial observations using a different transport model.

Central parts of the shelf were sampled in a previous ship-based campaign that did not reveal widespread large CH_4 emissions in the area (Thornton et al., 2016b), but the observation period and area of such campaigns is limited. Therefore, more observations that are more sensitive to the shelf and less sensitive to terrestrial emissions could provide additional insights. The station Baranov on the New Siberian Islands, which began operation in late 2015 (Tuomas Laurila, personal communication), may prove useful for this purpose.

There are several ways to improve the inverse model. One way would be a better description of terrestrial CH_4 emissions in the domain. In particular, a crude description of zero-curtain emissions was among the successful auxiliary variables and at the same time, ESAS emission estimates during fall may have been strongly influenced by terrestrial signals. In addition, we speculate that wetland extent in process-based wetland models may be inaccurately represented in the vicinity of the atmospheric stations because model selection preferred simple, wide-extent models to process-based models for the majority of the terrestrial emission budget. The influence of these simple models on the inferred ESAS budget was limited (Sect. 5.2.5.3), but better descriptions of the spatial extent of terrestrial CH_4 emissions and in particular cold season emissions may nonetheless improve the accuracy of ESAS CH_4 emission estimates.

Likewise, improved descriptions of ESAS CH_4 emission processes and seafloor emission patterns could improve our understanding of their role in the ESAS CH_4 cycle and better constrain the emissions to the atmosphere. Improvable process descriptions include in particular the distribution of local emission hotspots, transient emissions (or, more general, the spatiotemporal distribution of sources of CH_4 to the shelf water), leads and polynyas in sea ice, controls on mixing of the water column, sea ice melt and lateral transport via ocean currents.

Investigating transport model quality and refining selection criteria for atmospheric data could help reduce the confusion of terrestrial and oceanic emissions, the influence of near field emissions, and evaluating the accuracy of results especially during the cold season, when difficult-to-model transport situations are prevalent in the Arctic.

More accurate boundary conditions may improve the accuracy of the model. The results appeared to be fairly robust against differences between the two sets of boundary conditions used in this study as well as against seasonally varying biases, but the uncertainty in this quantity was certainly not fully explored.

Refined covariance models could be used to test certain hypotheses and robustness of results. For example, imposing a smaller prior covariance on emissions close to the shore could force the model to react with increasing emissions in offshore parts of the ESAS.

Emissions from the ESAS to the atmosphere were only considered for the extent of the ESAS itself in this study. For a more comprehensive picture of the ESAS CH_4 cycle, lateral transport with ocean currents (Damm et al., 2018) needs to be taken into account.

Lastly, case studies of individual atmospheric signals could provide further insights on localized and/or transient CH_4 sources in the ESAS.

Appendix A Details on Ambarchik hardware and quality control

In the following sections, details on the atmospheric greenhouse gas measurement system and the data gathered at Ambarchik are given. Similarly to Chapter 4, the material presented here is an edited version of the appendix of Reum et al. (2018a).

A.1 Ambarchik station hardware

Table A.1: Gas handling components (labels as in Fig. 2).

Description	Label	Manufacturer	Model
CRDS analyzer	CRDS analyzer	Picarro	G2301
Membrane pump	MP1	Picarro	Picarro vacuum pump
Piston pump	PP1	Gardner Denver Thomas	617CD32
Flow meter	FM1	OMEGA	FMA1826A
Flow meter	FM2	OMEGA	FMA1814A-ST
Flow meter	FM3	OMEGA	FMA1812A
Multiposition valve	MPV1	Vici	Valco EMT2CSD6MWM
Solenoid valve	V1–V4	SMC	VDW350-6W-2-01N-H-X22-Q
Needle Valve	NV1–NV3	Swagelok	SS-2MG
Gas tanks	High, Middle, Low, Target	Luxfer Gas Cylinders	20 l T-PED cylinders, Type P3056Z
Pressure regulator	RE1–4 (incl. pressure gauges P2–P9)	TESCOM	44-3440KA412-S
Pressure sensor	P1	Keller	PAA-21Y
Stainless steel tubing	ss tube 1/16″	Vici	Vici Jour JR-T-625-40
Stainless steel tubing	ss tube 1/8″	Vici	Vici Jour JR-T-626-00
Flexible tubing	flex tube 1/4″	SERTO	SERTOflex 6.35S
Inlet filter	F1, F2	Solberg	F-15-100
Filter	F3, F4	Swagelok	SS-4TF-40
Filter	F5, F6	Swagelok	SS-4FW-2

Table A.2: Meteorological measurements by MPI-BGC at Ambarchik

Measurand	Manufacturer	Model	Height a.g.l. / location
Wind speed, direction	METEK	uSonic-2	20 m / tower
Air temperature, relative humidity	MELA	KPK1_6-ME-H38 (inside ventilated radiation shield)	20 m and 2 m / tower
Air pressure	SETRA	Type 278	1 m / laboratory

A.2 Derivation of water correction coefficients for Ambarchik

The influence of water vapor on CO_2 and CH_4 measurements was corrected for based on several water correction experiments and a novel water correction model, which we describe in the following paragraphs. For more details, please refer to Reum et al. (2018b).

Experiments were performed with two different humidification methods. For the so-called droplet method, a droplet of de-ionized water (ca. 1 ml) was injected into the dry air stream from a pressurized air tank and measured with the CRDS analyzer. The gradual evaporation of the droplet provided varying water vapor levels. By contrast to the droplet method, the gas washing bottle method was designed to hold water content in the sampled air at stable levels. For this purpose, the air stream from a pressurized tank was humidified by directing it through a gas washing bottle filled with de-ionized water, resulting in an air stream saturated with water vapor. The humid air was mixed with a second, untreated air stream from the same tank. Different water vapor levels were realized by varying the relative flow through the lines using needle valves.

Initial experiments have been performed using the droplet method, but systematic biases in the resulting dry air mole fractions at $H_2O < 0.5$ % led to further experiments with the gas washing bottle method and the development of an improved water correction model:

$$f_c(\boldsymbol{h}) = \underbrace{\boldsymbol{1 + a_c \cdot h + b_c \cdot h^2}}_{\boldsymbol{f_c^{para}(h)}} + \boldsymbol{d_c} \cdot \left(\boldsymbol{e}^{-\frac{\boldsymbol{h}}{\boldsymbol{h_p}}} - \boldsymbol{1}\right) \tag{A.1}$$

Here, $\boldsymbol{f_c^{para}(h)}$ corrects for dilution and pressure broadening (Chen et al., 2010). The parameters d_c and h_p correct for a sensitivity of pressure inside the measurement cavity of Picarro analyzers to water vapor (Reum et al., 2018b).

Three droplet experiments were performed in 2014, while one gas washing bottle experiment was performed in each 2015 and 2017. The droplet method proved unsuitable to derive the pressure-related coefficients $\boldsymbol{d_c}$ and $\boldsymbol{h_p}$ due to fast variations of water vapor, which typically occurred below 0.5 % H_2O (Reum et al., 2018b). Therefore, from the droplet experiments only the data with slowly varying water vapor were used, and $\boldsymbol{d_c}$ and $\boldsymbol{h_p}$ were based only on the gas washing bottle experiments. For each species, a synthesis water correction function was derived by fitting coefficients to the average response of the individual functions (Table A.3).

Table A.3: Synthesis water correction coefficients. Uncertainties are approximated by the maximum difference between the coefficients of the individual water correction functions and the coefficient of synthesis function.

Species	a_c [(% H_2O_{rep})$^{-1}$]	b_c [(% H_2O_{rep})$^{-2}$]	d_c [unitless]	h_p [% H_2O_{rep}]
CO_2	$(-1.2 \pm 0.2) \times 10^{-2}$	$(-2.7 \pm 0.5) \times 10^{-4}$	$(2.2 \pm 1.0) \times 10^{-4}$	0.22 ± 0.12
CH_4	$(-0.97 \pm 0.07)\times 10^{-2}$	$(-3.1 \pm 1.4) \times 10^{-4}$	$(1.1 \pm 0.7) \times 10^{-3}$	0.22 ± 0.12

A.3 Calibration scale and coefficients

Table A.4: Calibrated dry air mole fractions of the air tanks in use at Ambarchik. For a discussion of the uncertainties, see Appendix A.5.

Name	WMO scale X2007 CO_2 [ppm]	WMO scale X2004A CH_4 [ppb]
High Tank	444.67 ± 0.03	2366.95 ± 0.31
Middle Tank	398.68 ± 0.03	1962.39 ± 0.31
Low Tank	354.37 ± 0.03	1796.94 ± 0.31
Target Tank	401.56 ± 0.03	1941.96 ± 0.31

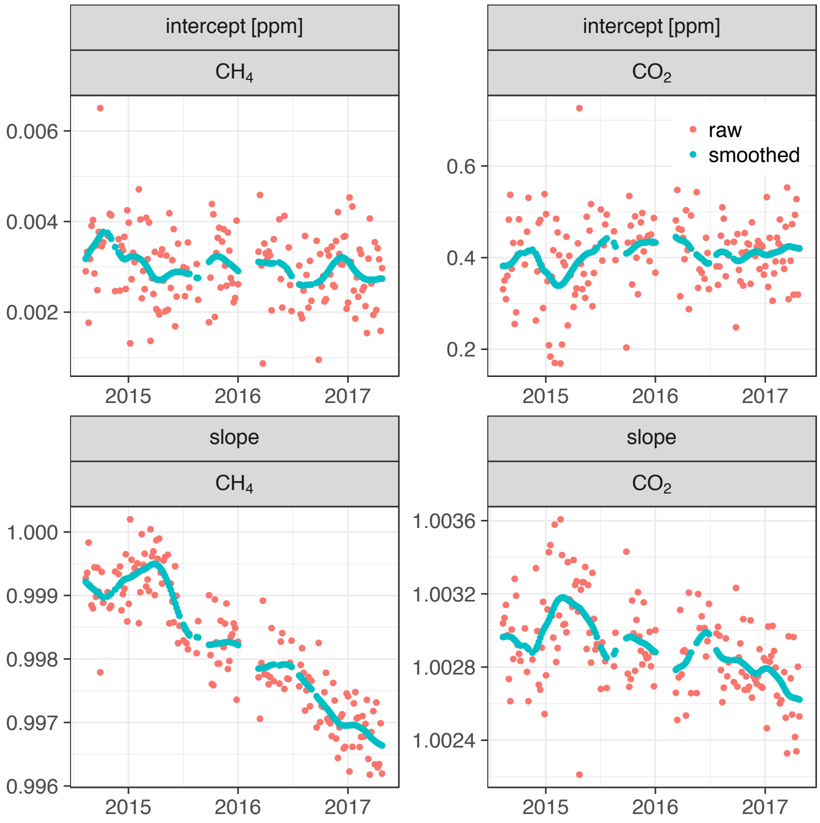

Fig. A.1: Coefficients of linear fits to High, Middle and Low Tank. The smoothed coefficients are used for calibrating data (figure from Reum et al., 2018a).

A.4 Spike detection algorithm for CO_2

The CO_2 spike detection algorithm is a multi-step process. First, candidates for CO_2 spikes are identified. In subsequent steps, false positives are removed. Parts of the algorithm are based on Vickers and Mahrt (1997).

Step 1. Identifying spike candidates based on variation of differences between CO_2 measurements

For this step, data are processed in intervals spanning 1.5 hours. Candidates for CO_2 spikes are identified based on the variability of differences between individual CO_2 measurements. Measurements with differences that exceed 3.5 standard deviations from non-flagged data are flagged as spike candidates. Since flagging the data changes the standard deviation of the non-flagged data, flagging is repeatedly applied until changes between standard deviations of the non-flagged data between the last and second-last loop are less than 10^{-10} ppm CO_2. In cases when all CO_2 data in the interval have rather uniform variations, this procedure flags the whole interval. In that case, all flags are removed, and the interval is considered to have no spikes.

Step 2. Blurring

Around the top of a spike, differences between individual CO_2 soundings are often small and thus, these measurements are not captured as part of a spike in step 1. To unite the ascending and descending parts of spikes, the 20 data points before and after a flagged measurement are flagged. From here on, each group of consecutive flagged measurements is considered a spike candidate.

Step 3. Unflagging individual outliers

Step one often identifies individual or very few consecutive data points as spikes, spanning few seconds. We regard these very small groups of flagged data points as noise misidentified as spikes. After blurring (step 2), these individual outliers form groups of at least 41 data points. In step 3, spike candidates consisting of less than 45 data points are unflagged.

Step 4. Baseline, detrending

For each spike candidate, the baseline is identified as a linear fit to the unflagged measurements within five minutes of any data point of the spike candidate. Using this baseline, the data in this interval are detrended, including the spike candidate.

Step 5. Spike height

From the detrended data from step 4, the maximum deviation from the baseline ("spike height") is calculated. Spike candidates smaller than 8 standard deviations of the baseline measurements are unflagged.

Step 6. Unflagging abrupt but persistent changes

Until the previous step, the algorithm flags abrupt CO_2 changes even if they are persistent. This pattern occurs for example during changes of wind direction and does not constitute an isolated spike. In this case, a trough is present in the detrended spike. The minimum deviation from the baseline is calculated ("trough depth") and compared to the spike height. Since spike height and trough depths can be based on few data points, the influence of noise is strong. To counteract, spike height and trough depth are diminished by two standard deviations of the baseline. Spike candidates with trough depths greater than one fifth of the spike height are unflagged.

Step 7. Unflagging persistent variability changes

The procedure so far can flag the beginning or end of longer periods of larger CO_2 variability. To unflag these false positives, steps 4–5 are applied again with the following changes: (1) a longer baseline of 30 minutes before and after the spike candidate (instead of five minutes) is used, (2) baseline standard deviations are calculated separately for the period before and after the spike candidate, (3) the spike height from step 5 is used instead of recalculated, and (4) the spike height must exceed the maximum of the two baseline standard deviations by a factor of 6 instead of 8.

Step 8. Repeat

The result from steps 4–7 depends on unflagged data points surrounding a spike candidate. Therefore, these steps are repeated until a steady state is reached.

An example of flagged spikes is shown in Fig. A.2. In this example, removing flagged data reduced the hourly averages of Center inlet data between 3 and 4 a.m. by 0.5 ppm (CO_2) and 7.0 ppb (CH_4). No Top inlet data were flagged in this period. Since small spikes can be hard to distinguish from natural signals, some smaller features can pass the algorithm without being flagged that may be classified as spikes upon visual inspection, e.g. at 5:33 a.m. in Fig. A.2. However, given that larger spikes alter hourly averages by values on the order of magnitude of the WMO goals, the impact of these features is likely negligible. In this particular example, removing the detected spikes reduced average CO_2 mole fractions between 5 and 6 a.m. from the Center inlet by 0.07 ppm. Removing the unflagged small spike at 5:33 a.m. would further reduce this average by 0.005 ppm, which is inconsequential.

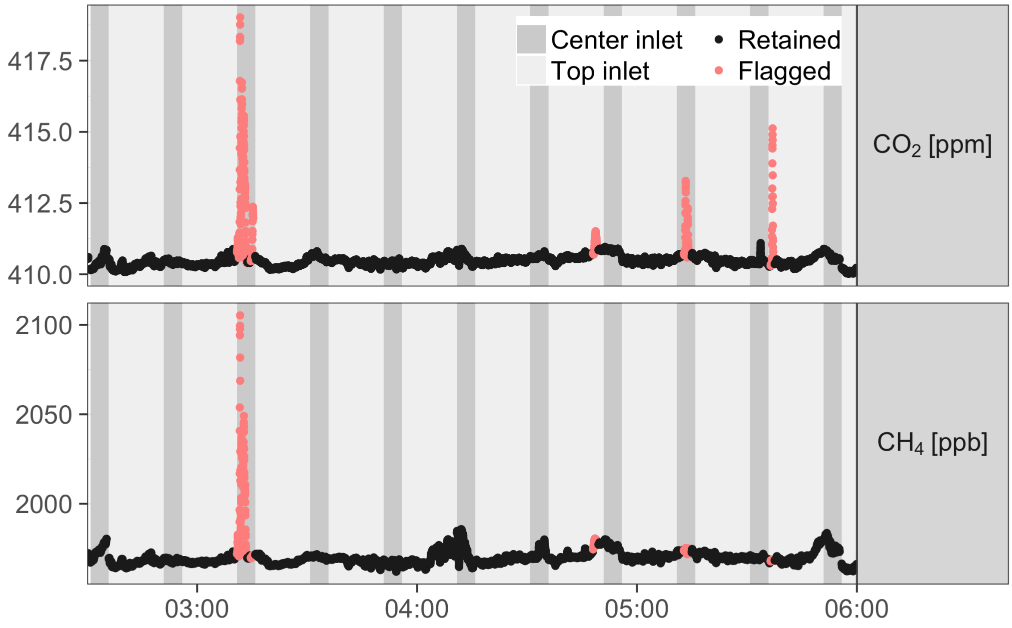

Fig. A.2: Example of a series of flagged CO_2 spikes from December 4, 2016 (figure from Reum et al., 2018a).

A.5 Measurement uncertainties

We adopted the uncertainty quantification method of Andrews et al. (2014). Here, we summarize the main ideas of this approach, the modifications we made, and quantify individual uncertainty components. A detailed description of the nomenclature and method was omitted; please refer to Andrews et al. (2014).

Uncertainty estimation framework by Andrews et al. (2014) and modifications

Andrews et al. (2014) calculated the measurement uncertainty as the largest of four different formulations (Eq. (9a–d) therein). Formulations (a) and (b) were the prediction interval of the linear regression of the calibration tanks, which takes into account the standard error of the fit (se_{fit}) and the uncertainty in the analyzer signal. The difference between (a) and (b) was the estimate of the uncertainty in the analyzer signal. In formulation (a), it was estimated from a model (σ_u) that accounts for analyzer precision (u_p) and drift (u_b), uncertainty of the water vapor correction (u_{wv}), equilibration after switching calibration tanks (u_{eq}) and extrapolation beyond the range covered by the calibration tanks (u_{ex}). In measurement uncertainty formulation (b), the uncertainty estimate of the analyzer signal was estimated from the residuals of the linear fits of the calibration tank mole fractions (σ_y), accounting for the fact that the assigned values of the calibration tanks have non-zero uncertainty (σ_x):

$$\sigma'_y = \sqrt{\sigma_y{}^2 - (m\sigma_x)^2} \tag{A.2}$$

Here, m is the slope of the calibration function. Formulation (c) was the bias of the Target tank (u_{TGT}), and formulation (d) the uncertainty in the assigned values of the calibration tanks (σ_x). In this approach, uncertainty formulations (b), (c) and (d) only accounted for uncertainties of dry air measurements. Hence, we modified it by adding the uncertainty of the water correction to these formulations. Thus, the analyzer precision model for uncertainty formulation (a) became:

$$\sigma_u = \sqrt{u_p{}^2 + u_b{}^2 + u_{eq}{}^2 + u_{ex}{}^2} \tag{A.3}$$

The full uncertainty terms were thus:

$$u_{M,a} = \sqrt{\left(z_{(\alpha,f)}\right)^2 \left(\frac{se_{fit}}{m}\right)^2 + \sigma_u{}^2 + u_{wv}{}^2} \tag{A.4}$$

$$u_{M,b} = \sqrt{\left(z_{(\alpha,f)}\right)^2 \left(\left(\frac{se_{fit}}{m}\right)^2 + \left(\frac{\sigma'_y}{m}\right)^2 \right) + u_{wv}{}^2} \tag{A.5}$$

$$u_{M,c} = \sqrt{u_{TGT}{}^2 + u_{wv}{}^2} \tag{A.6}$$

$$u_{M,d} = \sqrt{\sigma_x{}^2 + u_{wv}{}^2} \tag{A.7}$$

Here, $z_{(\alpha,f)}$ is the quantile function of Student's t distribution. At Ambarchik, three calibration tanks are used to infer linear calibration functions. Thus, for a prediction interval at 1σ-level, $z_{(\alpha=0.675,f=1)} = 1.79$.

Uncertainty components and estimates

In the following paragraphs, the individual components of the four uncertainty estimates Eq. (A.4)–(A.7) are described. For numerical values of the components, see Table A.5. The time-varying uncertainty estimates are shown in Fig. A.3.

Water-vapor (u_{wv})

For the water correction uncertainty u_{wv}, we used the maximum of the difference between individual water correction functions and the synthesis water correction function, i.e. 0.018

% CO_2 and 0.034 % CH_4, regardless of actual water content. This approach likely overestimates u_{wv} at low water vapor content, but was chosen because u_{wv} was not well constrained by the small number of water correction experiments conducted so far.

Assigned values of calibration gas tanks (σ_x)

For the uncertainty of the assigned values of the calibration gas tanks σ_x, we followed the approach by Andrews et al. (2014), who set them to the reproducibility of the primary scales WMO X2007 (CO_2) and WMO X2004 (CH_4). Estimates based on the MPI-BGC implementations of the primary scales yielded smaller uncertainties that underestimated the mismatch between the CO_2 mole fractions of the calibration tanks.

Target tank (u_{TGT})

The uncertainty based on the Target tank measurements u_{TGT} was the same as in Andrews et al. (2014), but with the weighting and window we used for smoothing the calibration coefficients.

Analyzer signal precision model (σ_u)

For the analyzer signal precision model σ_u, analyzer precision (u_p) and drift (u_b) were estimated jointly from variations during a gas tank measurement over 12 days prior to field deployment. The other components (σ_{eq}, σ_{ex}) appeared negligible. In particular, we found no conclusive evidence of non-negligible equilibration errors (σ_{eq}) in our calibrations; however, this remains subject to future research (Appendix A.5). The extrapolation uncertainty (σ_{ex}) applied to only to a small fraction of Ambarchik data, so we ignored this error.

Standard error of fit (se_{fit})

The standard error of the fit was estimated based on individual calibration cycles. This ignores the improvement of the precision achieved by averaging coefficients over multiple cycles. Thus, se_{fit} is overestimated here. Since it is not the dominant source of uncertainty, this error is small.

Table A.5: Measurement uncertainty components. The nomenclature follows Andrews et al. (2014). For time-varying components, averages are reported and denoted with an asterisk (*).

Uncertainty component	CO_2 [ppm]	CH_4 [ppb]
Water correction u_{wv}	* 0.075	* 0.67
Assigned values of calibration gas tanks σ_x	0.03	0.31
Analyzer signal (a) σ_u	0.013	0.25
Analyzer signal (b) σ_y'	* 0.058	* 0.00
Standard error of fit se_{fit}	* 0.047	* 0.11
Target tank deviation from laboratory value u_{TGT}	* 0.038	* 0.32
Maximum of estimates $u_{M,a–d}$	* 0.11	* 0.75

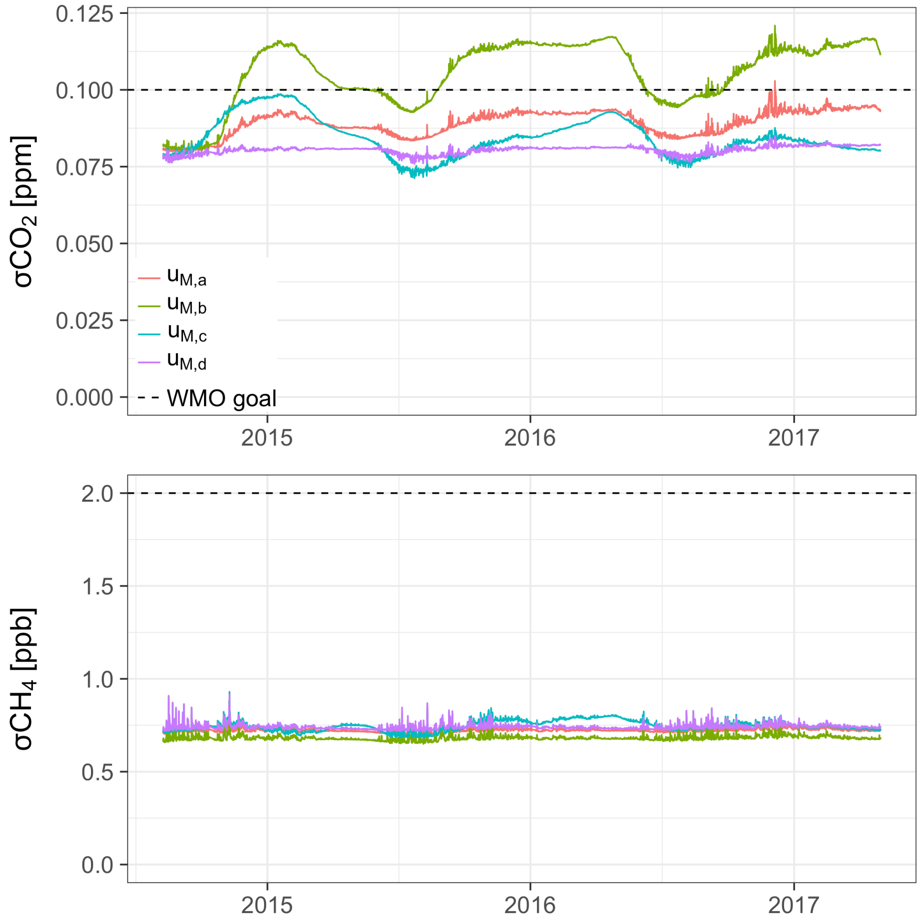

Fig. A.3: Estimates of CO_2 and CH_4 measurement uncertainty as defined in Eq. (A.4)–(A.7). The dashed lines are the WMO inter-laboratory compatibility goals (figure from Reum et al., 2018a).

Potential improvements of the calibration accuracy

Several aspects related to the accuracy of the calibration using regular gas tank measurements are subject to future research. Here, we outline potential calibration errors that could not be conclusively quantified, and how we plan to address them in the future.

To investigate whether the regular probing time of the gas tanks was sufficient for equilibration (e.g. due to flushing of the tubing), we fitted exponential functions to the medians of the regular tank measurements. Deviations between modeled equilibrium mole fractions and the averages used for calibration were negligible ($|\Delta CO_2| < 0.008$ ppm; $|\Delta CH_4| < 0.09$ ppb) and thus ignored. Furthermore, in two experiments, we investigated equilibration error and other drifts (e.g. diffusion in the pressure reducers) by measuring the calibration tanks in reversed order, and in original order for up to two hours. However, the experiments were inconclusive. Based on the available data, we estimated the largest conceivable biases for the ranges 350–450 ppm CO_2 and 1800–2400 ppb CH_4. They were up to 0.06 ppm CO_2 and 0.5 ppb CH_4 at the edges of these ranges and vanished around their centers. More experiments are necessary to assess these possible biases; hence, no bias correction was implemented.

The CO_2 bias of the water-corrected Target tank mole fractions varied from -0.06 to -0.01 ppm (Fig. 4, left). These variations correlated with residual water vapor (which was much smaller than 0.01 %) and temperature in the laboratory during the Target tank measurements, as well as with ambient CO_2 mole fractions sampled before. This suggests that the variations may be due to insufficient flushing during calibration. However, the correlations varied over time without changes to the hardware or probing strategy. Therefore, further investigation of this observation is required, and no correction was implemented.

So far, possible drifts of the gas tanks have not been included in our uncertainty assessment. This will be assessed only when the gas tanks are almost empty, and shipped back to the MPI-BGC for recalibration.

Appendix B Average maps and timeseries of auxiliary variables

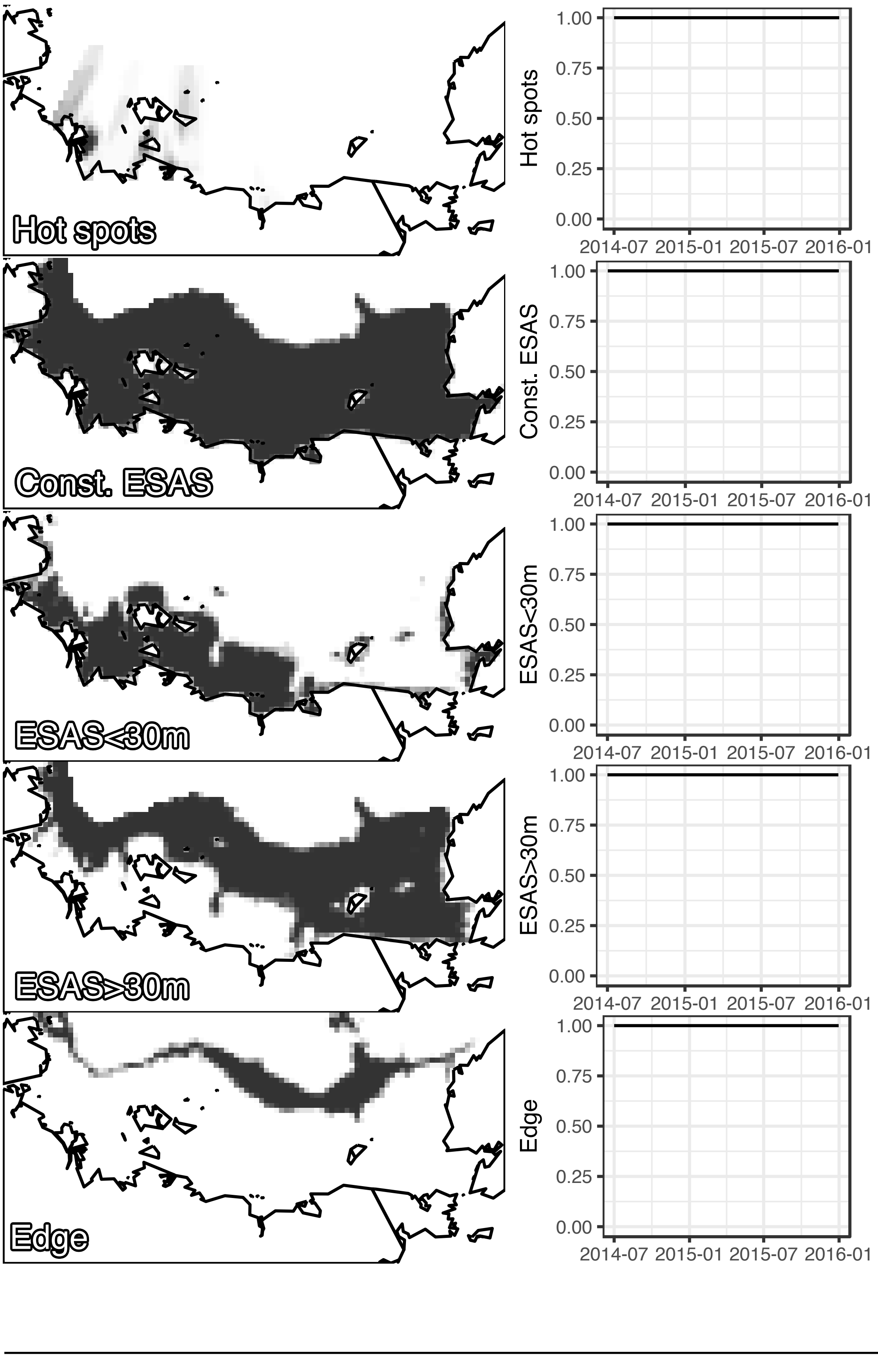

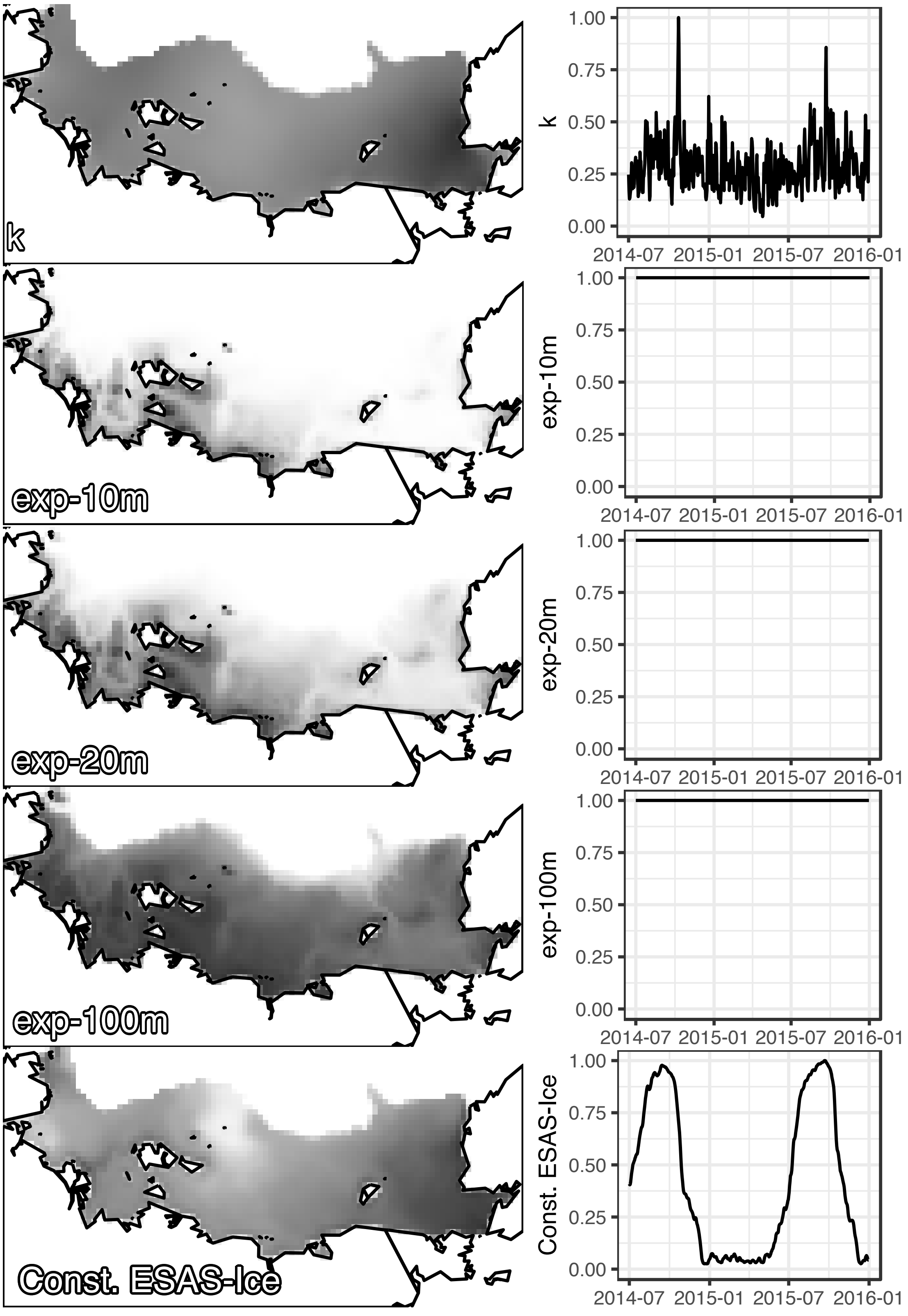
k
exp-10m
exp-20m
exp-100m
Const. ESAS-Ice
1.00
0.75
0.50
0.25
0.00
2014-07
2015-01
2015-07
2016-01

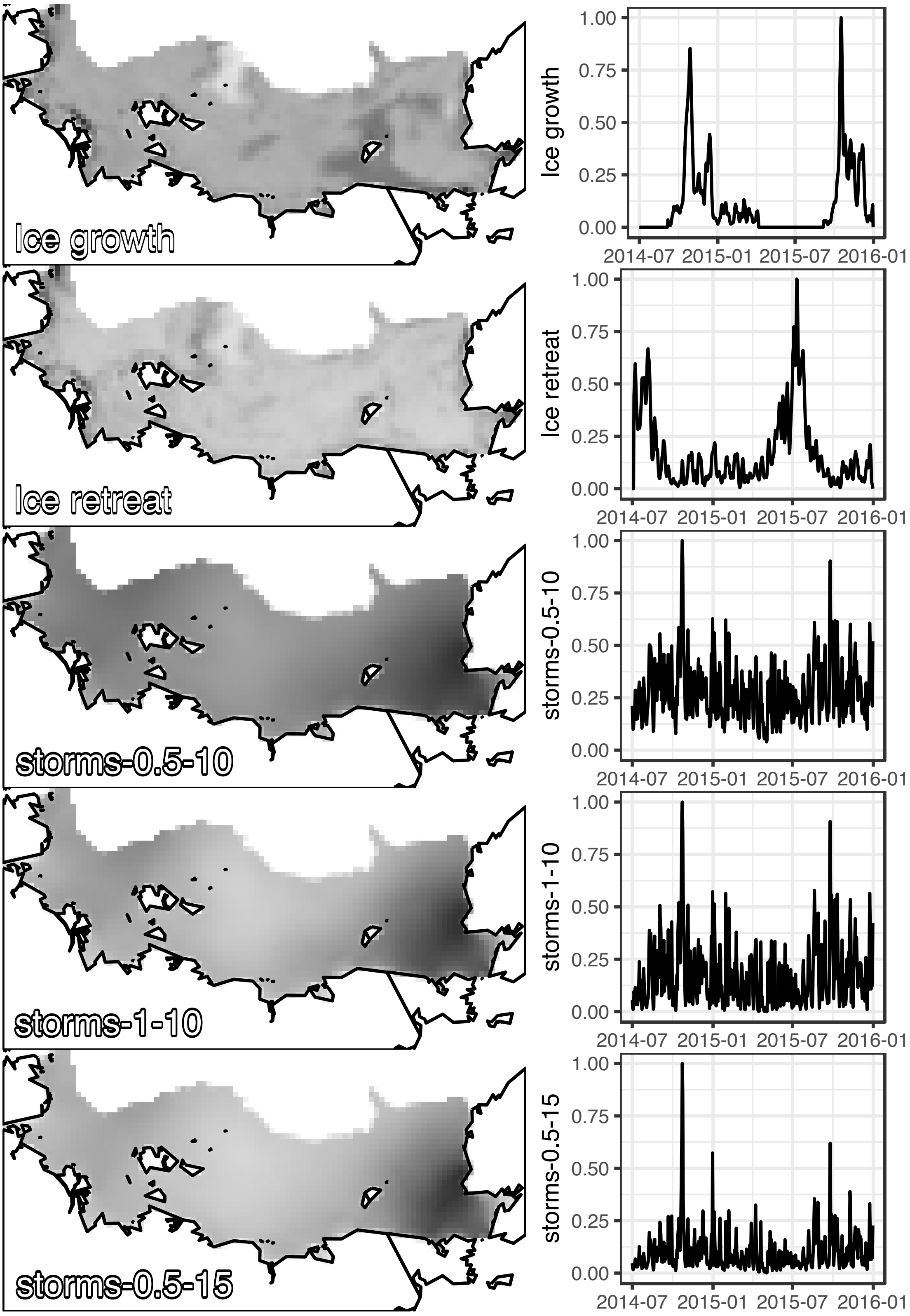
Ice growth
Ice retreat
storms-0.5-10
storms-1-10
storms-0.5-15
1.00
0.75
0.50
0.25
0.00
2014-07
2015-01
2015-07
2016-01

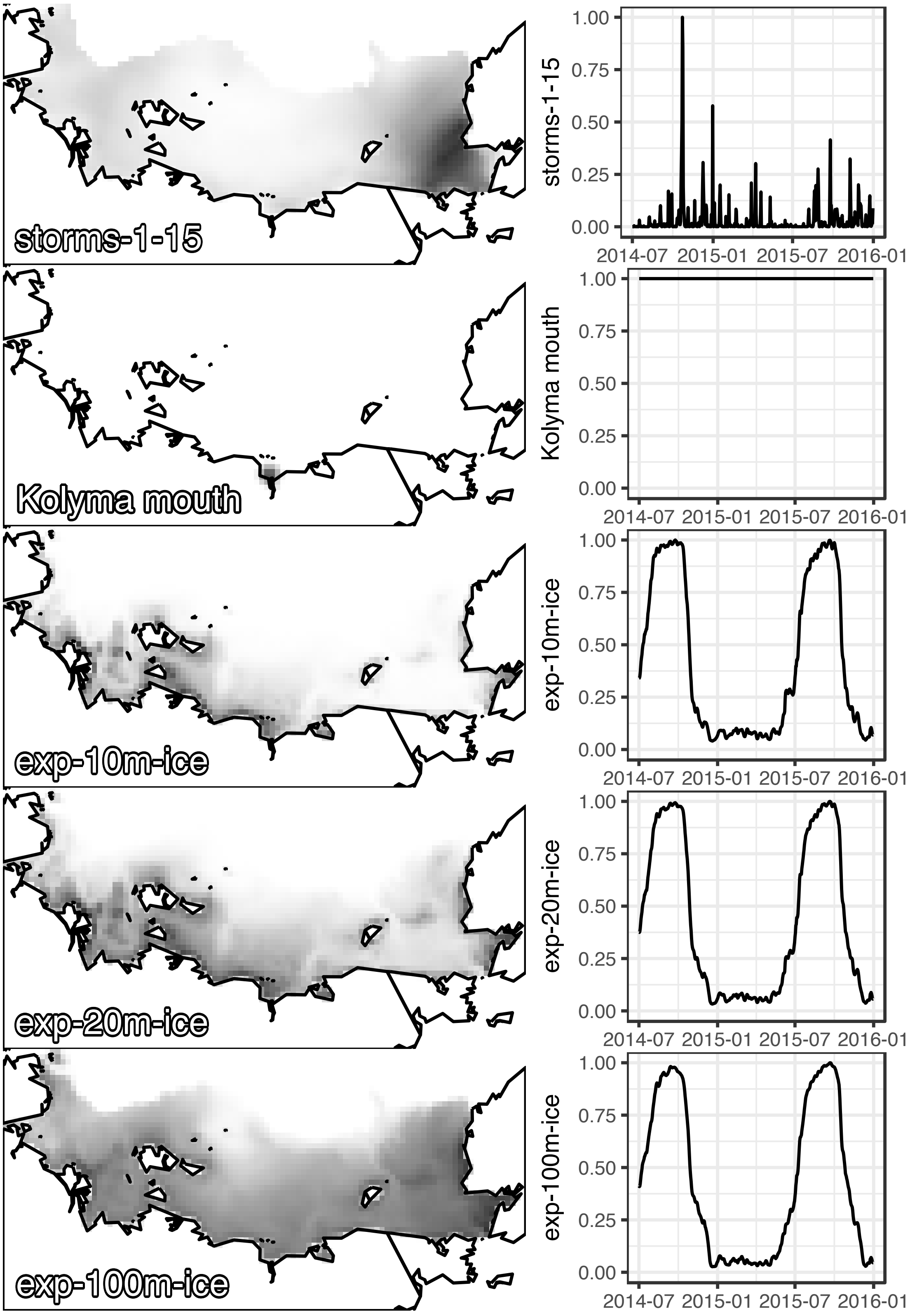
storms-1-15
Kolyma mouth
exp-10m-ice
exp-20m-ice
exp-100m-ice
1.00
0.75
0.50
0.25
0.00
2014-07
2015-01
2015-07
2016-01

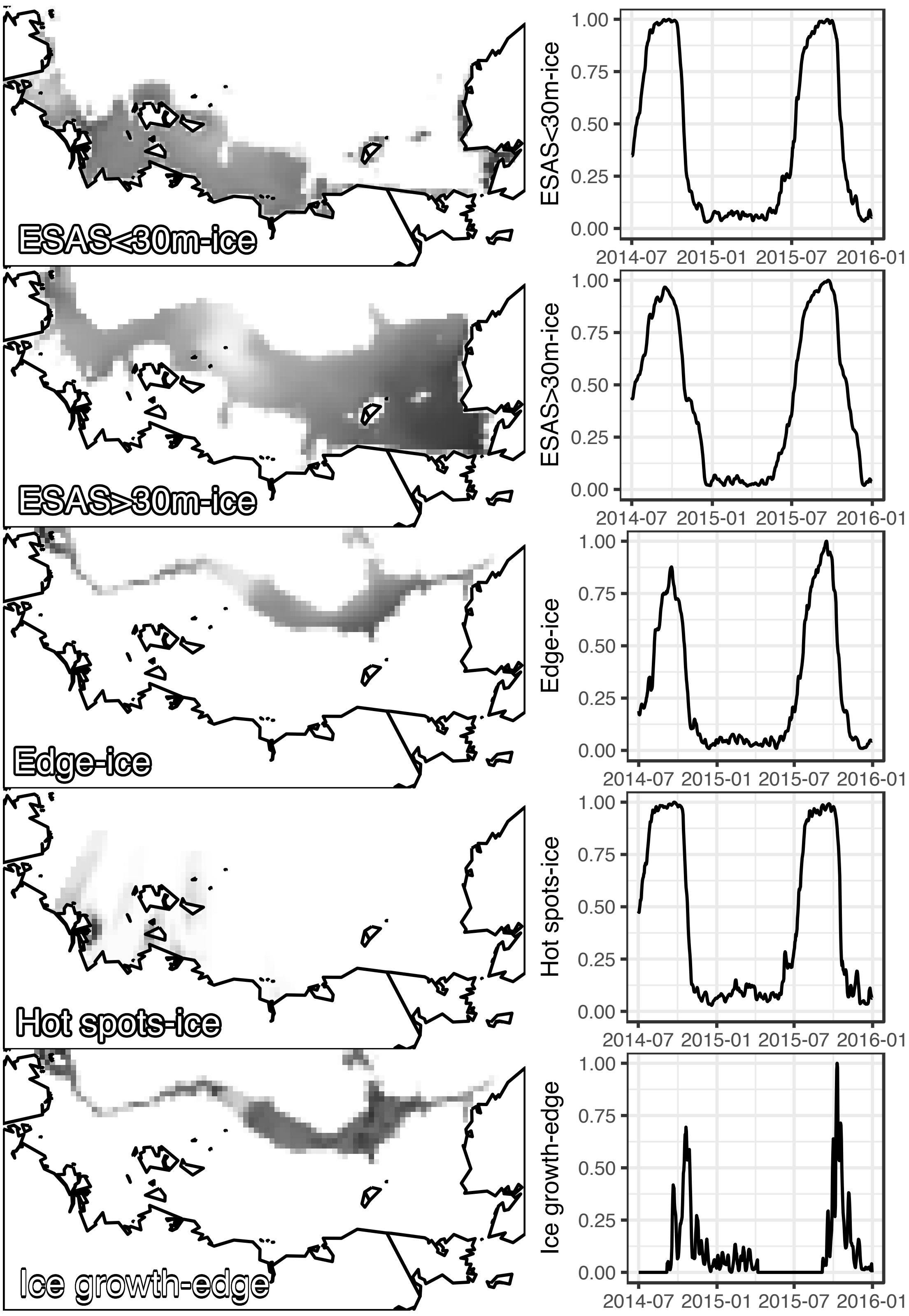
ESAS<30m-ice
ESAS>30m-ice
Edge-ice
Hot spots-ice
Ice growth-edge
ESAS<30m-ice
ESAS>30m-ice
Edge-ice
Hot spots-ice
Ice growth-edge
1.00
0.75
0.50
0.25
0.00
2014-07
2015-01
2015-07
2016-01

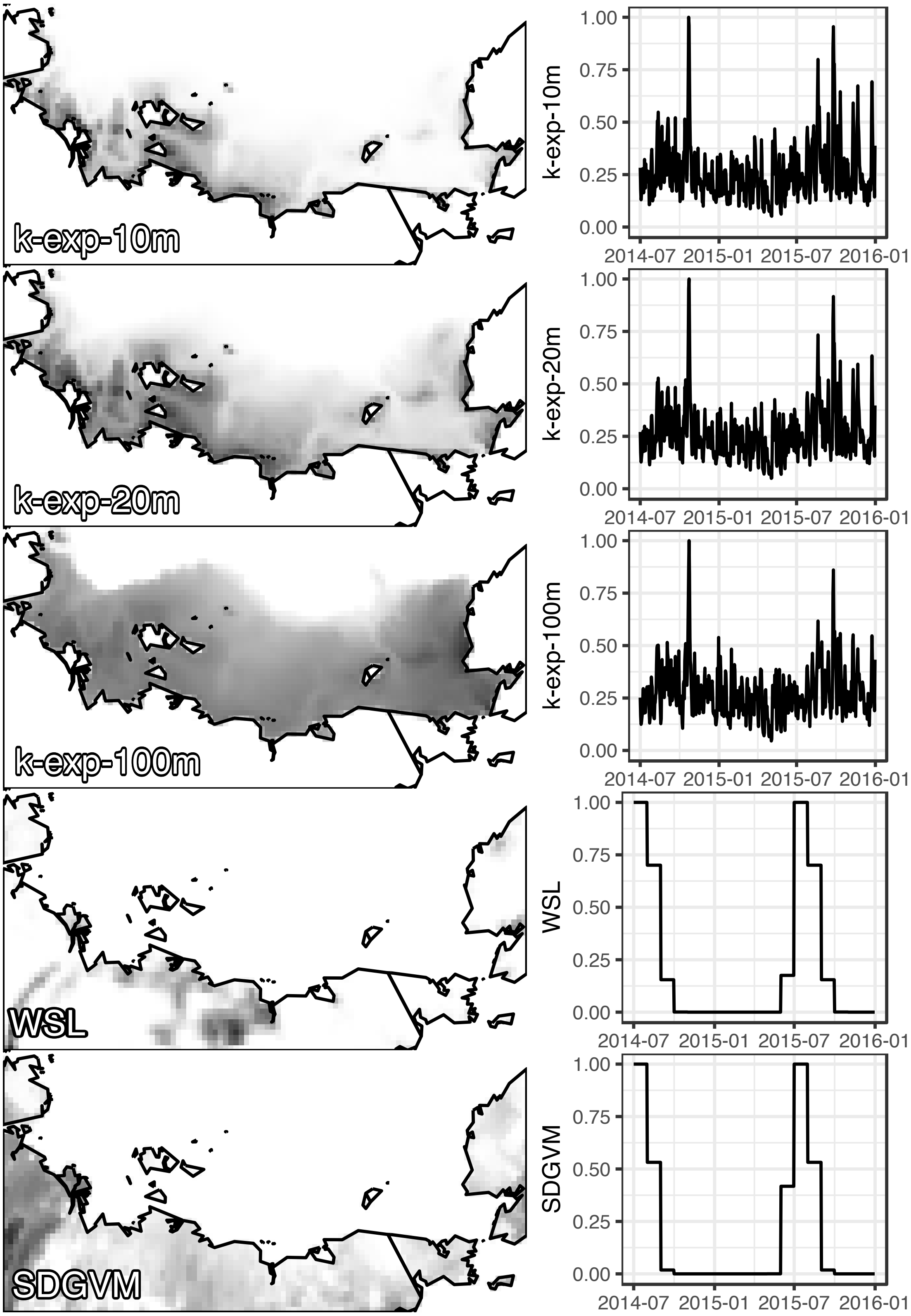
k-exp-10m
k-exp-20m
k-exp-100m
WSL
SDGVM
1.00
0.75
0.50
0.25
0.00
2014-07
2015-01
2015-07
2016-01

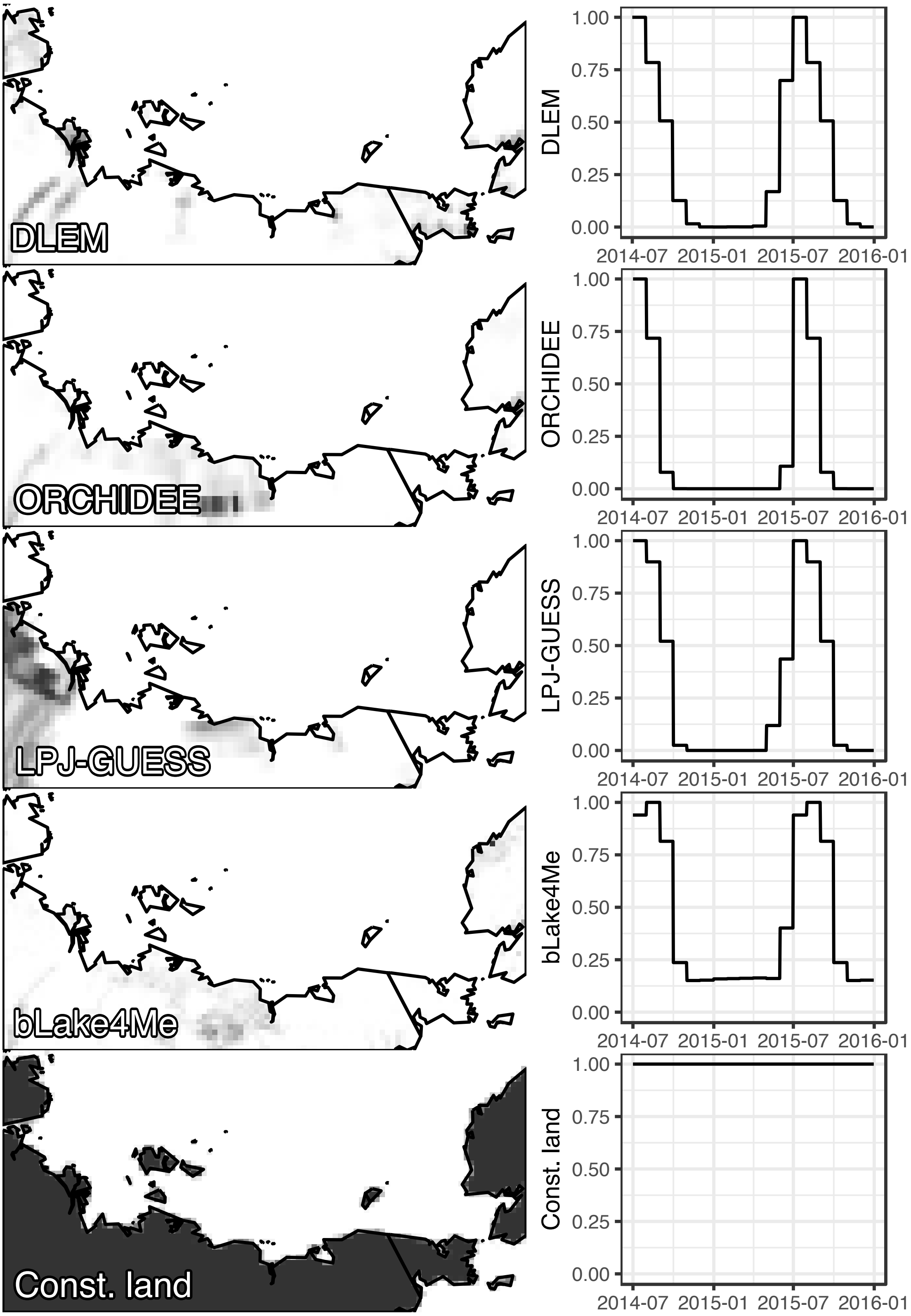
DLEM
ORCHIDEE
LPJ-GUESS
bLake4Me
Const. land
1.00
0.75
0.50
0.25
0.00
2014-07
2015-01
2015-07
2016-01

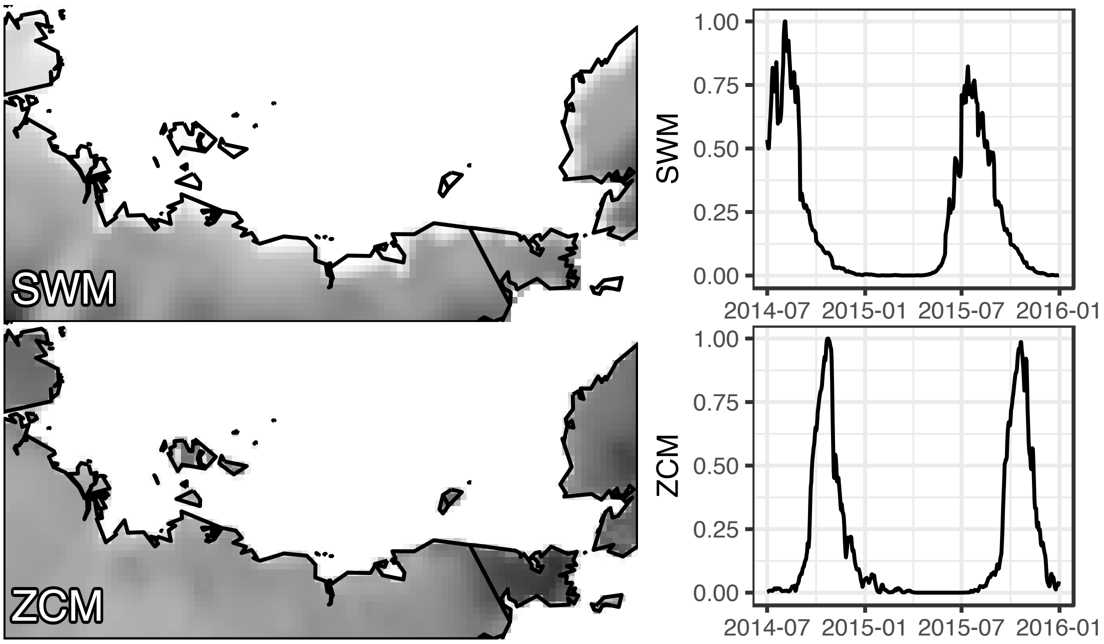

Fig. B.1: Average maps (2014-12-01 – 2015-11-30) and timeseries averaged over the whole domain of all auxiliary variables.

Bibliography

Ainley, D. G., Tynan, C. T. and Stirling, I.: Sea Ice: A Critical Habitat for Polar Marine Mammals and Birds, in Sea Ice: An Introduction to its Physics, Chemistry, Biology and Geology, pp. 240–266, Blackwell, Oxford, UK., 2003.

Anderson, L. G., Björk, G., Jutterström, S., Pipko, I. I., Shakhova, N. E., Semiletov, I. P. and Wåhlström, I.: East Siberian Sea, an Arctic region of very high biogeochemical activity, Biogeosciences, 8(6), 1745–1754, doi:10.5194/bg-8-1745-2011, 2011.

Andreassen, K., Hubbard, A., Winsborrow, M., Patton, H., Vadakkepuliyambatta, S., Plaza-Faverola, A., Gudlaugsson, E., Serov, P., Deryabin, A., Mattingsdal, R., Mienert, J. and Bünz, S.: Massive blow-out craters formed by hydrate-controlled methane expulsion from the Arctic seafloor, Science (80-.)., 356(6341), 948–953, doi:10.1126/science.aal4500, 2017.

Andrews, A. E., Kofler, J. D., Trudeau, M. E., Williams, J. C., Neff, D. H., Masarie, K. A., Chao, D. Y., Kitzis, D., Novelli, P. C., Zhao, C. L., Dlugokencky, E. J., Lang, P. M., Crotwell, M. J., Fischer, M. L., Parker, M. J., Lee, J. T., Baumann, D. D., Desai, A. R., Stanier, C. O., De Wekker, S. F. J., Wolfe, D. E., Munger, J. W. and Tans, P. P.: CO_2, CO, and CH_4 measurements from tall towers in the NOAA earth system research laboratory's global greenhouse gas reference network: Instrumentation, uncertainty analysis, and recommendations for future high-accuracy greenhouse gas, Atmos. Meas. Tech., 7(2), 647–687, doi:10.5194/amt-7-647-2014, 2014.

Archer, D.: A model of the methane cycle, permafrost, and hydrology of the Siberian continental margin, Biogeosciences, 12(10), 2953–2974, doi:10.5194/bg-12-2953-2015, 2015.

Bauch, H. A., Mueller-Lupp, T., Taldenkova, E., Spielhagen, R. F., Kassens, H., Grootes, P. M., Thiede, J., Heinemeier, J. and Petryashov, V. V.: Chronology of the holocene transgression at the north siberian margin, Glob. Planet. Change, 31(1–4), 125–139, doi:10.1016/S0921-8181(01)00116-3, 2001.

Berchet, A., Bousquet, P., Pison, I., Locatelli, R., Chevallier, F., Paris, J.-D., Dlugokencky, E. J., Laurila, T., Hatakka, J., Viisanen, Y., Worthy, D. E. J., Nisbet, E. G., Fisher, R., France, J., Lowry, D., Ivakhov, V. and Hermansen, O.: Atmospheric constraints on the methane emissions from the East Siberian Shelf, Atmos. Chem. Phys., 16(6), 4147–4157, doi:10.5194/acp-16-4147-2016, 2016.

Bigdeli, A., Hara, T., Loose, B. and Nguyen, A. T.: Wave Attenuation and Gas Exchange Velocity in Marginal Sea Ice Zone, J. Geophys. Res. Ocean., 123(3), 2293–2304, doi:10.1002/2017JC013380, 2018.

Bohn, T. J., Melton, J. R., Ito, A., Kleinen, T., Spahni, R., Stocker, B. D., Zhang, B., Zhu, X., Schroeder, R., Glagolev, M. V., Maksyutov, S., Brovkin, V., Chen, G., Denisov, S. N., Eliseev, A. V., Gallego-Sala, A., McDonald, K. C., Rawlins, M. A., Riley, W. J., Subin, Z. M., Tian, H., Zhuang, Q. and Kaplan, J. O.: WETCHIMP-WSL: intercomparison of wetland methane emissions models over West Siberia, Biogeosciences, 12(11), 3321–3349, doi:10.5194/bg-12-3321-2015, 2015.

Bussmann, I.: Distribution of methane in the Lena Delta and Buor-Khaya Bay, Russia, Biogeosciences, 10(7), 4641–4652, doi:10.5194/bg-10-4641-2013, 2013.

Byrd, R. H., Lu, P., Nocedal, J. and Zhu, C.: A Limited Memory Algorithm for Bound Constrained Optimization, SIAM J. Sci. Comput., 16(5), 1190–1208, doi:10.1137/0916069, 1995.

Chadburn, S. E., Krinner, G., Porada, P., Bartsch, A., Beer, C., Belelli Marchesini, L., Boike, J., Ekici, A., Elberling, B., Friborg, T., Hugelius, G., Johansson, M., Kuhry, P., Kutzbach, L., Langer, M., Lund, M., Parmentier, F. J. W., Peng, S., Van Huissteden, K., Wang, T., Westermann, S., Zhu, D. and Burke, E. J.: Carbon stocks and fluxes in the high latitudes: Using site-level data to evaluate Earth system models, Biogeosciences, 14(22), 5143–5169, doi:10.5194/bg-14-5143-2017, 2017.

Charkin, A. N., Dudarev, O. V., Semiletov, I. P., Kruhmalev, A. V., Vonk, J. E., Sánchez-García, L., Karlsson, E. and Gustafsson, O.: Seasonal and interannual variability of sedimentation and organic matter distribution in the Buor-Khaya Gulf: The primary recipient of input from Lena River and coastal erosion in the southeast Laptev Sea, Biogeosciences, 8(9), 2581–2594, doi:10.5194/bg-8-2581-2011, 2011.

Chen, H., Winderlich, J., Gerbig, C., Hoefer, A., Rella, C. W., Crosson, E. R., Van Pelt, A. D., Steinbach, J., Kolle, O., Beck, V., Daube, B. C., Gottlieb, E. W., Chow, V. Y., Santoni, G. W. and Wofsy, S. C.: High-accuracy continuous airborne measurements of greenhouse gases (CO_2 and CH_4) using the cavity ring-down spectroscopy (CRDS) technique, Atmos. Meas. Tech., 3(2), 375–386, doi:10.5194/amt-3-375-2010, 2010.

Chevallier, F., Viovy, N., Reichstein, M. and Ciais, P.: On the assignment of prior errors in Bayesian inversions of CO_2 surface fluxes, Geophys. Res. Lett., 33(13), 1–5, doi:10.1029/2006GL026496, 2006.

Chevallier, F., Wang, T., Ciais, P., Maignan, F., Bocquet, M., Altaf Arain, M., Cescatti, A., Chen, J., Dolman, A. J., Law, B. E., Margolis, H. a., Montagnani, L. and Moors, E. J.: What eddy-covariance measurements tell us about prior land flux errors in CO_2-flux inversion schemes, Global Biogeochem. Cycles, 26(1), 1–9, doi:10.1029/2010GB003974, 2012.

Cicerone, R. J. and Oremland, R. S.: Biogeochemical aspects of atmospheric methane, Global Biogeochem. Cycles, 2(4), 299–327, doi:10.1029/GB002i004p00299, 1988.

Crabeck, O., Delille, B., Rysgaard, S., Thomas, D. N., Geilfus, N.-X., Else, B. and Tison, J.-L.: First "in situ" determination of gas transport coefficients (D_{O2}, D_{Ar}, and D_{N2}) from bulk gas concentration measurements (O_2 , N_2, Ar) in natural sea ice, J. Geophys. Res. Ocean., 119(10), 6655–6668, doi:10.1002/2014JC009849, 2014.

Cramer, B. and Franke, D.: Indications for an active petroleum system in the Laptev Sea, NE Siberia, J. Pet. Geol., 28(4), 369–384, doi:10.1111/j.1747-5457.2005.tb00088.x, 2005.

Dallimore, S. R. and Collett, T. S.: Intrapermafrost gas hydrates from a deep core hole in the Mackenzie Delta, Northwest Territories, Canada, Geology, 23(6), 527, doi:10.1130/0091-7613(1995)023<0527:IGHFAD>2.3.CO;2, 1995.

Damm, E., Schauer, U., Rudels, B. and Haas, C.: Excess of bottom-released methane in an Arctic shelf sea polynya in winter, Cont. Shelf Res., 27(12), 1692–1701, doi:10.1016/j.csr.2007.02.003, 2007.

Damm, E., Kiene, R. P., Schwarz, J., Falck, E. and Dieckmann, G.: Methane cycling in Arctic shelf water and its relationship with phytoplankton biomass and DMSP, Mar. Chem., 109(1–2), 45–59, doi:10.1016/j.marchem.2007.12.003, 2008.

Damm, E., Helmke, E., Thoms, S., Schauer, U., Nöthig, E., Bakker, K. and Kiene, R. P.: Methane production in aerobic oligotrophic surface water in the central Arctic Ocean, Biogeosciences, 7(3), 1099–1108, doi:10.5194/bg-7-1099-2010, 2010.

Damm, E., Rudels, B., Schauer, U., Mau, S. and Dieckmann, G.: Methane excess in Arctic surface water- triggered by sea ice formation and melting, Sci. Rep., 5, 16179, doi:10.1038/srep16179, 2015a.

Damm, E., Thoms, S., Beszczynska-Möller, A., Nöthig, E. M. and Kattner, G.: Methane excess production in oxygen-rich polar water and a model of cellular conditions for this paradox, Polar Sci., 9(3), 327–334, doi:10.1016/j.polar.2015.05.001, 2015b.

Damm, E., Bauch, D., Krumpen, T., Rabe, B., Korhonen, M., Vinogradova, E. and Uhlig, C.: The Transpolar Drift conveys methane from the Siberian Shelf to the central Arctic Ocean, Sci. Rep., 8(1), 1–10, doi:10.1038/s41598-018-22801-z, 2018.

Danielson, J. J. and Gesch, D. B.: Global Multi-resolution Terrain Elevation Data 2010 (GMTED2010), U.S. Geol. Surv. Open-File Rep. 2011–1073, 2010, 26, 2011.

Dee, D. P., Uppala, S. M., Simmons, A. J., Berrisford, P., Poli, P., Kobayashi, S., Andrae, U., Balmaseda, M. A., Balsamo, G., Bauer, P., Bechtold, P., Beljaars, A. C. M., van de Berg, L., Bidlot, J., Bormann, N., Delsol, C., Dragani, R., Fuentes, M., Geer, A. J., Haimberger, L., Healy, S. B., Hersbach, H., Hólm, E. V., Isaksen, L., Kållberg, P., Köhler, M., Matricardi, M., Mcnally, A. P., Monge-Sanz, B. M., Morcrette, J. J., Park, B. K., Peubey, C., de Rosnay, P., Tavolato, C., Thépaut, J. N. and Vitart, F.: The ERA-Interim reanalysis: Configuration and performance of the data assimilation system, Q. J. R. Meteorol. Soc., 137(656), 553–597, doi:10.1002/qj.828, 2011.

Deike, L. and Melville, W. K.: Gas Transfer by Breaking Waves, Geophys. Res. Lett., doi:10.1029/2018GL078758, 2018.

Delisle, G.: Temporal variability of subsea Permafrost and gas hydrate occurrences as function of climate change in the Laptev Sea, Siberia, Polarforschung, 68, 221–225 [online] Available from: http://epic.awi.de/28436/1/Polarforsch1998_27.pdf (Accessed 29 August 2014), 2000.

DelSontro, T., McGinnis, D. F., Wehrli, B. and Ostrovsky, I.: Size does matter: Importance of large bubbles and small-scale hot spots for methane transport, Environ. Sci. Technol., 49(3), 1268–1276, doi:10.1021/es5054286, 2015.

Dlugokencky, E. J., Steele, P., Lang, P. M. and Masarie, K. A.: Atmospheric methane at Mauna Loa and Barrow observatories: Presentation and analysis of in situ measurements, J. Geophys. Res., 100(D11), 23103, doi:10.1029/95JD02460, 1995.

Dmitrenko, I., Tyshko, K., Kirillov, S., Eicken, H., Holemann, J. and Kassens, H.: Impact of flaw polynyas on the hydrography of the Laptev Sea, Glob. Planet. Change, 48(1–3), 9–27, doi:10.1016/j.gloplacha.2004.12.016, 2005.

Dmitrenko, I. A., Kirillov, S. A., Tremblay, L. B., Kassens, H., Anisimov, O. A., Lavrov, S. A., Razumov, S. O. and Grigoriev, M. N.: Recent changes in shelf hydrography in the Siberian Arctic: Potential for subsea permafrost instability, J. Geophys. Res., 116(C10), C10027, doi:10.1029/2011JC007218, 2011.

Eicken, H.: From the Microscopic, to the Macroscopic, to the Regional Scale: Growth, Microstructure and Properties of Sea Ice, in Sea Ice: An Introduction to its Physics, Chemistry, Biology and Geology, edited by D. N. Thomas and G. S. Dieckmann, pp. 22–83, Blackwell, Oxford, UK., 2003.

Else, B. G. T., Papakyriakou, T. N., Galley, R. J., Drennan, W. M., Miller, L. A. and Thomas, H.: Wintertime CO $_2$ fluxes in an Arctic polynya using eddy covariance: Evidence for enhanced air-sea gas transfer during ice formation, J. Geophys. Res., 116, C00G03, doi:10.1029/2010JC006760, 2011.

Etiope, G.: Natural Gas Seepage, Springer International Publishing, Cham., 2015.

Evenden, G. I.: Cartographic Projection Procedures for the UNIX Environment - A User's Manual., 1990.

Fenwick, L., Capelle, D., Damm, E., Zimmermann, S., Williams, W. J., Vagle, S. and Tortell, P. D.: Methane and nitrous oxide distributions across the North American Arctic Ocean during summer, 2015, J. Geophys. Res. Ocean., 122(1), 390–412, doi:10.1002/2016JC012493, 2017.

Frederick, J. M. and Buffett, B. A.: Taliks in relict submarine permafrost and methane hydrate deposits: Pathways for gas escape under present and future conditions, J. Geophys. Res. Earth Surf., 119(2), 106–122, doi:10.1002/2013JF002987, 2014.

Gornitz, V. and Fung, I. Y.: Potential distribution of methane hydrates in the world's oceans, Global Biogeochem. Cycles, 8(3), 335–347, doi:10.1029/94GB00766, 1994.

He, X., Sun, L., Xie, Z., Huang, W., Long, N., Li, Z. and Xing, G.: Sea ice in the Arctic Ocean: Role of shielding and consumption of methane, Atmos. Environ., 67, 8–13, doi:10.1016/j.atmosenv.2012.10.029, 2013.

Henderson, J. M., Eluszkiewicz, J., Mountain, M. E., Nehrkorn, T., Chang, R. Y.-W., Karion, A., Miller, J. B., Sweeney, C., Steiner, N., Wofsy, S. C. and Miller, C. E.: Atmospheric transport simulations in support of the Carbon in Arctic Reservoirs Vulnerability Experiment (CARVE), Atmos. Chem. Phys., 15(8), 4093–4116, doi:10.5194/acp-15-4093-2015, 2015.

Hugelius, G., Strauss, J., Zubrzycki, S., Harden, J. W., Schuur, E. A. G., Ping, C. L., Schirrmeister, L., Grosse, G., Michaelson, G. J., Koven, C. D., O'Donnell, J. A., Elberling, B., Mishra, U., Camill, P., Yu, Z., Palmtag, J. and Kuhry, P.: Estimated stocks of circumpolar permafrost carbon with quantified uncertainty ranges and identified data gaps, Biogeosciences, 11(23), 6573–6593, doi:10.5194/bg-11-6573-2014, 2014.

IPCC: Climate Change 2013. The Physical Science Basis. Working Group 1 Contribution to the Fifth Assessment Report of the Intergovernmental Panel on Climate Change., 2013.

James, G., Witten, D., Hastie, T. and Tibshirani, R.: An Introduction to Statistical Learning, Springer., 2013.

James, R. H., Bousquet, P., Bussmann, I., Haeckel, M., Kipfer, R., Leifer, I., Niemann, H., Ostrovsky, I., Piskozub, J., Rehder, G., Treude, T., Vielstädte, L. and Greinert, J.: Effects of climate change on methane emissions from seafloor sediments in the Arctic Ocean: A review, Limnol. Oceanogr., 61(S1), S283–S299, doi:10.1002/lno.10307, 2016.

Janout, M., Hölemann, J., Juhls, B., Krumpen, T., Rabe, B., Bauch, D., Wegner, C., Kassens, H. and Timokhov, L.: Episodic warming of near-bottom waters under the Arctic sea ice on the central Laptev Sea shelf, Geophys. Res. Lett., 43(1), 264–272, doi:10.1002/2015GL066565, 2016.

Janout, M. A., Hölemann, J., Timokhov, L., Gutjahr, O. and Heinemann, G.: Circulation in the northwest Laptev Sea in the eastern Arctic Ocean: Crossroads between Siberian River water, Atlantic water and polynya-formed dense water, J. Geophys. Res. Ocean., 122(8), 6630–6647, doi:10.1002/2017JC013159, 2017.

Jeffreys, H.: The Theory of Probability, 3rd ed., Oxford University Press, Oxford., 1961.

Judd, A. G.: The global importance and context of methane escape from the seabed, Geo-Marine Lett., 23(3–4), 147–154, doi:10.1007/s00367-003-0136-z, 2003.

Kaleschke, L., Lüpkes, C., Vihma, T., Haarpaintner, J., Bochert, A., Hartmann, J. and Heygster, G.: SSM/I Sea Ice Remote Sensing for Mesoscale Ocean-Atmosphere Interaction Analysis, Can. J. Remote Sens., 27(5), 526–537, doi:10.1080/07038992.2001.10854892, 2001.

Kaplan, J. O.: Wetlands at the Last Glacial Maximum: Distribution and methane emissions, Geophys. Res. Lett., 29(6), 3–6, doi:10.1029/2001GL013366, 2002.

Karion, A., Lauvaux, T., Coto, I. L., Sweeney, C., Mueller, K. L., Gourdji, S., Angevine, W., Barkley, Z., Deng, A., Andrews, A., Stein, A., Whetstone, J., Office, S. P., Oceanic, N. and Insights, U.: Inter-comparison of Atmospheric Trace Gas Dispersion Models : Barnett Shale Case Study, , (November), 1–29, 2018.

Kass, R. and Raftery, A.: Bayes Factors, J. Am. Stat. Assoc., 90(430), 773–795, doi:10.1080/01621459.1995.10476572, 1995.

Kelley, J. J. and Gosink, T. A.: Gases in the sea-ice. Final report to the ONR (N000 14-76C-0331)., 1979.

Kern, S., Kaleschke, L. and Spreen, G.: Climatology of the Nordic (Irminger, Greenland, Barents, Kara and White/Pechora) Seas ice cover based on 85 GHz satellite microwave radiometry: 1992-2008, Tellus A, 62(4), 411–434, doi:10.1111/j.1600-0870.2010.00457.x, 2010.

Kilpeläinen, T., Vihma, T., Manninen, M., Sjöblom, A., Jakobson, E., Palo, T. and Maturilli, M.: Modelling the vertical structure of the atmospheric boundary layer over Arctic fjords in Svalbard, Q. J. R. Meteorol. Soc., 138(668), 1867–1883, doi:10.1002/qj.1914, 2012.

Kirschke, S., Bousquet, P., Ciais, P., Saunois, M., Canadell, J. G., Dlugokencky, E. J., Bergamaschi, P., Bergmann, D., Blake, D. R., Bruhwiler, L., Cameron-Smith, P., Castaldi, S., Chevallier, F., Feng, L., Fraser, A., Heimann, M., Hodson, E. L., Houweling, S., Josse, B., Fraser, P. J., Krummel, P. B., Lamarque, J.-F., Langenfelds, R. L., Le Quéré, C., Naik, V., O'Doherty, S., Palmer, P. I., Pison, I., Plummer, D., Poulter, B., Prinn, R. G., Rigby, M., Ringeval, B., Santini, M., Schmidt, M., Shindell, D. T., Simpson, I. J., Spahni, R., Steele, P., Strode, S. A., Sudo, K., Szopa, S., van der Werf, G. R., Voulgarakis, A., van Weele, M., Weiss, R. F., Williams, J. E. and Zeng, G.: Three decades of global methane sources and sinks, Nat. Geosci., 6(10), 813–823, doi:10.1038/ngeo1955, 2013.

Kitanidis, P. K.: Introduction to Geostatistics, Cambridge University Press, Cambridge., 1997.

Kitidis, V., Upstill-Goddard, R. C. and Anderson, L. G.: Methane and nitrous oxide in surface water along the North-West Passage, Arctic Ocean, Mar. Chem., 121(1–4), 80–86, doi:10.1016/j.marchem.2010.03.006, 2010.

Kittler, F., Heimann, M., Kolle, O., Zimov, N., Zimov, S. A. and Göckede, M.: Long-Term Drainage Reduces CO_2 Uptake and CH_4 Emissions in a Siberian Permafrost Ecosystem, Global Biogeochem. Cycles, 31(12), 1704–1717, doi:10.1002/2017GB005774, 2017.

Koch, K., Knoblauch, C. and Wagner, D.: Methanogenic community composition and anaerobic carbon turnover in submarine permafrost sediments of the Siberian Laptev Sea, Environ. Microbiol., 11(3), 657–668, doi:10.1111/j.1462-2920.2008.01836.x, 2009.

Kort, E. A., Wofsy, S. C., Daube, B. C., Diao, M., Elkins, J. W., Gao, R. S., Hintsa, E. J., Hurst, D. F., Jimenez, R., Moore, F. L., Spackman, J. R. and Zondlo, M. A.: Atmospheric observations of Arctic Ocean methane emissions up to 82° north, Nat. Geosci., 5(5), 318–321, doi:10.1038/ngeo1452, 2012.

Kountouris, P., Gerbig, C., Totsche, K.-U., Dolman, A. J., Meesters, A. G. C. A., Broquet, G., Maignan, F., Gioli, B., Montagnani, L. and Helfter, C.: An objective prior error quantification for regional atmospheric inverse applications, Biogeosciences, 12(24), 7403–7421, doi:10.5194/bg-12-7403-2015, 2015.

Kvenvolden, K. A., Lilley, M. D., Lorenson, T. D., Barnes, P. W. and McLaughlin, E.: The Beaufort Sea continental shelf as a seasonal source of atmospheric methane, Geophys. Res. Lett., 20(22), 2459–2462, doi:10.1029/93GL02727, 1993.

Leifer, I. and Patro, R. K.: The bubble mechanism for methane transport from the shallow sea bed to the surface: A review and sensitivity study, Cont. Shelf Res., 22(16), 2409–2428, doi:10.1016/S0278-4343(02)00065-1, 2002.

Leifer, I., Luyendyk, B. P., Boles, J. and Clark, J. F.: Natural marine seepage blowout: Contribution to atmospheric methane, Global Biogeochem. Cycles, 20(3), doi:10.1029/2005GB002668, 2006.

Lenton, T. M., Held, H., Kriegler, E., Hall, J. W., Lucht, W., Rahmstorf, S. and Schellnhuber, H. J.: Tipping elements in the Earth’s climate system, Proc. Natl. Acad. Sci., 105(6), 1786–1793, doi:10.1073/pnas.0705414105, 2008.

Li, Y., Zhan, L., Zhang, J., Chen, L., Chen, J. and Zhuang, Y.: A significant methane source over the Chukchi Sea shelf and its sources, Cont. Shelf Res., 148(July), 150–158, doi:10.1016/j.csr.2017.08.019, 2017.

Lin, J. C., Gerbig, C., Wofsy, S. C., Andrews, A. E., Daube, B. C., Davis, K. J. and Grainger, C. A.: A near-field tool for simulating the upstream influence of atmospheric observations: The Stochastic Time-Inverted Lagrangian Transport (STILT) model, J. Geophys. Res., 108(D16), 4493, doi:10.1029/2002JD003161, 2003.

Liu, H., Zhang, Q., Katul, G. G., Cole, J. J., Chapin, F. S. and MacIntyre, S.: Large CO_2 effluxes at night and during synoptic weather events significantly contribute to CO_2 emissions from a reservoir, Environ. Res. Lett., 11(6), 064001, doi:10.1088/1748-9326/11/6/064001, 2016.

Loose, B., Schlosser, P., Perovich, D., Ringelberg, D., Ho, D. T., Takahashi, T., Richter-Menge, J., Reynolds, C. M., Mcgillis, W. R. and Tison, J. L.: Gas diffusion through columnar laboratory sea ice: Implications for mixed-layer ventilation of CO2 in the seasonal ice zone, Tellus, Ser. B Chem. Phys. Meteorol., 63(1), 23–39, doi:10.1111/j.1600-0889.2010.00506.x, 2011.

Lovely, A., Loose, B., Schlosser, P., McGillis, W., Zappa, C., Perovich, D., Brown, S., Morell, T., Hsueh, D. and Friedrich, R.: The Gas Transfer through Polar Sea ice experiment: Insights into the rates and pathways that determine geochemical fluxes, J. Geophys. Res. Ocean., 120(12), 8177–8194, doi:10.1002/2014JC010607, 2015.

Lowry, K. E., Pickart, R. S., Selz, V., Mills, M. M., Pacini, A., Lewis, K. M., Joy-Warren, H. L., Nobre, C., van Dijken, G. L., Grondin, P.-L., Ferland, J. and Arrigo, K. R.: Under-Ice

Phytoplankton Blooms Inhibited by Spring Convective Mixing in Refreezing Leads, J. Geophys. Res. Ocean., 90–109, doi:10.1002/2016JC012575, 2018.

Mastepanov, M., Sigsgaard, C., Tagesson, T., Ström, L., Tamstorf, M. P., Lund, M. and Christensen, T. R.: Revisiting factors controlling methane emissions from high-Arctic tundra, Biogeosciences, 10(11), 5139–5158, doi:10.5194/bg-10-5139-2013, 2013.

Matveeva, T., Savvichev, A., Semenova, A., Logvina, E., Kolesnik, A. and Bosin, A.: Source, Origin, and Spatial Distribution of Shallow Sediment Methane in the Chukchi Sea, Oceanography, 28(3), 202–217, doi:10.5670/oceanog.2015.66, 2015.

Mau, S., Römer, M., Torres, M. E., Bussmann, I., Pape, T., Damm, E., Geprägs, P., Wintersteller, P., Hsu, C. W., Loher, M. and Bohrmann, G.: Widespread methane seepage along the continental margin off Svalbard-from Bjørnøya to Kongsfjorden, Sci. Rep., 7(June 2016), 1–13, doi:10.1038/srep42997, 2017.

McGinnis, D. F., Greinert, J., Artemov, Y., Beaubien, S. E. and Wüest, A.: Fate of rising methane bubbles in stratified waters: How much methane reaches the atmosphere?, J. Geophys. Res. Ocean., 111(9), 1–15, doi:10.1029/2005JC003183, 2006.

Melton, J. R., Wania, R., Hodson, E. L., Poulter, B., Ringeval, B., Spahni, R., Bohn, T. J., Avis, C. a., Beerling, D. J., Chen, G., Eliseev, A. V., Denisov, S. N., Hopcroft, P. O., Lettenmaier, D. P., Riley, W. J., Singarayer, J. S., Subin, Z. M., Tian, H., Zürcher, S., Brovkin, V., van Bodegom, P. M., Kleinen, T., Yu, Z. C. and Kaplan, J. O.: Present state of global wetland extent and wetland methane modelling: conclusions from a model inter-comparison project (WETCHIMP), Biogeosciences, 10(2), 753–788, doi:10.5194/bg-10-753-2013, 2013.

Michalak, A. M., Bruhwiler, L. and Tans, P. P.: A geostatistical approach to surface flux estimation of atmospheric trace gases, J. Geophys. Res., 109(D14), D14109, doi:10.1029/2003JD004422, 2004.

Miles, W. and Barry, G.: A 5-year satellite climatology of winter sea ice leads, J. Geophys. Res., 103(C10), 21723–21734, 1998.

Miller, C. M., Dickens, G. R., Jakobsson, M., Johansson, C., Koshurnikov, A., O'Regan, M., Muschitiello, F., Stranne, C. and Mörth, C.-M.: Pore water geochemistry along continental slopes north of the East Siberian Sea: inference of low methane concentrations, Biogeosciences, 14(12), 2929–2953, doi:10.5194/bg-14-2929-2017, 2017.

Miller, S. M., Michalak, A. M. and Levi, P. J.: Atmospheric inverse modeling with known physical bounds: An example from trace gas emissions, Geosci. Model Dev., 7(1), 303–315, doi:10.5194/gmd-7-303-2014, 2014a.

Miller, S. M., Worthy, D. E. J., Michalak, A. M., Wofsy, S. C., Kort, E. A., Havice, T. C., Andrews, A. E., Dlugokencky, E. J., Kaplan, J. O., Levi, P. J., Tian, H. and Zhang, B.: Observational constraints on the distribution, seasonality, and environmental predictors of North American boreal methane emissions, Global Biogeochem. Cycles, 28(2), 146–160, doi:10.1002/2013GB004580, 2014b.

Miller, S. M., Miller, C. E., Commane, R., Chang, R. Y.-W., Dinardo, S. J., Henderson, J. M., Karion, A., Lindaas, J., Melton, J. R., Miller, J. B., Sweeney, C., Wofsy, S. C. and Michalak, A. M.: A multiyear estimate of methane fluxes in Alaska from CARVE atmospheric observations, Global Biogeochem. Cycles, 30(10), 1441–1453, doi:10.1002/2016GB005419, 2016.

Myhre, C. L., Ferré, B., Platt, S. M., Silyakova, A., Hermansen, O., Allen, G., Pisso, I., Schmidbauer, N., Stohl, A., Pitt, J., Jansson, P., Greinert, J., Percival, C. J., Fjaeraa, A. M., O'Shea, S. J., Gallagher, M. W., Le Breton, M., Bower, K. N., Bauguitte, S. J. B., Dalsøren, S. B., Vadakkepuliyambatta, S., Fisher, R. E., Nisbet, E. G., Lowry, D., Myhre, G., Pyle, J. A., Cain, M. L. and Mienert, J.: Extensive release of methane from Arctic seabed west of Svalbard during summer 2014 does not influence the atmosphere, Geophys. Res. Lett., 43(9), 4624–4631, doi:10.1002/2016GL068999, 2016.

Nicolsky, D., Romanovsky, V. E., Romanovskii, N. N., Kholodov, A. L., Shakhova, N. E. and

Semiletov, I. P.: Modeling sub-sea permafrost in the East Siberian Arctic Shelf: The Laptev Sea region, J. Geophys. Res., 117(F3), F03028, doi:10.1029/2012JF002358, 2012.

Nuñez Ramirez, T. G.: PhD thesis (in prep.), Max Planck Institute for Biogeochemistry., 2019.

Olson, D. M., Dinerstein, E., Wikramanayake, E. D., Burgess, N. D., Powell, G. V. N., Underwood, E. C., D'amico, J. A., Itoua, I., Strand, H. E., Morrison, J. C., Loucks, C. J., Allnutt, T. F., Ricketts, T. H., Kura, Y., Lamoreux, J. F., Wettengel, W. W., Hedao, P. and Kassem, K. R.: Terrestrial Ecoregions of the World: A New Map of Life on Earth, Bioscience, 51(11), 933, doi:10.1641/0006-3568(2001)051[0933:TEOTWA]2.0.CO;2, 2001.

Overduin, P. P., Liebner, S., Knoblauch, C., Günther, F., Wetterich, S., Schirrmeister, L., Hubberten, H.-W. and Grigoriev, M. N.: Methane oxidation following submarine permafrost degradation: Measurements from a central Laptev Sea shelf borehole, J. Geophys. Res. Biogeosciences, 120(5), 965–978, doi:10.1002/2014JG002862, 2015.

Pankratova, N., Skorokhod, A., Belikov, I., Elansky, N., Rakitin, V., Shtabkin, Y. and Berezina, E.: Evidence of atmospheric response to methane emissions from the East Siberian Arctic Shelf, Geogr. Environ. Sustain., 11(1), 85–92, doi:10.24057/2071-9388-2018-11-1-85-92, 2018.

Paull, C. K., Ussler, W., Dallimore, S. R., Blasco, S. M., Lorenson, T. D., Melling, H., Medioli, B. E., Nixon, F. M. and McLaughlin, F. A.: Origin of pingo-like features on the Beaufort Sea shelf and their possible relationship to decomposing methane gas hydrates, Geophys. Res. Lett., 34(1), 1–5, doi:10.1029/2006GL027977, 2007.

Pickett-Heaps, C., Jacob, D. J., Wecht, K. J., Kort, E. A., Wofsy, S. C., Diskin, G. S., Worthy, D. E. J., Kaplan, J. O., Bey, I. and Drevet, J.: Magnitude and seasonality of wetland methane emissions from the Hudson Bay Lowlands (Canada), Atmos. Chem. Phys., 11, 3773–3779, doi:10.5194/acp-11-3773-2011, 2011.

Portnov, A., Smith, A. J., Mienert, J., Cherkashov, G., Rekant, P., Semenov, P., Serov, P. and Vanshtein, B.: Offshore permafrost decay and massive seabed methane escape in water depths > 20 m at the South Kara Sea shelf, Geophys. Res. Lett., 40(15), 3962–3967, doi:10.1002/grl.50735, 2013.

Rachold, V., Grigoriev, M. N., Are, F. E., Solomon, S., Reimnitz, E., Kassens, H. and Antonow, M.: Coastal erosion vs riverine sediment discharge in the Arctic Shelf seas, Int. J. Earth Sci., 89(3), 450–460, doi:10.1007/s005310000113, 2000.

Ramsey, F. L. and Schafer, D. W.: The Statistical Sleuth: A course in methods of data analysis, Duxbury Press, Belmont, CA., 1997.

Reeburgh, W. S.: Oceanic methane biogeochemistry., Chem. Rev., 107(2), 486–513, doi:10.1021/cr050362v, 2007.

Rella, C. W., Chen, H., Andrews, A. E., Filges, A., Gerbig, C., Hatakka, J., Karion, A., Miles, N. L., Richardson, S. J., Steinbacher, M., Sweeney, C., Wastine, B. and Zellweger, C.: High accuracy measurements of dry mole fractions of carbon dioxide and methane in humid air, Atmos. Meas. Tech., 6(3), 837–860, doi:10.5194/amt-6-837-2013, 2013.

Repeta, D. J., Ferrón, S., Sosa, O. A., Johnson, C. G., Repeta, L. D., Acker, M., DeLong, E. F. and Karl, D. M.: Marine methane paradox explained by bacterial degradation of dissolved organic matter, Nat. Geosci., 9(12), 884–887, doi:10.1038/ngeo2837, 2016.

Reum, F.: Optimization of greenhouse gas flux estimations using data obtained by the GOSAT spacecraft, Max Planck Institute for Biogeochemistry, Jena., 2012.

Reum, F., Göckede, M., Lavric, J. V, Kolle, O., Zimov, S., Zimov, N., Pallandt, M. and Heimann, M.: Accurate measurements of atmospheric carbon dioxide and methane mole fractions at the Siberian coastal site Ambarchik, Atmos. Meas. Tech. Discuss., 1–44, doi:10.5194/amt-2018-325, 2018a.

Reum, F., Gerbig, C., Lavric, J. V, Rella, C. W. and Göckede, M.: Correcting atmospheric CO_2 and CH_4 mole fractions obtained with Picarro analyzers for sensitivity of cavity pressure to water vapor, Atmos. Meas. Tech. Discuss., 2(August), 1–29, doi:10.5194/amt-2018-242, 2018b.

Rienecker, M. M., Suarez, M. J., Gelaro, R., Todling, R., Bacmeister, J., Liu, E., Bosilovich, M. G., Schubert, S. D., Takacs, L., Kim, G. K., Bloom, S., Chen, J., Collins, D., Conaty, A., Da Silva, A., Gu, W., Joiner, J., Koster, R. D., Lucchesi, R., Molod, A., Owens, T., Pawson, S., Pegion, P., Redder, C. R., Reichle, R., Robertson, F. R., Ruddick, A. G., Sienkiewicz, M. and Woollen, J.: MERRA: NASA's modern-era retrospective analysis for research and applications, J. Clim., 24(14), 3624–3648, doi:10.1175/JCLI-D-11-00015.1, 2011.

Rödenbeck, C., Houweling, S., Gloor, M. and Heimann, M.: CO_2 flux history 1982–2001 inferred from atmospheric data using a global inversion of atmospheric transport, Atmos. Chem. Phys., 3, 1919–1964, doi:10.5194/acp-3-1919-2003, 2003.

Rodgers, C. D.: Inverse Methods for Atmospheric Sounding, World Scientific Publishing Co. Pte. Ltd., 2000.

Romanovskii, N. N. and Hubberten, H.-W.: Results of permafrost modelling of the lowlands and shelf of the Laptev Sea Region, Russia, Permafr. Periglac. Process., 12(2), 191–202, doi:10.1002/ppp.387, 2001.

Romanovskii, N. N., Hubberten, H.-W., Gavrilov, A. V., Eliseeva, A. A. and Tipenko, G. S.: Offshore permafrost and gas hydrate stability zone on the shelf of East Siberian Seas, Geo-Marine Lett., 25(2–3), 167–182, doi:10.1007/s00367-004-0198-6, 2005.

Ruppel, C.: Permafrost-associated gas hydrate: Is it really approximately 1 % of the global system?, J. Chem. Eng. Data, 60(2), 429–436, doi:10.1021/je500770m, 2015.

Sapart, C.-J., Shakhova, N. E., Semiletov, I. P., Jansen, J., Szidat, S., Kosmach, D., Dudarev, O., van der Veen, C., Egger, M., Sergienko, V., Salyuk, A., Tumskoy, V., Tison, J.-L. and Röckmann, T.: The origin of methane in the East Siberian Arctic Shelf unraveled with triple isotope analysis, Biogeosciences, 14(9), 2283–2292, doi:10.5194/bg-14-2283-2017, 2017.

Saunois, M., Bousquet, P., Poulter, B., Peregon, A., Ciais, P., Canadell, J. G., Dlugokencky, E. J., Etiope, G., Bastviken, D., Houweling, S., Janssens-Maenhout, G., Tubiello, F. N., Castaldi, S., Jackson, R. B., Alexe, M., Arora, V. K., Beerling, D. J., Bergamaschi, P., Blake, D. R., Brailsford, G., Brovkin, V., Bruhwiler, L., Crevoisier, C., Crill, P., Covey, K., Curry, C. L., Frankenberg, C., Gedney, N., Höglund-Isaksson, L., Ishizawa, M., Ito, A., Joos, F., Kim, H.-S., Kleinen, T., Krummel, P., Lamarque, J.-F., Langenfelds, R., Locatelli, R., Machida, T., Maksyutov, S., McDonald, K. C., Marshall, J., Melton, J. R., Morino, I., Naik, V., O'Doherty, S., Parmentier, F.-J. W., Patra, P. K., Peng, C., Peng, S., Peters, G. P., Pison, I., Prigent, C., Prinn, R., Ramonet, M., Riley, W. J., Saito, M., Santini, M., Schroeder, R., Simpson, I. J., Spahni, R., Steele, P., Takizawa, A., Thornton, B. F., Tian, H., Tohjima, Y., Viovy, N., Voulgarakis, A., van Weele, M., van der Werf, G. R., Weiss, R. F., Wiedinmyer, C., Wilton, D. J., Wiltshire, A., Worthy, D. E. J., Wunch, D. B., Xu, X., Yoshida, Y., Zhang, B., Zhang, Z. and Zhu, Q.: The global methane budget 2000–2012, Earth Syst. Sci. Data, 8(2), 697–751, doi:10.5194/essd-8-697-2016, 2016.

Savvichev, A. S., Rusanov, I. I., Pimenov, N. V., Zakharova, E. E., Veslopolova, E. F., Lein, A. Y., Crane, K. and Ivanov, M. V.: Microbial processes of the carbon and sulfur cycles in the Chukchi Sea, Microbiology, 76(5), 603–613, doi:10.1134/S0026261707050141, 2007.

Schröder, H.: Methan in der marinen Wassersäule der Laptew See, Prozesse und Verteilung, Friedrich-Alexander Universität Erlangen-Nürnberg. [online] Available from: http://epic.awi.de/28691/1/Sch2000bj.pdf, 2000.

Schuur, E. A. G., Abbott, B. W., Bowden, W. B., Brovkin, V., Camill, P., Canadell, J. G., Chanton, J. P., Chapin, F. S., Christensen, T. R., Ciais, P., Crosby, B. T., Czimczik, C. I., Grosse, G., Harden, J., Hayes, D. J., Hugelius, G., Jastrow, J. D., Jones, J. B., Kleinen, T., Koven, C. D., Krinner, G., Kuhry, P., Lawrence, D. M., McGuire, A. D., Natali, S. M., O'Donnell, J. A., Ping, C. L., Riley, W. J., Rinke, A., Romanovsky, V. E., Sannel, A. B. K., Schädel, C., Schaefer, K., Sky, J., Subin, Z. M., Tarnocai, C., Turetsky, M. R., Waldrop, M. P., Walter Anthony, K. M., Wickland, K. P., Wilson, C. J. and Zimov, S. A.: Expert assessment of vulnerability of permafrost carbon to climate change, Clim. Change, 119(2), 359–374, doi:10.1007/s10584-013-0730-7, 2013.

Schuur, E. A. G., McGuire, A. D., Schädel, C., Grosse, G., Harden, J. W., Hayes, D. J., Hugelius, G., Koven, C. D., Kuhry, P., Lawrence, D. M., Natali, S. M., Olefeldt, D., Romanovsky, V. E., Schaefer, K., Turetsky, M. R., Treat, C. C. and Vonk, J. E.: Climate change and the permafrost carbon feedback, Nature, 520(7546), 171–179, doi:10.1038/nature14338, 2015.

Semiletov, I. P., Dudarev, O., Luchin, V., Charkin, A., Shin, K. H. and Tanaka, N.: The East Siberian Sea as a transition zone between Pacific-derived waters and Arctic shelf waters, Geophys. Res. Lett., 32(10), 1–5, doi:10.1029/2005GL022490, 2005.

Semiletov, I. P., Shakhova, N. E., Sergienko, V. I., Pipko, I. I. and Dudarev, O. V.: On carbon transport and fate in the East Siberian Arctic land–shelf–atmosphere system, Environ. Res. Lett., 7(1), 015201, doi:10.1088/1748-9326/7/1/015201, 2012.

Shakhova, N., Semiletov, I., Sergienko, V., Lobkovsky, L., Yusupov, V., Salyuk, A., Salomatin, A., Chernykh, D., Kosmach, D., Panteleev, G., Nicolsky, D., Samarkin, V., Joye, S., Charkin, A., Dudarev, O., Meluzov, A. and Gustafsson, O.: The East Siberian Arctic Shelf: towards further assessment of permafrost-related methane fluxes and role of sea ice, Philos. Trans. R. Soc. A Math. Phys. Eng. Sci., 373(2052), 20140451, doi:10.1098/rsta.2014.0451, 2015.

Shakhova, N. E. and Semiletov, I. P.: Methane release and coastal environment in the East Siberian Arctic shelf, J. Mar. Syst., 66(1–4), 227–243, doi:10.1016/j.jmarsys.2006.06.006, 2007.

Shakhova, N. E., Semiletov, I. P. and Panteleev, G.: The distribution of methane on the Siberian Arctic shelves: Implications for the marine methane cycle, Geophys. Res. Lett., 32(9), L09601, doi:10.1029/2005GL022751, 2005.

Shakhova, N. E., Semiletov, I. P., Salyuk, A., Yusupov, V., Kosmach, D. and Gustafsson, O.: Extensive Methane Venting to the Atmosphere from Sediments of the East Siberian Arctic Shelf, Science (80-.)., 327(5970), 1246–1250, doi:10.1126/science.1182221, 2010a.

Shakhova, N. E., Semiletov, I. P., Leifer, I., Salyuk, A., Rekant, P. and Kosmach, D.: Geochemical and geophysical evidence of methane release over the East Siberian Arctic Shelf, J. Geophys. Res., 115(C8), C08007, doi:10.1029/2009JC005602, 2010b.

Shakhova, N. E., Semiletov, I. P., Leifer, I., Sergienko, V., Salyuk, A., Kosmach, D., Chernykh, D., Stubbs, C., Nicolsky, D., Tumskoy, V. and Gustafsson, Ö.: Ebullition and storm-induced methane release from the East Siberian Arctic Shelf, Nat. Geosci., 7(1), 64–70, doi:10.1038/ngeo2007, 2014.

Sher, A. V., Kuzmina, S. A., Kuznetsova, T. V. and Sulerzhitsky, L. D.: New insights into the Weichselian environment and climate of the East Siberian Arctic, derived from fossil insects, plants, and mammals, Quat. Sci. Rev., 24(5–6), 533–569, doi:10.1016/j.quascirev.2004.09.007, 2005.

Skamarock, W. C., Klemp, J. B., Dudhi, J., Gill, D. O., Barker, D. M., Duda, M. G., Huang, X.-Y., Wang, W. and Powers, J. G.: A Description of the Advanced Research WRF Version 3. NCAR Technical Note NCAR/TN-475+STR., 2008.

Spalding, M. D., Fox, H. E., Allen, G. R., Davidson, N., Ferdaña, Z. A., Finlayson, M., Halpern, B. S., Jorge, M. A., Lombana, A., Lourie, S. A., Martin, K. D., McManus, E., Molnar, J., Recchia, C. A. and Robsertson, J.: Marine Ecoregions of the World: A Bioregionalization of Coastal and Shelf Areas, Bioscience, 57(7), 573, doi:10.1641/B570707, 2007.

Sparrow, K. J., Kessler, J. D., Southon, J. R., Garcia-Tigreros, F., Schreiner, K. M., Ruppel, C. D., Miller, J. B., Lehman, S. J. and Xu, X.: Limited contribution of ancient methane to surface waters of the U.S. Beaufort sea shelf, Sci. Adv., 4(1), 1–8, doi:10.1126/sciadv.aao4842, 2018.

Spreen, G., Kaleschke, L. and Heygster, G.: Sea ice remote sensing using AMSR-E 89-GHz channels, J. Geophys. Res., 113(C2), C02S03, doi:10.1029/2005JC003384, 2008.

Steffen, W., Rockström, J., Richardson, K., Lenton, T. M., Folke, C., Liverman, D., Summerhayes, C. P., Barnosky, A. D., Cornell, S. E., Crucifix, M., Donges, J. F., Fetzer, I., Lade, S. J., Scheffer, M., Winkelmann, R. and Schellnhuber, H. J.: Trajectories of the Earth System in the Anthropocene, Proc. Natl. Acad. Sci., 115(33), 8252–8259, doi:10.1073/pnas.1810141115, 2018.

Steiner, N. S., Lee, W. G. and Christian, J. R.: Enhanced gas fluxes in small sea ice leads and cracks: Effects on CO_2 exchange and ocean acidification, J. Geophys. Res. Ocean., 118(3), 1195–1205, doi:10.1002/jgrc.20100, 2013.

Stull, R. B.: An Introduction to Boundary Layer Meteorology, Springer Netherlands, Dordrecht., 1988.

Sweeney, C., Gloor, E., Jacobson, A. R., Key, R. M., McKinley, G. A., Sarmiento, J. L. and Wanninkhof, R. H.: Constraining global air-sea gas exchange for CO_2 with recent bomb ^{14}C measurements, Global Biogeochem. Cycles, 21(2), 1–10, doi:10.1029/2006GB002784, 2007.

Sweeney, C., Dlugokencky, E., Miller, C. E., Wofsy, S., Karion, A., Dinardo, S., Chang, R. Y.-W., Miller, J. B., Bruhwiler, L., Crotwell, A. M., Newberger, T., McKain, K., Stone, R. S., Wolter, S. E., Lang, P. E. and Tans, P.: No significant increase in long-term CH_4 emissions on North Slope of Alaska despite significant increase in air temperature, Geophys. Res. Lett., 43(12), 6604–6611, doi:10.1002/2016GL069292, 2016.

Tan, Z., Zhuang, Q. and Walter Anthony, K. M.: Modeling methane emissions from arctic lakes: Model development and site-level study, J. Adv. Model. Earth Syst., 7(2), 459–483, doi:10.1002/2014MS000344, 2015.

Tarantola, A.: Inverse problem theory, methods for data fitting and model parameter estimation, Elsevier Science, Amsterdam., 1987.

Tarantola, A.: Inverse Problem Theory and Methods for Model Parameter Estimation, SIAM., 2005.

Thonat, T., Saunois, M., Bousquet, P., Pison, I., Tan, Z., Zhuang, Q., Crill, P. M., Thornton, B. F., Bastviken, D., Dlugokencky, E. J., Zimov, N., Laurila, T., Hatakka, J., Hermansen, O. and Worthy, D. E. J.: Detectability of Arctic methane sources at six sites performing continuous atmospheric measurements, Atmos. Chem. Phys., 17(13), 8371–8394, doi:10.5194/acp-17-8371-2017, 2017.

Thoning, K. W., Tans, P. P. and Komhyr, W. D.: Atmospheric carbon dioxide at Mauna Loa Observatory: 2. Analysis of the NOAA GMCC data, 1974–1985, J. Geophys. Res., 94(D6), 8549, doi:10.1029/JD094iD06p08549, 1989.

Thornton, B. F., Wik, M. and Crill, P. M.: Double-counting challenges the accuracy of high-latitude methane inventories, Geophys. Res. Lett., 43(24), 12,569-12,577, doi:10.1002/2016GL071772, 2016a.

Thornton, B. F., Geibel, M. C., Crill, P. M., Humborg, C. and Mörth, C. M.: Methane fluxes from the sea to the atmosphere across the Siberian shelf seas, Geophys. Res. Lett., 43(11), 5869–5877, doi:10.1002/2016GL068977, 2016b.

Turner, A. J., Jacob, D. J., Benmergui, J., Brandman, J., White, L. and Randles, C. A.: Assessing the capability of different satellite observing configurations to resolve the distribution of methane emissions at kilometer scales, Atmos. Chem. Phys. Discuss., 1–23, doi:10.5194/acp-2018-164, 2018.

Uttal, T., Makshtas, A. and Laurila, T.: The Tiksi International Hydrometeorological Observatory - An Arctic members partnership, WMO Bull., 62(2), 2013.

Vickers, D. and Mahrt, L.: Quality Control and Flux Sampling Problems for Tower and Aircraft Data, J. Atmos. Ocean. Technol., 14(3), 512–526, doi:10.1175/1520-0426(1997)014<0512:QCAFSP>2.0.CO;2, 1997.

Vonk, J. E., Sánchez-García, L., van Dongen, B. E., Alling, V., Kosmach, D., Charkin, A., Semiletov, I. P., Dudarev, O. V., Shakhova, N. E., Roos, P., Eglinton, T. I., Andersson, A. and Gustafsson, Ö.: Activation of old carbon by erosion of coastal and subsea permafrost in Arctic Siberia., Nature, 489(7414), 137–40, doi:10.1038/nature11392, 2012.

Wåhlström, I. and Meier, H. E. M.: A model sensitivity study for the sea–air exchange of methane in the Laptev Sea, Arctic Ocean, Tellus B Chem. Phys. Meteorol., 66(1), 24174, doi:10.3402/tellusb.v66.24174, 2014.

Wåhlström, I., Omstedt, A., Björk, G. and Anderson, L. G.: Modelling the CO_2 dynamics in the Laptev Sea, Arctic Ocean: Part I, J. Mar. Syst., 102–104, 29–38, doi:10.1016/j.jmarsys.2012.05.001, 2012.

Walczowski, W. and Piechura, J.: New evidence of warming propagating toward the Arctic Ocean, Geophys. Res. Lett., 33(12), 1–5, doi:10.1029/2006GL025872, 2006.

Wang, Q., Danilov, S., Jung, T., Kaleschke, L. and Wernecke, A.: Sea ice leads in the Arctic Ocean: Model assessment, interannual variability and trends, Geophys. Res. Lett., 43(13), 7019–7027, doi:10.1002/2016GL068696, 2016.

Wania, R., Melton, J. R., Hodson, E. L., Poulter, B., Ringeval, B., Spahni, R., Bohn, T. J., Avis, C. A., Chen, G., Eliseev, A. V., Hopcroft, P. O., Riley, W. J., Subin, Z. M., Tian, H., van Bodegom, P. M., Kleinen, T., Yu, Z. C., Singarayer, J. S., Zürcher, S., Lettenmaier, D. P., Beerling, D. J., Denisov, S. N., Prigent, C., Papa, F. and Kaplan, J. O.: Present state of global wetland extent and wetland methane modelling: methodology of a model inter-comparison project (WETCHIMP), Geosci. Model Dev., 6(3), 617–641, doi:10.5194/gmd-6-617-2013, 2013.

Wanninkhof, R. H.: Relationship Between Wind Speed and Gas Exchange, J. Geophys. Res., 97(92), 7373–7382, doi:10.1029/92JC00188, 1992.

Ward, E. J.: A review and comparison of four commonly used Bayesian and maximum likelihood model selection tools, Ecol. Modell., 211(1–2), 1–10, doi:10.1016/j.ecolmodel.2007.10.030, 2008.

Warwick, N. J., Cain, M. L., Fisher, R., France, J. L., Lowry, D., Michel, S. E., Nisbet, E. G., Vaughn, B. H., White, J. W. C. and Pyle, J. A.: Using δ13C-CH_4 and δD-CH_4 to constrain Arctic methane emissions, Atmos. Chem. Phys., 16(23), 14891–14908, doi:10.5194/acp-16-14891-2016, 2016.

Weatherall, P., Marks, K. M., Jakobsson, M., Schmitt, T., Tani, S., Arndt, J. E., Rovere, M., Chayes, D., Ferrini, V. and Wigley, R.: A new digital bathymetric model of the world's oceans, Earth Sp. Sci., 2(8), 331–345, doi:10.1002/2015EA000107, 2015.

Westbrook, G. K., Thatcher, K. E., Rohling, E. J., Piotrowski, A. M., Pälike, H., Osborne, A. H., Nisbet, E. G., Minshull, T. a., Lanoisellé, M., James, R. H., Hühnerbach, V., Green, D., Fisher, R. E., Crocker, A. J., Chabert, A., Bolton, C., Beszczynska-Möller, A., Berndt, C. and Aquilina, A.: Escape of methane gas from the seabed along the West Spitsbergen continental margin, Geophys. Res. Lett., 36(15), doi:10.1029/2009GL039191, 2009.

Wik, M., Varner, R. K., Anthony, K. W., MacIntyre, S. and Bastviken, D.: Climate-sensitive northern lakes and ponds are critical components of methane release, Nat. Geosci., 9(2), 99–105, doi:10.1038/ngeo2578, 2016.

Winkel, M., Mitzscherling, J., Overduin, P. P., Horn, F., Winterfeld, M., Rijkers, R., Grigoriev, M. N., Knoblauch, C., Mangelsdorf, K., Wagner, D. and Liebner, S.: Anaerobic methanotrophic communities thrive in deep submarine permafrost, Sci. Rep., 8(1), 1–13, doi:10.1038/s41598-018-19505-9, 2018.

WMO: 18th WMO/IAEA Meeting on Carbon Dioxide, Other Greenhouse Gases and Related Tracers Measurement Techniques (GGMT-2015). [online] Available from: https://library.wmo.int/opac/doc_num.php?explnum_id=3074, 2016.

Yadav, V. and Michalak, A. M.: Improving computational efficiency in large linear inverse problems: an example from carbon dioxide flux estimation, Geosci. Model Dev., 6(3), 583–590, doi:10.5194/gmd-6-583-2013, 2013.

Yadav, V., Mueller, K. L. and Michalak, A. M.: A backward elimination discrete optimization algorithm for model selection in spatio-temporal regression models, Environ. Model. Softw., 42, 88–98, doi:http://dx.doi.org/10.1016/j.envsoft.2012.12.009, 2013.

El Yazidi, A., Ramonet, M., Ciais, P., Broquet, G., Pison, I., Abbaris, A., Brunner, D., Conil, S., Delmotte, M., Gheusi, F., Guerin, F., Hazan, L., Kachroudi, N., Kouvarakis, G., Mihalopoulos, N., Rivier, L. and Serça, D.: Identification of spikes associated with local sources in continuous time series of atmospheric CO, CO_2 and CH_4, Atmos. Meas. Tech., 11(3), 1599–1614, doi:10.5194/amt-11-1599-2018, 2018.

Yu, J., Xie, Z., Sun, L., Kang, H., He, P. and Xing, G.: δ13C-CH4 reveals CH4 variations over oceans from mid-latitudes to the Arctic, Sci. Rep., 5(1), 13760, doi:10.1038/srep13760, 2015.

Yurganov, L. N. and Leifer, I.: Estimates of methane emission rates from some Arctic and sub-Arctic areas based on orbital interferometer IASI data, Curr. Probl. Remote Sens. Earth from Sp., 13(3), 173–183, doi:10.21046/2070-7401-2016-13-3-173-183, 2016.

Zavarsky, A., Goddijn-Murphy, L., Steinhoff, T. and Marandino, C. A.: Bubble-Mediated Gas Transfer and Gas Transfer Suppression of DMS and CO_2, J. Geophys. Res. Atmos., 123(12), 6624–6647, doi:10.1029/2017JD028071, 2018.

Zhang, W., Miller, P. A., Smith, B., Wania, R., Koenigk, T. and Döscher, R.: Tundra shrubification and tree-line advance amplify arctic climate warming: results from an individual-based dynamic vegetation model, Environ. Res. Lett., 8(3), 034023, doi:10.1088/1748-9326/8/3/034023, 2013.

Zhou, J., Tison, J. L., Carnat, G., Geilfus, N. X. and Delille, B.: Physical controls on the storage of methane in landfast sea ice, Cryosphere, 8(3), 1019–1029, doi:10.5194/tc-8-1019-2014, 2014.

Zimov, S. A., Schuur, E. A. G., Iii, F. S. C. and Chapin, F. S.: Climate change. Permafrost and the global carbon budget., Science (80-.)., 312(5780), 1612–3, doi:10.1126/science.1128908, 2006.

Zona, D., Gioli, B., Commane, R., Lindaas, J., Wofsy, S. C., Miller, C. E., Dinardo, S. J., Dengel, S., Sweeney, C., Karion, A., Chang, R. Y.-W., Henderson, J. M., Murphy, P. C., Goodrich, J. P., Moreaux, V., Liljedahl, A., Watts, J. D., Kimball, J. S., Lipson, D. A. and Oechel, W. C.: Cold season emissions dominate the Arctic tundra methane budget, Proc. Natl. Acad. Sci., 113(1), 40–45, doi:10.1073/pnas.1516017113, 2016.

List of figures

List of tables

List of publications

Reum, F., Göckede, M., Lavric, J. V, Kolle, O., Zimov, S., Zimov, N., Pallandt, M. and Heimann, M.: Accurate measurements of atmospheric carbon dioxide and methane mole fractions at the Siberian coastal site Ambarchik, Atmos. Meas. Tech. Discuss., 1–44, doi:10.5194/amt-2018-325, 2018a.

Reum, F., Gerbig, C., Lavric, J. V, Rella, C. W. and Göckede, M.: Correcting atmospheric CO_2 and CH_4 mole fractions obtained with Picarro analyzers for sensitivity of cavity pressure to water vapor, Atmos. Meas. Tech. Discuss., 2(August), 1–29, doi:10.5194/amt-2018-242, 2018b.

Acknowledgements

This work would not have been possible without the support from colleagues, supervisors, collaborators and friends and family.

First and foremost, I would like to thank my supervisor Mathias Göckede for his invaluable and tireless support through all stages of my PhD project, the freedom to pursue my own ideas and advice on life as a scientist. Without Mathias, I would not have made it anywhere close to this point.

Thanks to Martin Heimann and Martin Claußen for serving as evaluators of this thesis and together with Victor Brovkin, Jošt Lavrič, Martin Stendel and Mathias constituted my PhD advisory committees in Jena and Hamburg.

Thanks to Mathias Göckede, Martin Heimann, the Max Planck Society, the European Commission and the European Science Foundation for the financial support to carry out this work.

Thanks to everyone who made the establishment of the Ambarchik station possible: Martin Heimann, Sergey Zimov, Nikita Zimov, Mathias, Jošt, Olaf Kolle and Martin Hertel. Thanks to the crew who keeps the station running on-site: Dima, Nadya, Maxim, Igor, and the ever-changing crew of the Roshydromet weather station Ambarchik. Thanks to Martijn Pallandt and Mathias for taking over care for the Ambarchik station. May it run for many years to come!

Thanks to Christoph Gerbig and Chris Rella for valuable ideas and impulses on the water vapor correction of Picarro greenhouse gas analyzers.

Thanks for support in the lab to Jošt, Stephan Baum, Christoph, Annette Filges, Reimo Leppert and Dietrich Feist.

Thanks to Julia Marshall, Dietrich Feist, Andrew Durso and Martin Heimann for valuable comments on manuscripts.

Thanks to Scot Miller and Anna Michalak, who helped kick-start the geostatistical inverse model during my research stay at the Department for Global Ecology of the Carnegie Institution in Stanford. Special thanks to Scot for continued support on modeling methods and interpretations.

Thanks to the people who provided input for the inverse model: John Henderson, Frank-Thomas Koch, Tonatiuh Guillermo Nuñez Ramirez, Stefan Kern, Ted Bohn, Weixin Zhang, Zeli Tan and Tuomas Laurila.

Thanks to Lars Kaleschke, Stefan Kern and Markus Janout for valuable discussions on sea ice.

Thanks to my colleagues at the Max Planck Institute for Biogeochemistry for discussions on each and every topic and for making my time there worthwhile, especially my office mates: Jan Winderlich, Eric Morgan, Tonatiuh Guillermo Nuñez Ramirez, Steffen Schmidt, Ina Burjack, Sabrina Arnold, Gionata Biavati, Sandra Raab and Martijn Pallandt; (other) members of the IPAS group: Fanny Kittler, Min Jung Kwon, Karel Castro-Morales; my other fellow BSY-lers: Julia Marshall, Christian Rödenbeck, Chirag Dhara, Shreeya Verma, Martin Kunz, Michal Galkowski, Ulli Schleier and Silvana Schott; and everyone who keeps the institute running.

Thanks to Reimo for fixing my computer when its infamous hard drive cable failed!

Thanks to Steffi Rothhardt for her support of the PhD students at the MPI-BGC.

To my friends, whom I can (and do) always count on, especially Kathrin, Irma, Sven and Juliane: Thank you!

Lastly, special thanks go to my parents Renate and Hans-Joachim. You are always there for me.

Eidesstaatliche Versicherung

Hiermit versichere ich an Eides statt, dass ich die vorliegende Dissertation mit dem Titel: „Methane emissions from the East Siberian Arctic Shelf inferred from accurate observations of atmospheric methane mole fractions“ selbstständig verfasst und keine anderen als die angegebenen Hilfsmittel – insbesondere keine im Quellenverzeichnis nicht benannten Internet-Quellen – benutzt habe. Alle Stellen, die wörtlich oder sinngemäß aus Veröffentlichungen entnommen wurden, sind als solche kenntlich gemacht. Ich versichere weiterhin, dass ich die Dissertation oder Teile davon vorher weder im In- noch im Ausland in einem anderen Prüfungsverfahren eingereicht habe und die eingereichte schriftliche Fassung der auf dem elektronischen Speichermedium entspricht.

Jena, 10.1.2019

Friedemann Reum